Technologies in the 2 μm waveband

Eoin Russell
BSc
112357281

NATIONAL UNIVERSITY OF IRELAND, CORK

SCHOOL OF SCIENCE

DEPARTMENT OF PHYSICS

Thesis submitted for the degree of Doctor of Philosophy

December 2021

Head of Department:	Prof. John McInerney
Supervisors:	Dr. Fatima G. Gunning Mr. Brian Corbett

Research supported by the Irish Research Council (GOPOIG/2017/385)

Contents

List of Figures

List of Tables

I, Eoin Russell, certify that this thesis is my own work and I have not obtained a degree in this university or elsewhere on the basis of the work submitted in this thesis.

Eoin Russell

List of Acronyms

ASE: Amplified Spontaneous Emission
AU: Arbitrary Unit
CMOS: Complementary Metal–Oxide–Semiconductor
CNR: Carrier Noise Ratio
CW: Continuous Wave
DFC: Dual Frequency Comb
EDFA: Erbium Doped Fibre Amplifier
ESA: Electrical Spectrum Analyser
FP: Fabry-Pérot
FSR: Free Spectral Range
FTIR: Fourier Transform Infrared Spectroscopy
FWHM: Full Width Half Maximum
FWM: Four Wave Mixing
HC-PBGF: Hollow Core Photonic bandgap Fibre
LI: Light–Current
LIDAR: Light Detection and Ranging
MZM: Mach-Zehnder Modulator
MQW: Multi-Quantum Well
OFC: Optical Frequency Comb
OSA: Optical Spectrum Analyser
OSNR: Optical Signal Noise Ratio
PC: Polarisation Controller
PD: Photodiode
PIC: Photonic Integrated Circuit
QCL: Quantum Cascade Laser
SMSR: Side Mode Suppression Ratio
SNR: Signal Noise Ratio
SOA: Semiconductor Optical Amplifier
SOI: Silicon On Insulator
TDFA: Thulium Doped Fibre Amplifier
TEC: Thermo-Electric Controller
TPA: Two-Photon Absorption
XPM: Cross Phase Modulation

List of Publications

E. Russell, N. Kavanagh, K. Shortiss and F. C. Garcia Gunning, "Development of thulium-doped fibre amplifiers for the 2 μm waveband," SPIE Proceedings, 10683, Fiber Lasers and Glass Photonics: Materials through Applications, 106832Q (2018).

F. C. Garcia Gunning, N. Kavanagh, E. Russell, R. Sheehan, J. O'Callaghan, and B. Corbett, "Key enabling technologies for optical communications at 2000 nm," Applied Optics, 57, E64-E70 (2018).

E. Russell, B. Corbett and F. C. Garcia Gunning, "Gain switched dual frequency comb at 2 μm," Optics Express, (Accepted for publication on 07/12/21), Assigned Issue Vol. 29 No. 26.

Acknowledgements

First and foremost, I would like to thank my supervisor, Dr Fatima Gunning, for giving me the opportunity to pursue my PhD in the Photonics Systems Group at the Tyndall National Institute. You have worked to create a very positive and welcoming atmosphere in your group where I always felt like my goals were supported and my ideas heard. Thank you for all the guidance and for giving me the freedom to pursue subjects and projects which I personally found engaging and exciting.

To my parents, Mary and Niko, thank you for everything. You have given me so much support throughout my life. You have both given everything to me, Caoimh and Conor so we could have the opportunities to pursue our passions. Thank you for always believing in me.

To my partner Nicole, you have been a part of this journey with me from the beginning. You have experienced all the highs and lows alongside me and I couldn't have done it without you. Thank you for being so supportive of my ambitions and for keeping me focused on what is really important.

To my friends, Rory, Michael, Killian, Caolan, Brian, Dave and Adam. We started our journeys together almost ten years ago now, and I still rely on all of you for so much. Physics is a team sport after all. I have to give special thanks to Michael for being such an active part of my PhD journey. Whether you were dismantling my ideas with a single sentence or helping me with some of the hardest problems I had to tackle during my studies, you have always managed to remind me that I love what I do.

To the members of the Photonics Systems Group, It has been a pleasure to work with all of you. The team spirit fostered in the PSG has created such a supportive working atmosphere. I have received so much help over the years and I hope I managed to give some guidance when I could. I would like to give particular thanks to Niamh for making me feel so welcome when I first arrived in Tyndall and for getting me off the ground in the world of 2 μm photonics.

Lastly, I would like to express my gratitude to the Irish Research Council for funding my research.

Abstract

Over the last couple of decades, photonic technologies have become an integral part of many fields of scientific research and industry. Some of these applications include, but are not limited to, optical communications, metrology and optical sensing. As the field of photonics continues to mature and develop, the diversity of its applications also expands. One of the keys to maintaining this growth is the development of technologies that enable the operation of photonic devices at different wavelengths. The near-infrared waveband has been extensively studied due to its applications in the telecommunications industry, mostly around the 1550 nm wavelength. When looking further along the IR waveband the 2 μm wavelength region is of particular interest due to its potential applications in the fields of optical communications, silicon photonics and optical sensing.

In this thesis, we develop two technologies for enabling applications and research in the 2 μm waveband. The first achievement was the realisation of a semiconductor laser based frequency comb source at 2 μm. Optical combs are becoming ubiquitous in research applications, from spectroscopy to carrier generation for coherent optical communications. Beyond laboratory application, optical combs have seen little implementation due to their cost, size and complexity. In this thesis, we develop a compact and robust comb source for the 2 μm waveband using recently developed InP based semiconductor laser sources and the gain switching modulation method. In addition to this, the first demonstration of a dual frequency comb was shown at this wavelength. This allowed for the analysis of these combs using low speed photodetectors at near real-time acquisition rates. The optical frequency combs developed could be key components in enabling optical sensing and metrology applications in the 2 μm wavelength region.

The second achievement of this thesis was the development of fibre amplifiers for the 2 μm waveband using the rare-earth element Thulium ($Tm3+$). Due to the relative immaturity of technologies at this wavelength, managing component losses and maintaining optical power is essential. Thulium doped fibre amplifiers (TDFAs) offer a broad amplification bandwidth ranging from 1650 nm-2150 nm. These amplifiers can be pumped using a variety of wavelengths, each having their benefits and weaknesses which are explored in this thesis. Through variation in pump wavelength and doped fibre length, amplifiers were developed which were optimised for wavelengths around 2 μm while utilising low pump power.

Chapter 1

Introduction

This chapter sets out to give a brief overview of the background and motivation for the research carried out in this thesis. This chapter is broken down into three sections. Section 1.1 outlines the potential applications for optical devices operating in the 2 μm waveband. The three fields discussed include optical communications, silicon photonics and optical sensing. Also included in this section is a brief overview of the field of photonics and how it evolved to become a ubiquitous part of modern technology. Section 1.2 sets out the motivation for the specific work carried out in this thesis. The goal of this thesis was to develop an optical frequency comb solution operating around the 2 μm wavelength region. The potential for these devices to impact optical communications, silicon photonics and optical sensing is also discussed. Section 1.3 outlines the main achievements and outline of each chapter in this thesis.

1.1 The 2 μm Waveband and its Applications

Since the inception of the first laser, the ruby laser in 1960 [1], lasers have become a cornerstone of modern technology. The demonstration of lasing in semiconductor materials and the development of the first continuous-wave room temperature semiconductor laser in 1970, paved the way for the field of photonics, an optical analog to electronics [2, 3]. The semiconductor laser revolutionised the field of photonics by enabling the mass production and application of small scale laser devices. From bar code scanners to cutting edge medical applications, lasers became a ubiquitous part of modern technology. Optical communications was one of the key fields to benefit from the development of the semiconductor laser. Used in combination with low loss optical fibres as a transmission medium, the first optical data link was set up in 1975 [4]. By 1980 optical telecommunications links became commercially available.

Since this revelation in optical communication technologies, much of the development in semiconductor lasers has been driven by communications applications. Beginning at 850 nm, progressing to 1330 nm and now at 1550 nm, the optical wavelength ranges developed in semiconductor laser have been focused on achieving lower loss optical communications with improving optical fibre technology [5]. In this thesis, we focus on developing technologies operating beyond these conventional communications wavelengths to the 2 μm wavelength region. In recent years there has been much interest in the 2 μm waveband due to the potential for applications in optical communications, silicon photonics and optical sensing [6, 7]. In this section, I explore these three key applications and how photonic devices operating in the 2 μm wavelength region could facilitate advancement in these three fields.

1.1.1 Optical Communications

Optical communications describes the process of sending optical signals, containing data, through optical fibre cables to an endpoint where that data can be retrieved. Almost all modern telecommunications operate in the 1550 nm window, as it is the minimum optical loss wavelength of silica fibres [8]. However, there are concerns supported by recent research that the 1550 nm telecommunications window may be approaching a "capacity crunch" due to increasing internet bandwidth consumption [9]. As data consumption

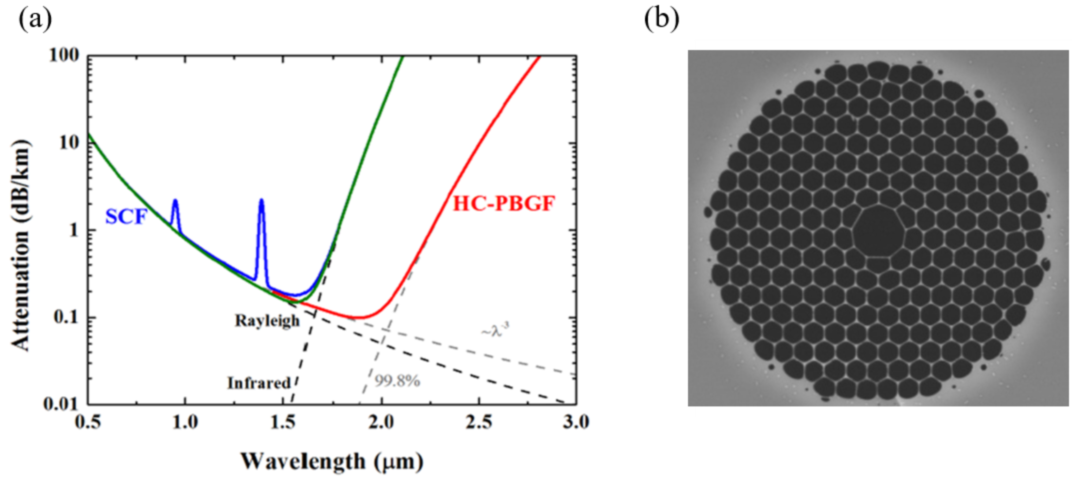

Figure 1.1: (a) Sketch of optical loss vs wavelength for standard silica fibre and HC-PBGF (b) Cross section of HC-PBGF showing the lattice structure used to contain the light in its hollow core [12].

increases through the widespread use of information-dense applications, like 4k video streaming, the number of optical data channels passing through optical fibres will also need to increase. With increasing optical power passing through silica fibres there is potential for signal breakdown due to power dependant nonlinearities in the fibre. This is sometimes referred to as the nonlinear Shannon limit, as it expands on the traditional Shannon noisy channel theorem to include fibre nonlinearities [10]. These nonlinear effects cause the properties of the optical signals passing through the fibres to be distorted to the point where data can no longer be retrieved. One potential solution to this capacity issue is to change the transmission medium to a new optical fibre with better nonlinear tolerance. One candidate for a new transmission medium is Hollow Core Photonic Bandgap Fibre (HC-PBGF) [11, 12]. This fibre consists of a hollow core surrounded by a honeycomb-like structure which enables the confinement of the optical signals in the fibre core through Bragg reflections. This is in contrast to a solid silica-based core in traditional fibre. As light is guided through an air core, theoretical predictions say that a loss of ≈0.1 dB/km can be achieved (half of current SMF), with the additional benefit of reducing the nonlinear effect ($\approx 1000\times$ lower than SMF). This would suggest that hollow core fibre can achieve much higher capacities than current solid core systems due to its increased power handling capabilities. In traditional solid core fibre, Rayleigh scattering is the main loss mechanism creating the minimum wavelength of 1550 nm [13]. In hollow core fibres, surface scattering, caused by the roughness of the inner walls of the fibre, is the primary loss mechanism. This, in theory, suggests that the new minimum loss wavelength for these fibres is around 2 μm. Steps have been taken in recent years to enable 2 μm communications [14, 15, 6], but continued development is required to achieve communications on a par with the current 1550 nm standards.

1.1.2 Silicon Photonics

In recent years silicon photonics has emerged as a platform for photonic integrated circuits (PICs) which aims to take advantage of the well-established silicon processing standards and facilities used in the complementary metal-oxide-semiconductor (CMOS) electronics industry [16, 17]. One of the goals of photonics is to see a mass implementation of optoelectronic devices, similar to the way electronics have been deployed to date. Silicon photonics holds the most promise in seeing this goal realised as it brings the photonic processing standards in line with current CMOS manufacturing practices. As well as CMOS compatibility, silicon has some desirable optical properties which can be used to create efficient on-chip optical components. High refractive index contrast between silicon and the silicon oxide cladding used in silicon on insulator (SOI) platforms is one of the key advantages. This allows for small footprint photonic circuits to be designed due to the high confinement of light in SOI waveguides [18, 19]. Although there are many benefits to the SOI platform there are two key drawbacks. First, silicon has negligible second order nonlinearities, which is a requirement for traditional electro-optic

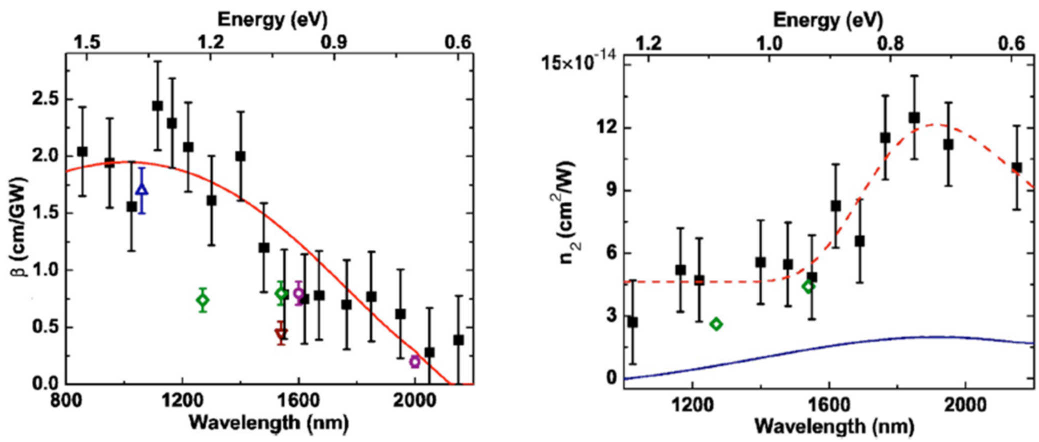

Figure 1.2: Theoretical (red) and measured (squares) results for the strength of (a) two-photon absorption and (b) Kerr nonlinearities in silicon as a function of wavelength [23].

modulation processes used in materials like Lithium Niobate ($LiNbO_3$) [20]. Due to the lack of second order nonlinearities, most of the processes used to manipulate light in silicon devices are third order nonlinear processes, primarily the Kerr effect. The Kerr effect can be used to induce processes like self-phase modulation (SPM), cross phase modulation (XPM) and four-wave mixing (FWM) [21, 22]. These processes are used to manipulate optical pulses, generate supercontinua and perform wavelength conversion.

The second drawback of the SOI platform is the high two-photon absorption (TPA) in silicon at 1550 nm. TPA is a process where the energy of two photons can be simultaneously absorbed to excite electrons in a material. This process causes problems in silicon as it creates unwanted optical loss and generates heat, which can reduce the efficiency of silicon devices. Figure 1.2 shows the theoretical and measured results for values of TPA and Kerr nonlinearity in silicon for wavelengths ranging from 850 nm-2200 nm [23]. Figure 1.2(a) shows how TPA falls off as the wavelength of light passing through silicon approaches 2 μm, reducing the optical loss and unwanted heat generation present at 1550 nm. Figure 1.2(b) shows the increasing nonlinear Kerr coefficient in silicon, peaking around 2 μm. A high Kerr coefficient translates to a lower optical power requirement to see the third order nonlinear effects. The 2 μm wavelength region could be the useful operating wavelength for devices on the SOI platform as it addresses the issue of TPA and satisfies the requirement for high 3rd order nonlinear coefficients.

1.1.3 Optical Sensing

Optical sensing encompasses the many applications in which light is used to retrieve information from an environment. Two of the key application where light has enabled advancements in sensing are Light Detection and Ranging (LIDAR) and optical spectroscopy [24]. LIDAR describes the use of laser light to monitor distances through the detection of reflected and scattered light. These systems come in a variety of designs but typically consist of a pulsed laser source and an optical receiver. Through monitoring the return time for reflected pulses, the distance of an object from the LIDAR source can be determined. In the case of more advanced coherent LIDAR systems, the Doppler shift of the light can also be monitored to determine the velocity of detected objects, often used for wind speed measurements [25, 26]. LIDAR systems are implemented in fields such as topological mapping, automated car sensing, atmospheric aerosol detection, weather metrology and many more. As these applications often operate in places where human exposure is unavoidable, eye safety is a key concern. Wavelengths above 1.45 μm are typically considered eye-safe due to the energy from these wavelengths being absorbed by the cornea thereby protecting the retina from damage. However, increasing the wavelength used by a LIDAR system negatively impacts the potential Doppler resolution of these systems, as the Doppler frequency shift is inversely proportional to the optical wavelength [27]. Operating at arbitrarily low wavelengths also comes with disadvantages including increased signal degradation due to turbulence and increased interference from scattered solar light [28]. The 2 μm waveband could be a desirable compromise between eye safety and resolution for many LIDAR applications.

The second form of optical sensing which could benefit from improvements to technologies in the 2 μm waveband is spectroscopy. Chapter 4 covers spectroscopy and its different forms in detail, but in a simple form, spectroscopy uses the interaction of light with molecules to extract information about the molecules. Absorption spectroscopy uses light to probe a sample, identifying the molecules present and their concentration based on the wavelengths of light absorbed. These absorbed wavelengths allow for the identification of molecules as each molecule has a unique absorption profile. Figure 1.3 shows some of the molecular absorption spectra present in a window around the 2 μm wavelength region. This window is selected as it can currently be covered by optical amplifiers in the 2 μm region [6]. The gases that can be detected in this window are of importance in many applications. The detection of carbon dioxide (CO_2) is a key component of atmospheric and interior air quality measurements [29, 30, 31]. Methane (CH_4) is a key contributor to greenhouse gasses [32, 33]. The monitoring of agricultural and industrial methane production continues to be an important part of atmospheric pollution management. For medical sensing, breath analysis for the presence of ammonia (NH_3) can be used for early non-invasive identification of medical issues like kidney disease [34, 35, 36]. Lastly, water vapour detection is very important in industrial applications, particularly combustion processes where water concentration can be used as an indicator for combustion efficiency [37, 38]. Beyond sensing, high water absorption holds the additional benefit of enabling laser based surgeries. With the high water concentration in human tissue, the penetration depth of light which is

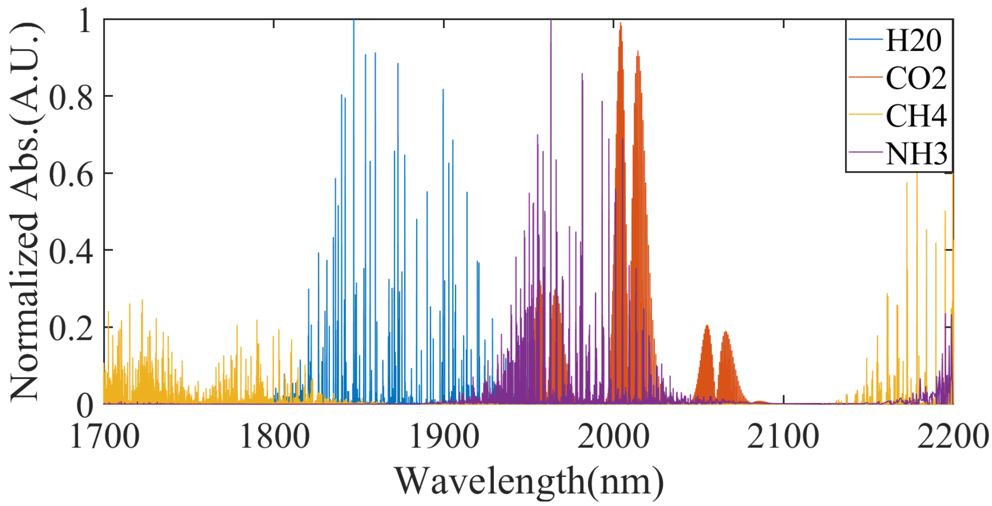

Figure 1.3: Normalised absorption profiles of molecules in a window of the 2 μm waveband.

absorbed by water is limited. This reduces excess tissue damage for laser-based surgical procedures [39]. For the wide range of applications shown above, utilisation of optical devices operating in the 2 μm waveband could result in very versatile and powerful technologies.

1.2 Thesis Motivation

The motivation for this thesis was to develop flexible optical technologies, operating in the 2 μm waveband, which could potentially enable one or more of the applications described in this chapter. The two key technologies studied were optical comb sources and optical amplifiers, which are essential building blocks required to enable photonic applications at any wavelength. The devices developed in this thesis were focused towards sensing applications, however, with modified design choices the methods and technologies could be applied in fields outside of optical sensing.

Optical frequency combs (OFCs) are an essential part of the continuously evolving field of photonics. For enabling the application of OFCs outside of a laboratory setting there are a number of issues that affect devices at all wavelengths [40]. Many of the applications where 2 μm optical technologies could see implementation are commercial in nature, such as the telecommunication and medical industry. Additionally, the realisation of ambitious sensing projects, like smart cities based on distributed sensing networks, require a commercial OFC source to be available. A commercial OFC source is preferably small in scale, simple in operation and consumes a minimal amount of power leading to a cost-effective device. In this thesis we attempt to address these requirements by developing an OFC source based on recently developed semiconductor laser sources on an Indium Phosphide platform, enabling laser emission in the 2 μm wavelength region [41]. The development of these laser sources has opened up the 2 μm wavelength region to methods and techniques which are well established for more mature 1.55 μm technologies. The primary technique explored in this thesis is gain switching, a modulation method that can be used to generate OFCs and has enabled the development of small scale OFC sources at 1.55 μm [42]. The potential of the gain switching method in combination with the aforementioned 2 μm laser sources was theoretically and experimentally explored with a focus on their potential in sensing applications.

Along with commercial applications requiring a small, simple and cost-effective OFC source, optical sensing applications benefit from devices that offer high sensing resolution and fast data acquisition times. In recent years the dual frequency comb (DFC) architecture has been developed to attempt to address these issues [43]. In theory, DFCs offer near real-time data acquisition rates with high sensing resolution in a coherent optical setup, which is important for applications where phase recovery is required, such as Doppler LIDAR. Using the OFC comb generators developed in this thesis, we explore the potential to use these devices in a DFC architecture. Through this, we attempt to demonstrate the potential of these sources as devices that can both satisfy commercial application requirements and provide high performance sensing functionality.

With the relative immaturity of optical technologies in the 2 μm wavelength region, optical loss is a persistent issue. With this in mind, the final portion of this thesis was focused on the development of a fibre amplifier that could aid in the recovery of lost optical power in 2 μm photonic testbeds. As the primary goal of these amplifiers was to recover optical loss and not to generate high power optical signal, the potential for a low power fibre amplifier tailored for amplification at 2 μm was explored.

1.3 Thesis Outline

In this chapter, the potential applications for optical technologies operating in the 2 μm waveband were shown. The motivation for the work presented in this thesis was also stated. The remainder of this thesis is outlined as follows:

Chapter 2 sets out the basic physical properties of semiconductor laser sources. The current availability of 2 μm optical sources is discussed, looking at both fibre and semiconductor laser sources. Gallium antimonide (GaSb) lasers, one of the primary semiconductor laser sources at 2 μm, is compared with the indium Gallium arsenide (InGaAs) multi-quantum well (MQW) semiconductors which were used throughout this project. The fundamental principles of optical frequency comb (OFC) generation are shown and derived from a simple Dirac comb function, demonstrating the relationship between the time and frequency domain when discussing OFCs. The process of OFC generation through gain switching of semiconductor laser sources is described. Through numerical simulation of the laser rate equations, the potential for OFC generation through gain switching of 2 μm InGaAs MQW lasers was explored. Using the results of these simulations, optimal gain switching conditions for OFC were found and used for experimental analysis in later chapters.

Chapter 3 covers the experimental analysis of gain switched OFC generation using InGaAs MQW lasers operating at 2.002 μm. Due to the limitation of currently commercially available optical spectrum analysers (OSAs) for 2 μm optical signals, much of the characterisation of the OFCs were carried out in the electrical domain. The method used to convert the optical frequencies to the electrical domain was frequency down conversion through heterodyne detection. This method is described in this chapter and how it was used to characterise OFCs in the 2 μm waveband is shown. Through the heterodyne detection method, the presence of OFCs could be detected, distinguishing gain switching regimes where OFCs were generated from regimes where continua were generated. This chapter also covers experiments in which optical injection locking (OIL) was used to restore OFC generation in gain switching regimes where a continuum was previously generated. OIL offered a significant improvement in OFC bandwidth and stability.

Chapter 4 first sets out the process of absorption spectroscopy and some of the methods used to carry out this process. Three main methods currently used in spectroscopy applications are discussed: broadband direct spectroscopy, laser spectroscopy and Michelson interferometer based Fourier transform infrared (FTIR) spectroscopy. In each case, the advantages and drawbacks of these methods are compared. The recently developed method of dual frequency comb (DFC) spectroscopy is then presented, explaining some of the advantages it may hold over the currently used methods. Using the gain switched laser sources studied in Chapter 3, a DFC architecture was set up utilising OIL and gain switching to achieve a compact, simple and robust 2 μm source. The DFC was characterised with a particular focus on comb bandwidth, spectrum acquisitions time and spectral signal to noise ratio (SNR). These parameters determine the measurement speed, resolution and sensitivity of DFC sources for potential spectroscopic applications.

Chapter 5 sets out by describing the physical properties of fibre-based optical amplifiers. The effects of energy level splitting in rare-earth atoms are covered, leading to many of the desirable properties of these elements such as broad emission bandwidths. Thulium ($Tm3+$) is the primary rare-earth element used in fibre amplifiers in the 2 μm wavelength region. In this chapter, Thulium doped fibre amplifiers (TDFAs) were developed to aid in signal amplification for the other experiments carried out in this thesis. The TDFAs were developed with a variety of configurations, focusing on pump wavelength and fibre length variations. Through optimisation of fibre length and optical pumping scheme a TDFA was developed which required relatively low pump powers to achieve optical power amplification at 2 μm.

Chapter 6 concludes this thesis, summarises the achievements of the project and sets out some avenues for future work which could be carried out to further the development of technologies in the 2 μm waveband.

Chapter 2

Optical Frequency Comb Generation at 2 μm

This chapter will explore the generation of optical frequency combs (OFCs) using semiconductor laser diodes operating in the 2 μm wavelength region using the gain switching modulation technique. Section 2.1 will describe the principles of laser operation and the design of a semiconductor laser for operation around 2 μm. Section 2.2 sets out the general definition of an OFC including its key properties in the frequency and time domain. Section 2.2 sets up a basic mathematical derivation for the relationship between the time domain optical pulses and frequency domain OFCs. This offers insight into the key parameter of the optical field in the time domain and how they can be varied to produce an optimised frequency comb. Section 2.3 reviews the current methods used for OFC generation in the 2 μm wavelength region, discussing their advantages and disadvantages. This section also describes the gain switching modulation technique and how it is used to generate short optical pulses by taking advantage of the nonlinear response of optical carriers to an applied RF modulation voltage. Section 2.4 describes a numerical model, based on the diode laser rate equation, used for the simulation of gain switched frequency comb generation in the 2 μm laser sources used throughout this thesis.

2.1 Laser Sources at 2 μm

In an atom, electrons may occupy only discrete energy levels due to the quantum mechanical nature of bound particles [44]. Electrons in an atom, with no external energy source, occupy their ground energy state. In the ground state, the electrons in the atom are occupying their lowest available discrete energy level and are considered to be stable. In the presence of an energy source, these electrons can be promoted to a higher discrete energy level. This is called the excited state and is an unstable electron configuration. As this new electron configuration is unstable, the electron will eventually fall back to its ground state. The energy lost by the electron falling to the ground state is conserved through radiative or non-radiative processes. A non-radiative recombination process is one in which the energy lost from the excited electron is conserved through phonons. Phonons are quantised vibrational energies describing vibrations in an elastic collection of atoms [45]. When the energy is conserved through the emission of a photon, a quantised packet of electromagnetic radiation, the recombination process is called radiative. In this scenario, an electron can spontaneously fall to the ground state, emitting a photon with a random phase and direction. This process is called spontaneous emission [46]. If a photon with energy equal to the difference between the excited electron state and the ground state is incident on the excited atom, it can cause the electron to fall to the ground

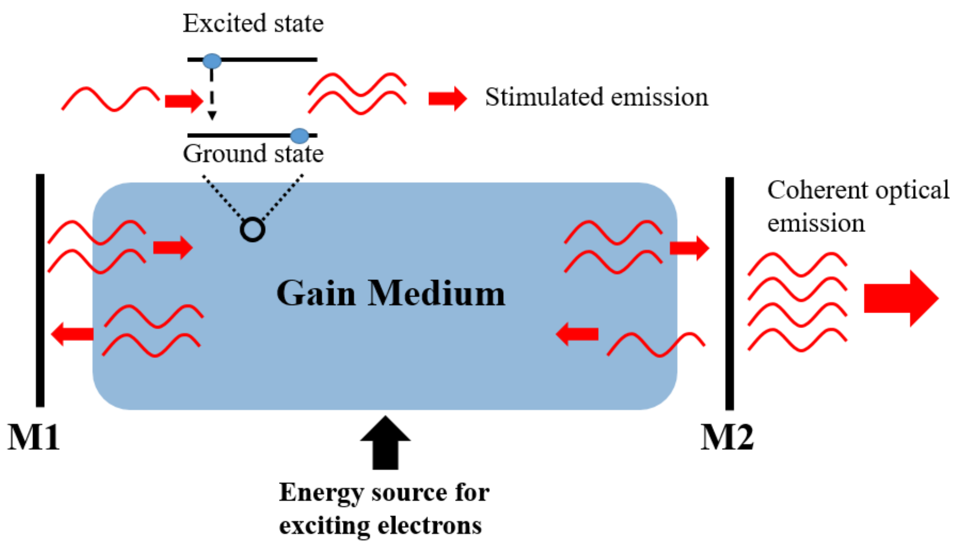

Figure 2.1: Diagram of basic laser showing an excited gain medium with an optical cavity created by mirrors M1 and M2, undergoing stimulated emission processes.

state emitting a photon with the same phase, frequency and direction as the photon which caused the emission. This process is called stimulated emission [47]. Stimulated emission is the key process for light amplification in laser sources, hence the name laser ("Light Amplification by Stimulated Emission of Radiation") [48]. A laser, in its simplest form, is a device that consists of a gain medium, a method for exciting the electrons in that medium and an optical cavity, see Fig. 2.1. In combination, this setup allows for stimulated emission to circulate through the gain medium causing a chain reaction of emissions that are all coherent, i.e. have the same phase and wavelength. Cavity resonance is achieved by selecting the distance between the cavity mirrors to generate standing waves for the desired lasing frequency. Due to one of the mirrors (M2) in the optical cavity being only partially reflective, some of this coherent light escapes, producing the laser beam. The wavelength of the light produced by a laser is dependant on the energy gap between the excited state and the ground state, as the energy conserved through the photon is equal to the energy gap. Through the selection of gain medium material, a laser can be designed to emit at many wavelengths from ultraviolet light up to far-infrared.

Current gain media operating in the 2 μm wavelength region come in two distinct varieties. The first form of gain media used in the 2 μm range are the semiconductor materials Gallium Antimonide (GaSb) and strained Indium Gallium Arsenide (InGaAs). The processes involved in light generation from these semiconductor materials are covered in the coming sections in this chapter, where the advantages and disadvantages of each material will also be explored. The second gain material used is rare-earth-doped glass fibre, which relies on rare-earth elements to generate emission at 2 μm. The two rare-earth elements with this emission wavelength are Thulium (Tm3+) and Holmium (Ho3+) [49]. These lasers use an optical pump as the method for electron excitation and an optical fibre based gain medium. The processes involved in lasers using this gain medium are covered extensively in Chapter 5.

2.1.1 Band Structures

The energy levels in single atoms are discrete, however, when bonded into a solid or gas, broadening of the energy levels occurs. In semiconductors, this broadening is prominent due to the covalent bonds formed. When atoms are covalently bonded they form bonding and anti-bonding orbitals with different energies, allowing for the electrons to occupy non-identical energy states. As the number of bonded atoms increases, the number of required unique energy levels also increases, resulting in orbital energy levels being split many times to form broad energy bands. In semiconductors, these bands are split into conduction and valence bands with an energy gap between the two, which can't be occupied by electrons. This gap is referred to as a bandgap. The valence band describes the energy levels which would be fully occupied in a minimum energy system, i.e at absolute zero. The conduction band is the converse, being empty in a minimum energy system. Semiconductors and insulators both have a bandgap in their energy structure but semiconductors have a bandgap small enough to allow for electrons to occupy the conduction band in a non zero temperature system. When electrons from the valence band occupy the conduction band, their vacancy from the valence band leaves a positive charge, called a hole. Semiconductor lasers use the bandgap to generate photons through the described stimulated emission process, now describing the recombination of electrons from the conduction band and holes in the valence band.

Figure 2.2 shows the stimulated emission process between semiconductor conduction and valence bands in two types of band structure. When selecting semiconductor materials to construct laser gain media the bandgap energy determines the wavelength of the light the laser can emit. For a laser to be an efficient producer of light, the semiconductor material used must have a direct

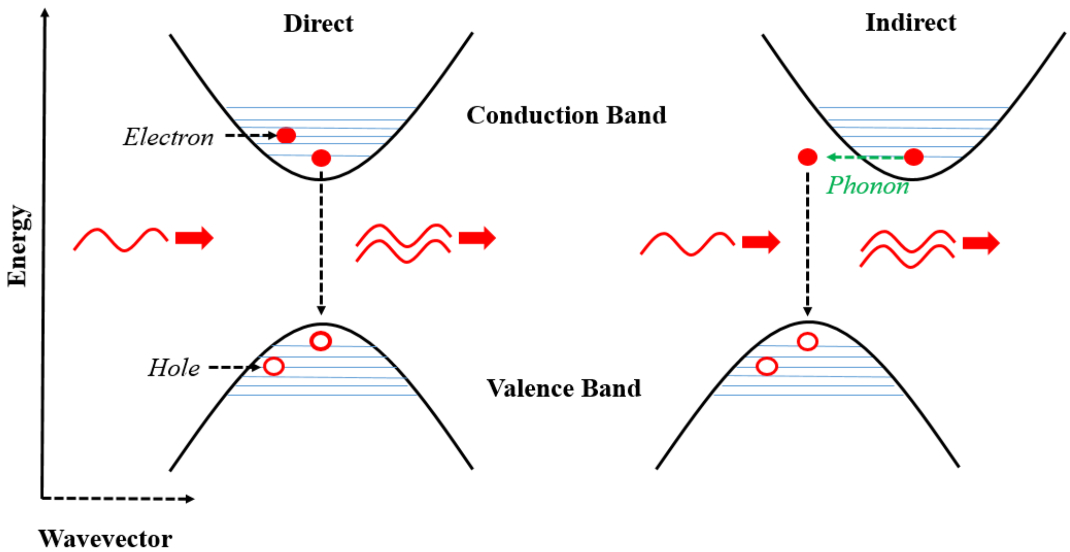

Figure 2.2: Stimulated emission process for direct (left) and indirect (right) bandgap semiconductors.

bandgap. In Fig. 2.2, the band structure for a direct (left) and indirect bandgap (right) semiconductor is shown. The x-axis, wavevector, describes the electron momentum in the bands. For a direct bandgap semiconductor, the valence and conduction band electrons have the same momentum, resulting in vertical transition in Fig. 2.2. A vertical transition in this case describes a process that only produces a photon in the electron transition. For optical emission across the bandgap to occur in indirect bandgap materials, the momentum difference of the electrons in the conduction and valence bands needs to be conserved. When stimulated emission occurs at the bandgap energy in these materials, the excess momentum is conserved in phonons in the material. This form of phonon-assisted stimulated emission is much less efficient and produces unwanted effects like heat generation. For this reason, semiconductor lasers are typically constructed of direct bandgap materials.

2.1.2 Semiconductor Laser Structure

Semiconductor materials can have additional elements added to them to increase their overall electron or hole concentration. This process is called doping and is used to create p-type (hole excess) and n-type (electron excess) semiconductors. Semiconductor laser sources use what is called a p-i-n diode structure, where an undoped semiconductor, referred to as intrinsic, is sandwiched between a p-type and n-type semiconductor, Fig. 2.3. When a current is applied across this diode, electrons from the n-type semiconductor recombine with holes from the p-type semiconductor across the intrinsic region. This recombination generates light which is reflected in the intrinsic region through mirrors at the intrinsic region facets, creating stimulated emissions and inducing lasing. It is typically desirable to design a laser source where the p-type and n-type semiconductor materials are different to the material in the intrinsic layer. Having different materials around the intrinsic layer increases the confinement of the light in that region due to the refractive index difference between the materials. The confinement of the electrons is also increased due to the bandgap difference between the layers. Multi-layer semiconductor devices made of different semiconductor materials are called heterostructures.

Through material selection, a semiconductor laser can be designed to emit at wavelengths in the visible to the mid-IR regions. Figure 2.4 shows a plot of semiconductor material bandgap energies vs lattice constant [50]. The lattice

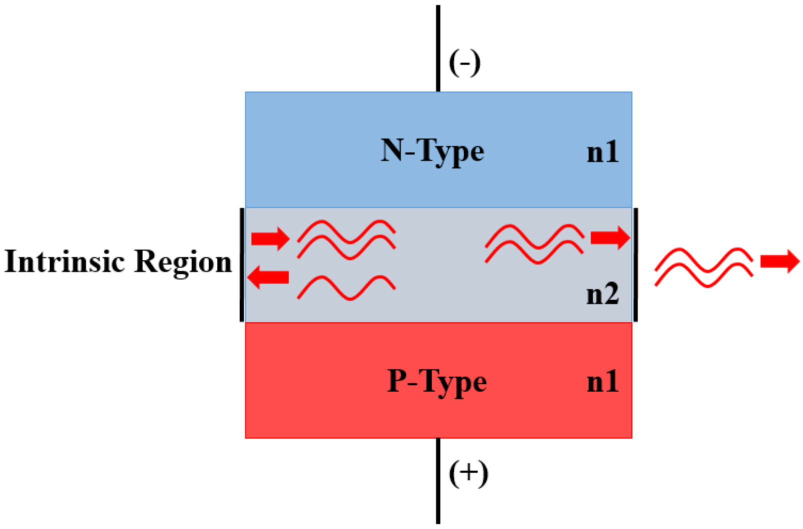

Figure 2.3: Diagram of a p-i-n laser diode with light confined in the intrinsic region by polished mirrors at the laser edges and the refractive index difference between n1 and n2.

constant describes the dimensions of the lattice of atoms bonded together in a solid. For different semiconductor materials to be grown on top of one another, the materials must be lattice-matched, i.e. have the same lattice constant. When lattice mismatch is present between two semiconductor layers, either strain is induced between the two materials or dislocation occurs [51, 52]. For large lattice mismatch, irregular bonding patterns form between the two materials, creating bonding site dislocation. Materials bonded in this way are said to have a high amount of defects and to have poor electronic-device characteristics [53]. In the case of a slight lattice mismatch, strain is induced between the two layers, slightly altering the material structure and changing the materials bandgap energy in the process. Strain is a property used in many lasers to purposely change the band energy of the selected material but must be carefully managed as not to cause unwanted defects in the laser materials. Looking at Fig. 2.4 and considering potential materials for emission in the 2 μm wavelength region, there are two candidates. First, Gallium Antimonide (GaSb) has been used as a 2 μm laser material since the 1980s [54]. In more recent years InGaAs laser sources operating at 2 μm have been developed, grown on an InP platform. When compared to GaSb, InP based laser technologies are attractive due to their lower cost and maturity of InP processing technologies [41]. These lasers offer performance and functionality which is similar to that of laser sources

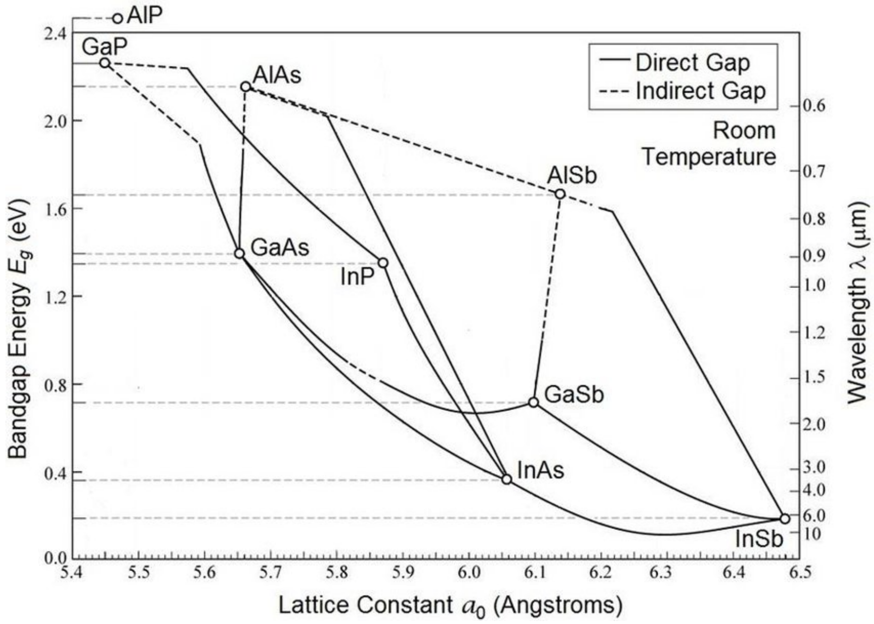

Figure 2.4: Plot of semiconductor bandgaps/wavelength vs lattice constant [50].

operating at more traditional wavelengths, with low threshold current, low noise and high stability. In this thesis, we extensively use these InGaAs laser sources to enable advances in 2 μm optical technologies.

2.1.3 InP Based Multi-Quantum Well Laser Design

The laser diodes used for experiments in this thesis were designed by Eblana Photonics and are based on an MQW active region grown on an InP platform. These lasers use a compressively strained multi-quantum well (MQW) InGaAs active region to produce emissions ranging from 1700 nm to 2100 nm [41]. MQW laser sources use an active region consisting of a heterostructure of thin alternating layers called wells and barriers. The alternating bandgap energies of these materials, InGaAs in the case of the lasers used in this thesis, results in the creation of potential energy wells. The carriers in the active region are then subject to quantum confinement in these wells, reducing the density of states in the active region. This leads to many desirable properties such as low threshold current, improved temperature stability and lower spectral bandwidth [55]. To achieve optical emission in the 2 μm wavelength region using an InGaAs MQW active region, mechanical strain is introduced between the material layers. By varying the Indium concentration in the InGaAs quantum wells, the lattice constant of the material is changed, leading to

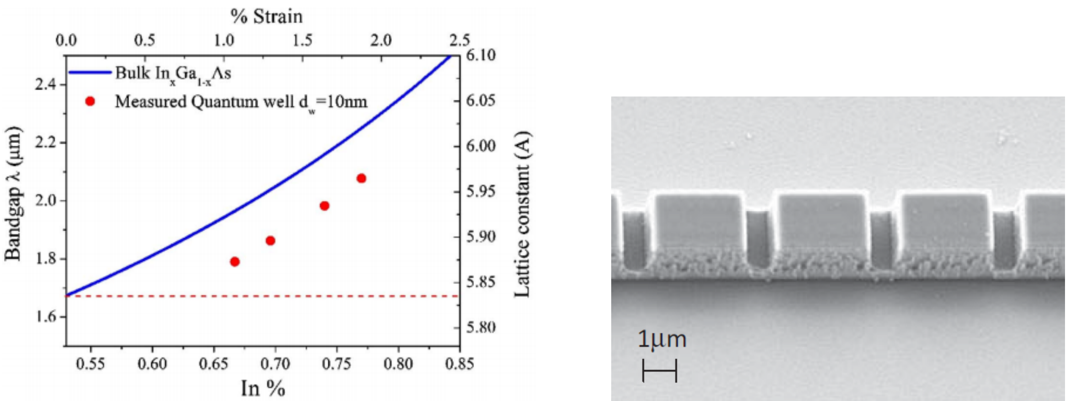

(a) (b)

Figure 2.5: (a) Strain and bandgap variation for increasing indium concentration in InGaAs MQW laser (b) SEM image of a slotted waveguide structure in DM laser [41].

strain between the active region layers. This results in a change of bandgap energy in the quantum wells. Through varying the Indium concentration from 0.67% to 0.78% an emission wavelength up to 2.1 μm can be achieved in the quantum wells, as shown in Fig. 2.5(a). As the strain between the semiconductor layers is increased, the number of defects in the device also increases, limiting the maximum strain that can be introduced into the devices.

The MQW lasers used in this thesis were based on a Fabry-Perot laser cavity, which allowed for the propagation of many laser modes due to the cavity length. As single-mode operation was desirable, the laser cavity needed to be modified to suppress all modes other than the desired emission wavelength. The lasers achieve single-mode operation through discrete mode technology [56]. This is done by introducing refractive index perturbations in the form of etched slots in the lasers ridge waveguide, as seen in Fig. 2.5(b) [57]. This causes feedback in the waveguide channel to propagate a specific optical mode decided by the spacing and depth of the slots in the waveguide. The lasers used in this thesis were constructed with In0.75Ga0.25As/In0.53Ga0.47As MQW structure grown on an InP substrate. The MQW structure consisted of three compressively strained 8 nm thick quantum wells and four lattice-matched 15 nm thick barriers.

2.2 Optical Frequency Combs

An optical frequency comb can be described as a laser spectrum consisting of a series of equidistant discrete optical frequencies [58], Fig. 2.6(b). In the time domain, this is represented by a series of equally spaced optical pulses with a fixed phase relationship, Fig. 2.6(a). The spacing between comb lines in the frequency domain is determined by the repetition frequency (f_{rep}) of the optical pulses generated. There is a slight offset induced in the frequency comb due to the evolution of the optical phase and group velocity of each pulse packet. This offset is called the carrier-envelope offset [59], which is a constant value due to the fixed phase evolution of the optical pulses, see $\Delta\phi_{ceo}$ in Fig. 2.6.

Optical frequency combs have become an essential tool in many fields of research including telecommunications [60], optical clocks [61], metrology [62], distance ranging [63] and optical sensing [43, 64, 65]. Along with the wide number of applications that implement frequency combs, there are many methods used to generate them [40]. Some examples include mode-locked lasers [66], micro ring resonators [67], fibre oscillators [68] and quantum cascade lasers (QCLs) [69].

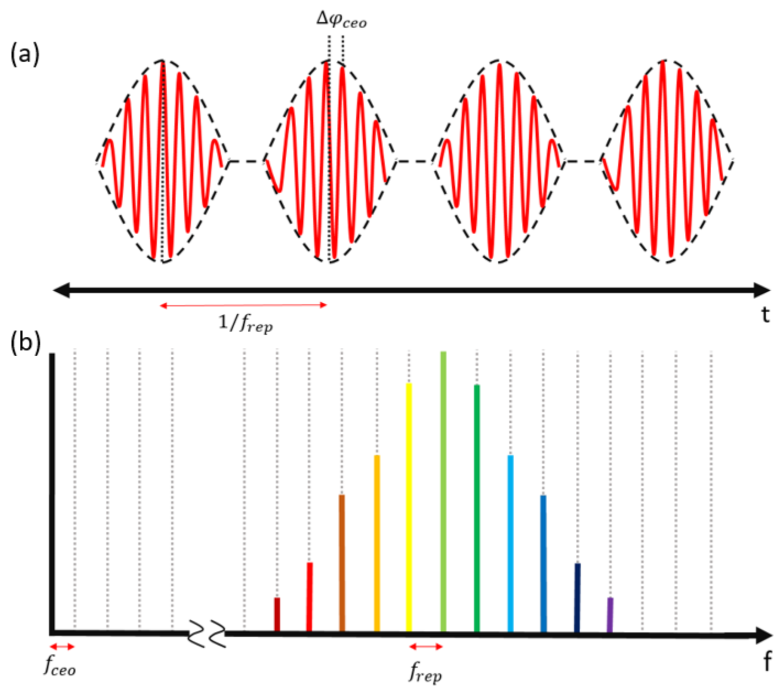

Figure 2.6: Optical frequency comb in (a) the time domain and (b) the frequency domain.

2.2.1 Theoretical Description of Optical Comb Generation

When generating an OFC it is often beneficial to think of the comb in the time domain as a series of optical pulses. Understanding the relationship between the time domain and frequency domain when generating OFCs offers insight into the effect of the optical pulse parameters on the OFC produced. This is a non-trivial relationship but we can approximate the relationship using the Fourier transform of an infinite series of identical pulses. For this scenario, it is assumed that the pulses produced are identical and have the same phase. In later simulations, the effect of phase evolution will be taken into account. The first step of the derivation is to look at the Fourier transform of a Dirac comb function. Then using a convolution of this function with the profile of one Lorentzian pulse, chosen to emulate a laser pulse, a pulse train function will be generated. The Fourier transform of this pulse train can be taken to approximate the frequency spectrum produced by a series of laser pulses. This in turn will show the relationship between the profile of a single pulse and the frequency comb it produces.

2.2.2 Dirac Comb Fourier Transform

A Dirac comb is a function in the time domain describing an infinite series of Dirac delta functions separated by some interval as shown in Fig. 2.7. A dirac comb function is defined as:

$$III(t) = \sum_{n=-\infty}^{\infty} \delta(t - nT) \tag{2.1}$$

where T in the interval between each delta function. As this is a periodic function it can be represented as a Fourier series:

$$III(t) = \sum_{n=-\infty}^{\infty} C_n e^{i2\pi nt/T} \tag{2.2}$$

Solving for the Fourier coefficient, C_n, over one interval T:

$$C_n = 1/T \int_{T/2}^{-T/2} III(t)dt = 1/T \int_{T/2}^{-T/2} \sum_{n=-\infty}^{\infty} \delta(t - nT)dt \tag{2.3}$$

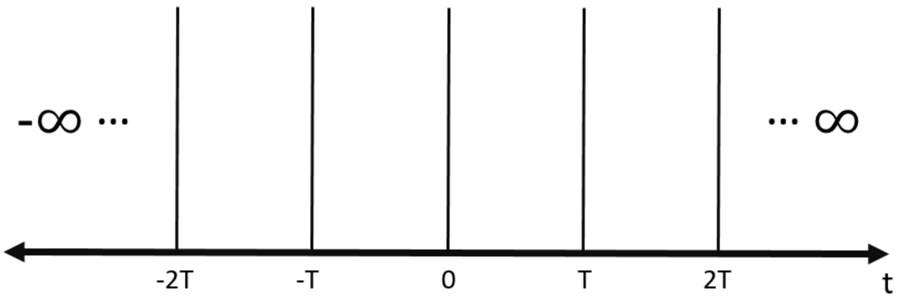

Figure 2.7: Dirac comb function, III(t), showing an infinite series of Dirac delta function separated by interval T in the time domain t.

As we are only integrating over 1 interval $n = 0$. C_n can then be derived as:

$$C_n = 1/T \int_{T/2}^{-T/2} \delta(t)dt = 1/T \tag{2.4}$$

Now we derive the Fourier transform of this Fourier series to represent the Dirac comb function in the frequency domain.

$$F[III(t)] = \int_{-\infty}^{\infty} 1/T \sum_{n=-\infty}^{\infty} e^{i2\pi nt/T} e^{-i\omega t/T} dt \tag{2.5}$$

where $\omega = 2\pi f$, and f is the frequency. Eqn. 3.5 simplifies down to:

$$F[III(t)] = III(\omega) = 1/T \sum_{n=-\infty}^{\infty} \delta(\omega - 2\omega_0) \tag{2.6}$$

This shows that the Fourier transform of a Dirac comb in the time domain with interval T is a Dirac comb in the frequency domain with interval $2\pi/T = \omega_0$, i.e. $III(\omega)$.

2.2.3 Optical Comb Description Through Convolution

A pulse train is a series of identical pulse profiles separated by some interval in the time domain. Figure 2.8 shows a simple way of defining this pulse train function using a convolution between a Dirac comb and a single pulse profile,

$f(t)$. This pulse train through convolution is defined as:

$$E(t) = III(t) * f(t) \tag{2.7}$$

where $III(t)$ is a dirac comb and $f(t)$ is the profile of a single optical pulse in the time domain. To see the resultant comb generated in the frequency domain by the pulse train, $E(t)$, we get the Fourier transform of $E(t)$:

$$F[E(t)] = F[III(t) * f(t)] \tag{2.8}$$

The convolution theorem states that the Fourier transform of a convolution of two functions can be represented by the product of the Fourier transforms of each function individually:

$$F[E(t)] = F[III(t)]F[f(t)] \tag{2.9}$$

We have already derived the expression for the Fourier transform of a Dirac comb in equation 2.6. This gives us the solution:

$$F[E(t)] = III(\omega)f(\omega) \tag{2.10}$$

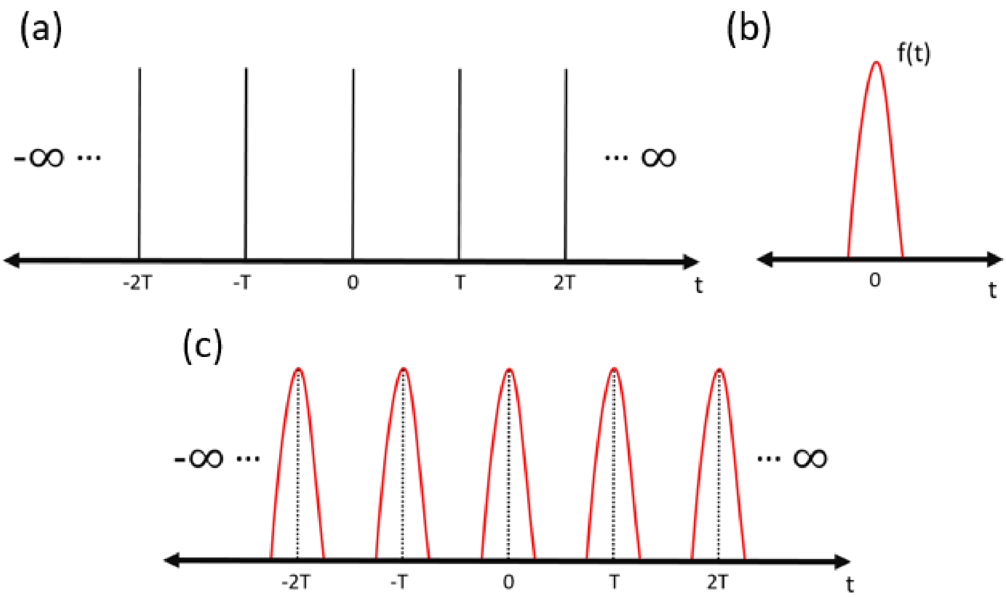

Figure 2.8: Plot of the (a) Dirac comb; (b) Lorentizian pulse profile and (c) Convolution of the Dirac comb and Lorentizian pulse profile.

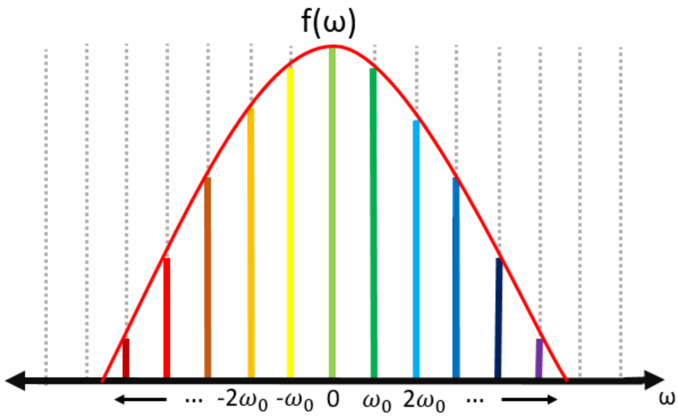

Figure 2.9: Comb function in the frequency domain with profile described by $f(\omega)$.

This shows that the Fourier transform of a pulse train is the product of the Fourier transform of a single pulse and the Fourier transform of the underlying Dirac comb. This can be seen in Fig. 2.9. We can see from this relationship that the profile of a single pulse, $f(t)$, describes the full profile of the optical comb it produces, $f(\omega)$. Using this relationship we can derive desirable optical pulse properties to produce optimal frequency combs. For example, the Fourier scaling theorem states that reducing the width of a pulse in the time domain creates a broader spectrum in the frequency domain. Therefore, generating narrow optical pulses in the time domain will produce a frequency comb which is a broader spectrum in the frequency domain. This relationship is the basis for much research in the improvement of optical combs using pulse compression techniques.

2.3 Frequency Comb Generation in the 2 μm Waveband

To date, there has been limited development of comb sources operating in the 2 μm [65]. Much of the focus has been directed towards the communications waveband, around 1550 nm, due to established applications and the availability of technologies required for comb generation and analysis. In this section, we discuss the current methods used for comb generation in the 2 μm waveband and how gain switching of the lasers developed in Section 2.1.3 could offer a simple and robust method of comb generation around 2 μm.

2.3.1 OFC Generation Methods at 2 μm

As described in Section 2.2, an OFC can be generated through the production of an optical pulse train with a fixed phase relationship between the pulses. Until recently, the primary laser technology used to produce optical emission in the 2 μm waveband were fibre-based lasers. These lasers consist of optical fibre doped with an element that has an emission wavelength in the 2 μm wavelength region [49, 70]. The availability of fibre-based laser sources led to the development of fibre oscillator and dissipative soliton fibre lasers for OFC generation [71, 72, 73]. These devices typically use a pulsed or continuous wave (CW) seed laser in combination with fibre compression stages to generate ultra-short pulses, with pulse widths in the picosecond to femtosecond region. These devices offer a broad comb spectrum of high power frequency tones but require a large amount of input power to achieve narrow pulsed emission. The optical power alone is on the order of watts, making this a prohibitive technology for low power applications. Fibre-based comb sources also lack the potential to be integrated into small footprint photonic integrated circuits (PICs). With these limitations, fibre oscillator based OFC generators will likely not see implementation outside of laboratory settings.

With the cost, size, power consumption and complexity being the main issues limiting the implementation of OFCs outside of laboratory settings [40], strides were made to attempt to find a semiconductor laser-based solution for OFC generation at 2 μm. Gallium Antimonide (GaSb) semiconductor lasers have opened up the potential for semiconductor diode lasers to stretch their emission into the 2 μm wavelength region and beyond [74, 75]. Laser sources based on this material have shown some promise as frequency modulated (FM) comb sources [76]. FM sources do not produce the same pulse train as mentioned in previous sections, instead, simultaneously supporting the generation of multiple CW wavelengths in the laser cavity [77]. Thus far, the OFC sources developed using GaSb based lasers have relied on the multimode generation of light using Quantum Cascade Lasers (QCLs) with high bias voltages far above the laser threshold. One of the main drawbacks of these devices is the high lasing threshold, approaching 100 mA [78, 69], with the desired comb emission only occurring around 300 mA-400 mA biases. There are also single mode GaSb laser sources available with desirable properties, such as low lasing threshold [79]. As of yet these have not been utilised for OFC generation.

In this thesis we used the gain switching modulation method in combination with recently developed III-V semiconductor diode lasers operating in the 2 μm wavelength region, see Section 2.1.3, to generate OFCs from an optical pulse train. These devices, in theory, offer the integration potential of the GaSb devices described above, while having a more traditional low threshold current and operating current in the tens of milliamps region.

2.3.2 Gain Switching

Gain switching is a method used to generate optical pulses by directly modulating the current supplied to a laser diode source. It was developed in the late 1970s as a means of generating picosecond optical pulses [80, 81, 82, 83]. To date this mechanism is still used for pulse generation in many fields due to its relative simplicity and integration potential [84, 85, 86]. Gain switching is achieved by applying an RF modulation voltage, in the form of an amplified sine wave, to a laser diode that is biased away from the laser threshold. Figure 2.10 shows a visualisation of the gain switching method. Gain switching occurs when the modulation amplitude is large enough to induce the nonlinear carrier response seen in Fig. 2.10(b). As the modulation current causes the carrier density to suddenly increase, there is a delay before stimulated emission can begin. Once stimulated emission starts, lasing occurs

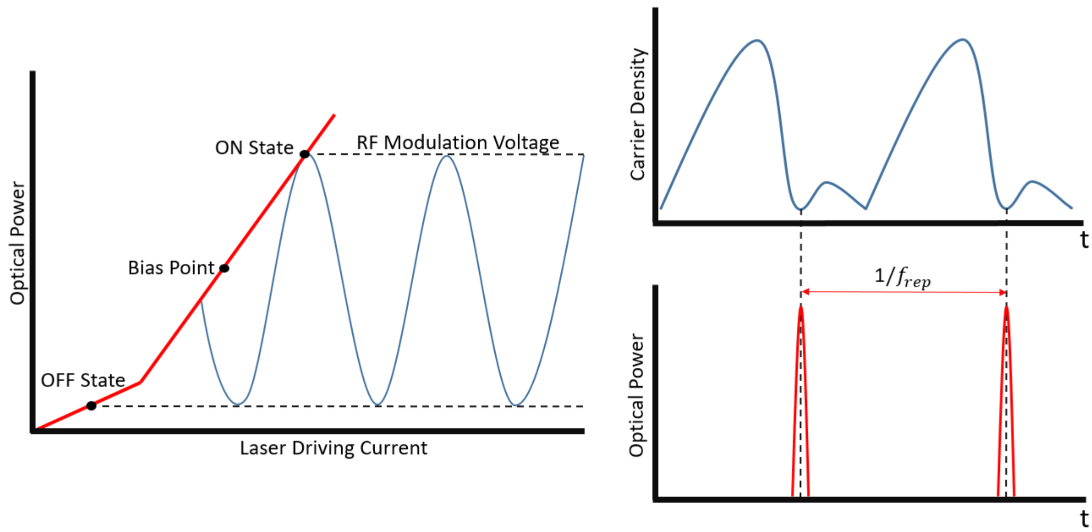

Figure 2.10: Gain switching method for pulse generation from the perspective of the (a) Laser LI curve showing where the laser is biased and the modulation applied to the laser around the bias point; (b) Carrier density evolution; (c) Optical power variation over time.

which quickly depletes the excited carriers. stimulated emission can begin. Once stimulated emission starts, lasing occurs which quickly depletes the excited carriers. This causes an optical pulse to be produced. Once the pulse depletes the carriers below the lasing threshold the pulse ends. This process of delayed lasing onset and rapid carrier depletion is what allows gain switching to produce pulses with a shorter duration than the applied modulation frequency. In a direct modulation regime where gain switching does not occur, the laser will simply switch on and off in conjunction with the applied modulation voltage and no nonlinear response will be seen in the carrier density. In certain gain switching regimes, which will be elaborated on later, the phase relationship between pulses generated can be fixed. This allows gain switched lasers to be used to generate optical combs [87, 88]. Gain switched diode lasers are an attractive option for comb sources as they are robust, integrable and have a simplistic operating mechanism.

2.4 Numerical Simulation of Gain Switching Process in 2 μm Lasers

In this section, we numerically simulate the potential of the 2 μm MQW DM laser sources to generate optical frequency combs. These simulations were carried out using the standard laser diode rate equations in combination with Langevin noise terms for the simulation of pulse to pulse phase noise. Section 2.4.1 simulates the turn-on dynamics of the laser sources in the absence of noise terms. Through this, the relaxation oscillations (ROs) were predicted for varying bias currents. The nonlinear response of the laser carriers and photons in the presence of a modulated current were also shown. Section 2.4.1 simulates the optimal driving conditions for OFC generation in the presence of stochastic noise in the laser sources.

2.4.1 Relaxation Oscillation and Pulse Generation

As the laser sources from Section 2.1.3 had not been used as comb sources in the past, we first set out to simulate their potential as comb sources and optimal operating conditions. The lasers were simulated using the standard laser diode rate equations [89, 90, 91, 92]. The rate equations (2.11)-(2.13) describe the evolution of the carrier density (N), photon density (S) and phase

(ϕ) of the laser source.

$$\frac{dN}{dt} = \frac{I}{eV_{act}} - R(N) - \frac{v_g g(N(t) - N_{th})S(t)}{1 + g_c S(t)} + F_N \tag{2.11}$$

$$\frac{dS}{dt} = (\frac{\Gamma v_g g(N(t) - N_{th})S(t)}{1 + g_c S(t)} - \frac{1}{t_p})S(t) - \beta \Gamma B N^2(t) + F_S \tag{2.12}$$

$$\frac{d\phi}{dt} = \frac{\alpha}{2}(\Gamma v_g g(N(t) - N_{th}) - \frac{1}{t_p}) + F_\phi \tag{2.13}$$

The symbols here take on their usual meaning which can be found in table 2.4.1. F_N, F_S and F_ϕ are stochastic noise terms that are ignored for the first portion of the simulation during the treatment of the above equations as ordinary differential equations. This was done to improve computation speed for simulations where the noise performance of the lasers was not required. The noise terms will be included in later simulations when the above equations are treated as stochastic differential equations, requiring different algorithms to achieve numerical solutions. Here, $R(N)$ describes non-radiative and radiative recombination in the laser which is broken down into three processes and their relative contribution dependant on the carrier density N:

$$R(N) = AN(t) + BN^2(t) + CN^3(t) \tag{2.14}$$

where A is the non-radiative recombination coefficient, B is the bimolecular recombination coefficient and C is the Auger recombination coefficient. Non-radiative recombination occurs when electrons in the conduction band fall to the valence band generating a phonon instead of a photon. Bimolecular recombination is a spontaneous process in which a conduction band electron spontaneously falls to the valence band emitting a photon. Lastly, Auger recombination describes a two carrier interaction where one carrier non-radiatively falls from the conduction band to the valence band with the energy loss conserved through exciting an electron in the conduction band to a higher energy in the conduction band [93]. With the above information, a MATLAB program was written in order to generate a number of results. First, we simulate the Light–Current (LI) curve of the laser source for currents (I) ranging from 0 mA to 80 mA. The rate equations were numerically solved using the ode45 function in MATLAB, which used the Runge-Kutta 4th order method for solving ODEs.

Laser Parameters for Simulations		
Symbol	Description	Value
e	Electron Charge	1.602×10^{-19} (C)
h	Planck Constant	6.626074×10^{-34} (JHz^{-1})
v_g	Group Velocity	9.368×10^{7} (ms^{-1})
f	Laser Frequency	1.4985×10^{14} (Hz)
V_{act}	Active Region Volume	2.4×10^{-17} (m^{3})
β	Spontaneous emission factor	1×10^{-4}
N_0	Carrier Density at Transparency	1×10^{24} (m^{-3})
α	Linewidth Enhancment Factor	4.1
t_p	Photon Lifetime	4.8281×10^{-12} (s)
g	Differential Gain Coefficient	3×10^{-20} $(m^{3}s^{-1})$
Γ	Confinement Factor	5%
g_c	Gain Compression Factor	3×10^{-20} (m^{3})
η_f	In-Fibre External Quantum Efficiency	7%
A	Non-Radiative Recombination	1.2×10^{9} (s^{-1})
B	Bimolecular Recombination	1×10^{-6} $(m^{-3}s^{-1})$
C	Auger Recombination	4×10^{-41} $(m^{-6}s^{-1})$

Figure 2.11 shows the simulated and experimental LI curves. The simulation accurately describes the LI curve at most current levels, lacking some accuracy when it comes to describing higher currents. The roll-off is likely due to thermal effects caused by self-heating. As we will be operating these lasers at low bias currents, self-heating at high biases was not taken into account.

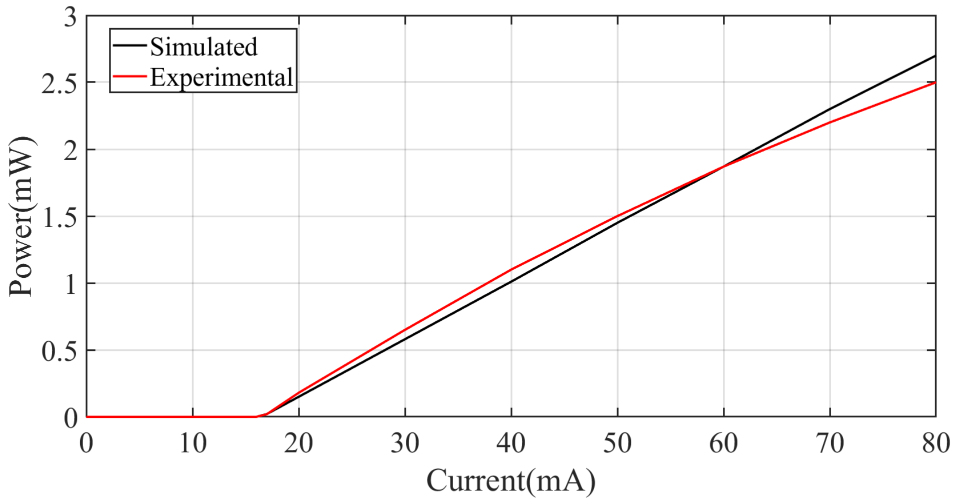

Figure 2.11: Simulated (Black) and experimental (red) LI curves for InGaAs MQW DM laser source operating at 2 μm.

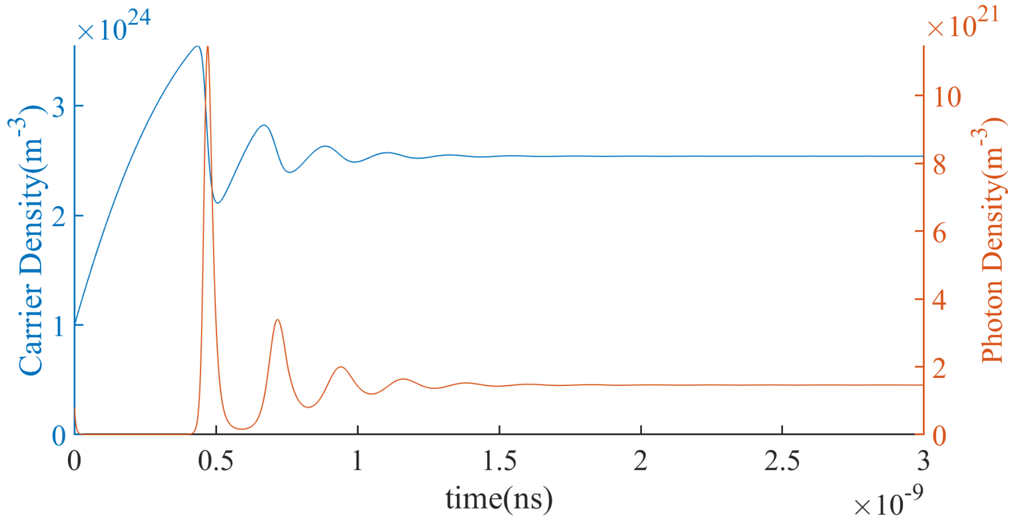

Figure 2.12: Simulation of turn on dynamics of laser carriers and photons in the cavity.

Looking at the simulated carrier and photon dynamics in the turn-on process of the laser biased at 40 mA, Fig. 2.12, we can see the delayed onset of the photon emission resulting in a sudden spiking at 0.5 ns followed by a damped oscillation to the laser steady-state. The damped oscillation is referred to as the relaxation oscillation. Relaxation oscillations occur when the upper state lifetime of a laser is much longer than the laser resonator damping time [94]. The frequency of relaxation oscillations varies with laser pump current and can be found using Eqn. 2.15:

$$f_{RO} = \frac{1}{2\pi}\sqrt{\frac{v_g g S_0}{t_p}} \tag{2.15}$$

where v_g is the group velocity, g is the gain coefficient, t_p is the photon lifetime and S_0 is the steady state photon density. Using this equation, the relaxation oscillation frequency for the 2 μm laser sources was calculated for bias currents from 20 mA to 50 mA. The results for the relaxation oscillation frequencies are shown in table 2.1. The carrier density evolution for increasing bias currents is show in Fig. 2.13.

When the bias current applied to the laser is modulated with a sinusoidal

Table 2.1: RO frequencies at different bias currents.

Current	20 mA	30 mA dB	40 mA	50 mA
f_{RO}	1.46 GHz	3.32 GHz	4.45 GHz	5.37 GHz

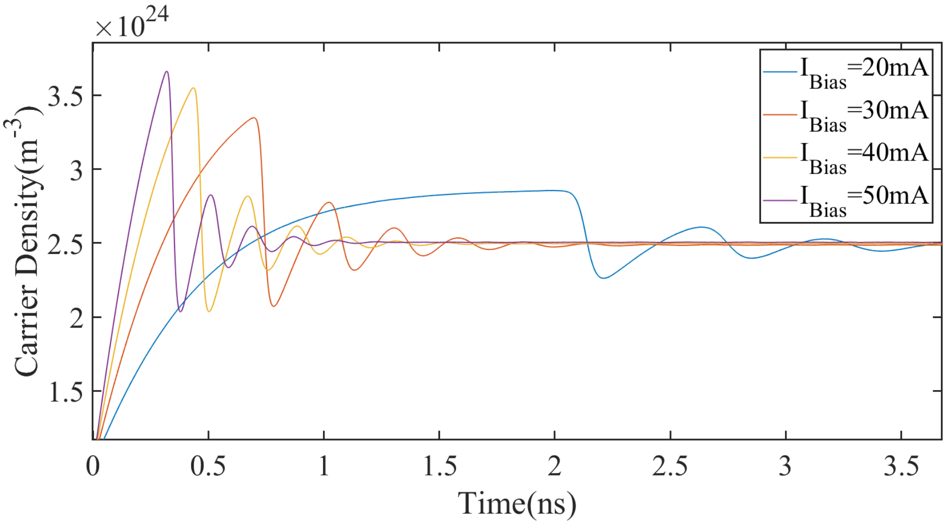

Figure 2.13: Relaxation oscillations in the carrier density for increasing bias currents.

signal, the spiking effect shown in Fig. 2.12 can be repeated over the repetition rate of the applied modulation current. It is this repeated spiking of the photon density which defines the gain switching modulation method. The modulation current (I) can be described by:

$$I = I_{bias} + I_{mod} sin(2\pi f_r t) \tag{2.16}$$

where I_{bias} is the bias current, I_{mod} is the modulation current and f_r is the modulation frequency. Applying this modulation current to Eqn. 2.11-2.13, with 40 mA bias current, 30 mA modulation current and 3 GHz modulation frequency we get, Fig. 2.14. In this scenario, the nonlinear response of the

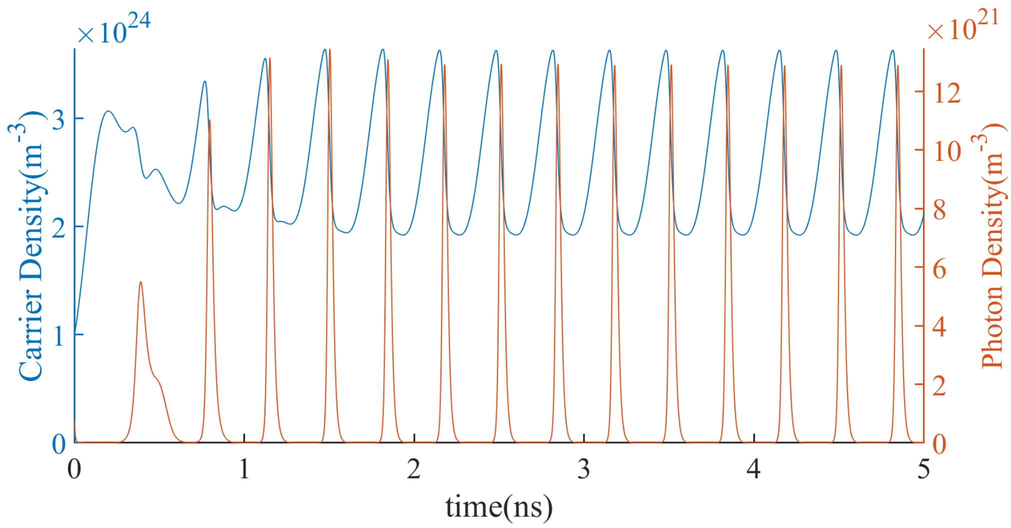

Figure 2.14: Carrier and Photon dynamics in gain switching regime.

laser carriers and photon density results in a train of optical pulses separated by $\frac{1}{f_{rep}}$ in the time domain.

2.4.2 Comb Generation and Frequency Noise

In describing the formation of a frequency comb from a train of optical pulses, as discussed in Section 2.2, the phase relationship between the optical pulses need to be fixed to form an OFC with discrete frequency tones. To comprehensively consider the phase of the optical pulses under gain switched conditions we now consider the stochastic noise terms F_N, F_S and F_ϕ. These noise terms are called Langevin terms, which are white-gaussian noise terms and obey the correlation properties [95]:

$$\langle F_i(t) \rangle = 0 \tag{2.17}$$

$$\langle F_i(t')F_j(t) \rangle = 2D_{ij}\delta(t-t') \tag{2.18}$$

Here i an j are indexes referring to N, S and ϕ. Eqn. 2.17 states that the mean of the gaussian noise term is 0 and Eqn. 2.18 describes the correlation between the carrier, photon and phase noise sources. D_{ij} represents the diffusion coefficients for the noise sources. The known non-vanishing diffusion terms are given by [96]:

$$D_{SS} = \beta\Gamma BN^2S \tag{2.19}$$

$$D_{NS} = -\beta BN^2S \tag{2.20}$$

$$D_{NN} = \frac{\beta BN^2S}{\Gamma} + \frac{1}{V_{act}}(R(N) + \frac{I}{eV_{act}}) \tag{2.21}$$

$$D_{\phi\phi} = \frac{\beta\Gamma BN^2}{4S} \tag{2.22}$$

In order to perform numerical computations with the noise fluctuations F_i, the diffusion terms need to be uncorrelated, i.e orthogonal. The orthogonality of the diffusion terms allows for independant Gaussian noise sources to be generated for each fluctuation term F_i. It can be seen in Eqn. 2.20 there is a cross-correlation between F_N and F_S through the non-vanishing diffusing term, D_{NS}. To generate a new F_i term which is orthogonal with F_S and F_ϕ we introduce a new fluctuation term F_Z [89]:

$$F_Z = \frac{F_S}{\Gamma} + F_N \tag{2.23}$$

The diffusion terms of F_Z are now:

$$D_{ZZ} = \frac{1}{V_{act}}(R(N) + \frac{I}{eV_{act}}) \tag{2.24}$$

$$D_{ZS} = 0 \tag{2.25}$$

$$D_{Z\phi} = 0 \tag{2.26}$$

$$D_{ZN} = \frac{1}{V_{act}}(R(N) + \frac{I}{eV_{act}}) \tag{2.27}$$

Explicit terms for the fluctuations in N, S and ϕ take the form;

$$F(t)_{ii} = \sqrt{2D_{ii}B_{sim}}\xi_i \tag{2.28}$$

where B_{sim} is the simulation bandwidth, i.e the inverse of the simulation time step, and ξ_i is a random Gaussian noise variable with zero mean and unity variance. Now explicit terms for the fluctuations can be written as:

$$F(t)_S = \sqrt{2D_{SS}B_{sim}}\xi_S \tag{2.29}$$

$$F(t)_\phi = \sqrt{2D_{\phi\phi}B_{sim}}\xi_\phi \tag{2.30}$$

$$F(t)_Z = \sqrt{2D_{ZZ}B_{sim}}\xi_Z \tag{2.31}$$

$$F(t)_N = F_Z(t) - \frac{F_S}{\Gamma} \tag{2.32}$$

With explicit expressions for the laser noise fluctuation complete, next, they are added to the rate Eqns. 2.11-2.13, to create a set of stochastic differential equations (SDEs) modelling the laser carriers, photons and phase. To numerically solve these equations it is first noted that they are SDEs in Ito form. Ito SDEs take the general form [97]:

$$\frac{dx_i(t)}{dt} = f_i(x,t) + \sum_j g_{ij}(x,t)\xi_j(t) \tag{2.33}$$

In the Ito formalism $f_i(x,t)$ is called the drift term, $g_{ij}(x,t)$ is the diffusion term and $\xi_j(t)$ is a random Gaussian white noise variable. When the Ito form SDE is compared with the rate equations it can be seen that the noiseless portion of the differential equations represents the drift term and the Gaussian white noise sources F_i represent the diffusion terms of the SDE. To numerically solve the rate equations the Euler–Maruyama method was used [98]. This is the primary algorithm used for solving Ito form SDEs. This algorithm is provided in the SDEtool MATLAB package [99]. Throughout the simulation process the frequency noise in the optical field was simulated using the relationship between instantaneous frequency and phase evolution:

$$\Delta f(t) = \frac{1}{2\pi}\frac{d\phi}{dt} \tag{2.34}$$

$$FN = \frac{1}{T}|\int_0^T \Delta f(t)e^{-i\omega t}dt|^2 \tag{2.35}$$

where $\Delta f(t)$ is the instantaneous frequency, ω is the Fourier angular frequency and FN is the frequency noise. Figure 2.15 shows the simulated frequency noise spectra for the 2 μm laser source for increasing bias currents. At low currents, near the laser threshold, the phase noise induced by the spontaneous emission in the laser is high due to the low power of the main frequency mode. As bias current increases, the main mode of the laser source begins to suppress spontaneous emission in the laser resulting in reduced frequency noise. Along with the reduction in frequency noise, the resonant noise of the lasers, seen by the peak FN values, shifts in alignment with the shifting RO frequencies. Looking at the effect of modulation amplitude and frequency, two key regimes arose.

First, the lasers output was simulated for optical frequencies ranging from 1 GHz to 4 GHz with 30 mA laser bias and 30 mA modulation amplitude. Figure 2.16 shows the simulated comb spectra for these operating conditions. Figure 2.16(a)-(c) show optical spectra where the clear broadening of the laser

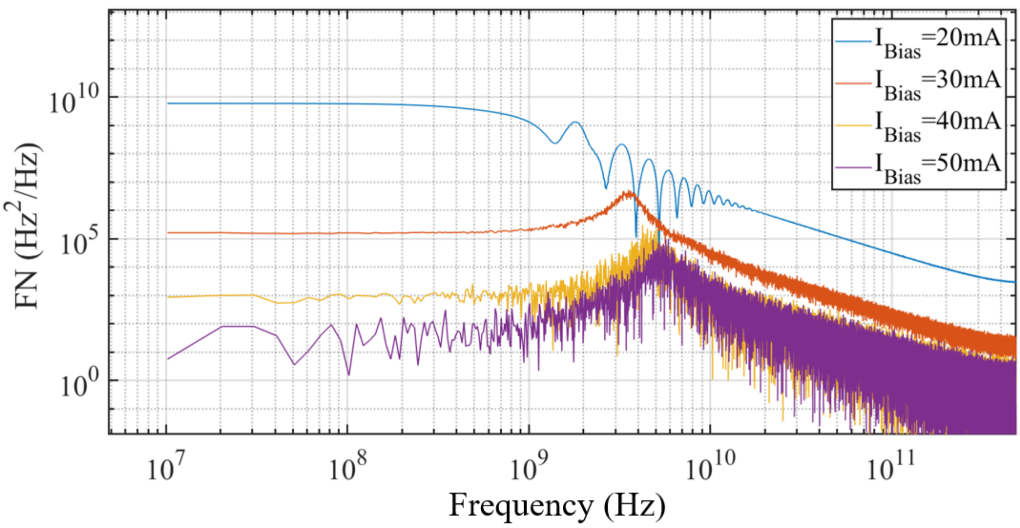

Figure 2.15: Frequency noise spectrum for bias currents from 20 mA to 50 mA.

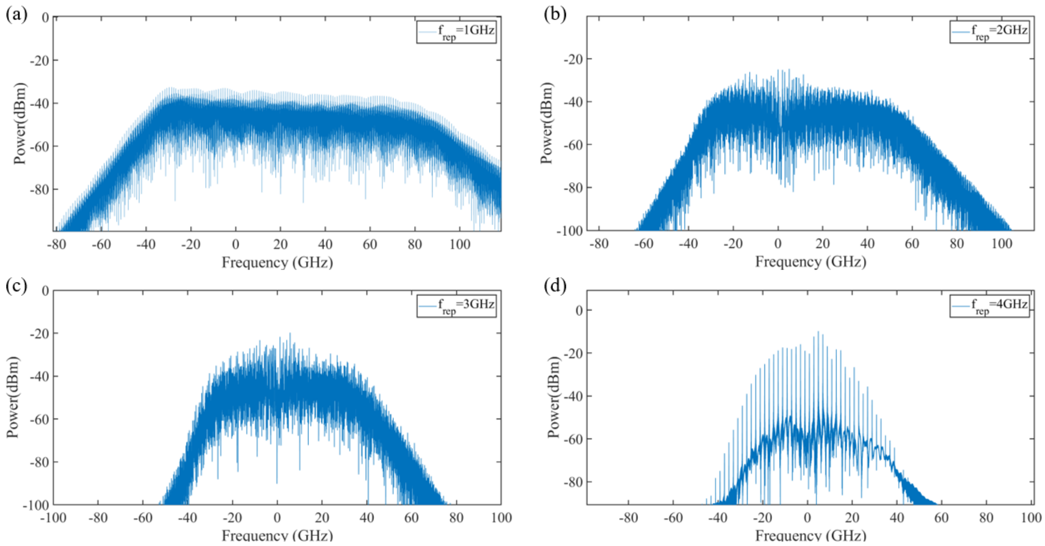

Figure 2.16: Simulation of optical frequency combs generated by gain switched laser biased at 30 mA and modulate with 30 mA amplitude for frequencies ranging from 1 GHz to 4 GHz.

output is seen, however, no comb lines are detected. This continuum generation occurs when the optical phase noise between pulses is large. The phase noise comes from spontaneous emissions which occur below the lasing threshold. With the laser bias at 30 mA and the modulation amplitude at 30 mA, there is a period in the laser modulation where the laser enters a fully off state. Here the photon density in the cavity is very low, with the majority of the emission coming from spontaneous processes with random phases.

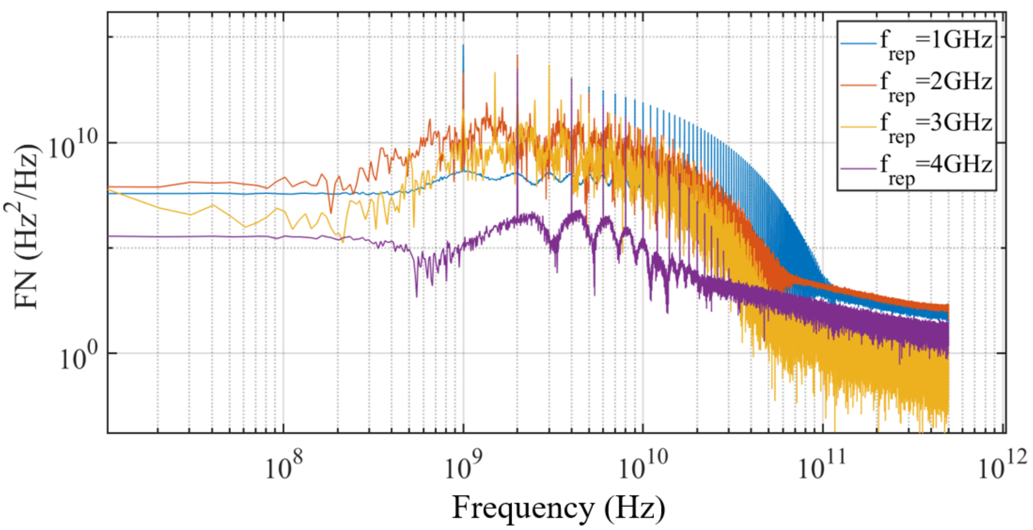

Figure 2.17: Frequency noise spectrum for gain switched laser biased at 30 mA and modulate with 30 mA amplitude for modulation frequencies ranging from 1 GHz to 4 GHz.

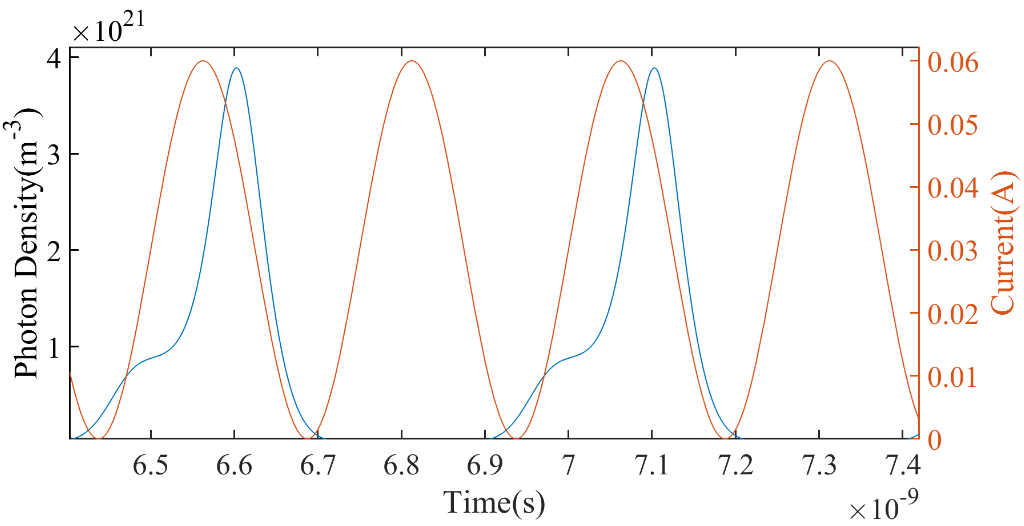

Figure 2.18: Period doubling at 4 GHz modulation frequency.

This caused the consecutive pulses to be seeded by photons with random phase, removing the locked phase evolution required for optical comb formation. Figure 2.17 confirms the large increase in phase noise for modulation frequencies 1 GHz-3 GHz. Note that the additional peaks are formed by the repetition frequency of the modulated laser. Figure 2.16(d) is a special case of comb generation called the period doubled (p2) regime [100]. Figure 2.18 clearly shows the p2 process where the sinusoidal modulation current generates a laser pulse for every second oscillation. Period doubling produces an optical comb as the minimum photon density in the laser cavity is higher when the modulation frequency passes the RO frequency of the laser. For a 3 GHz modulation frequency, a minimum photon density in the cavity was in the order of 1×10^{14}, where minimum photon density was in the order of 1×10^{17} in the 4 GHz case. The increased photon density is due to the 4 GHz modulation signal being greater than the RO frequency of the source, 3.4 GHz. With the modulation frequency greater than the RO frequency, the laser does not have time to fully relax to an off state, preventing the introduction of a large amount of spontaneous emission to the laser pulses. Figure 2.17 confirms the phase stability of this p2 regime with a reduced FN noise compared to the other three cases. The p2 regime present in these sources was not used for OFC generation in this thesis, but could be explored in future works.

To prevent the sub-threshold spontaneous emission from causing large phase noise in the comb sources, we repeated the simulation with a modulation amplitude of 13 mA. This modulation amplitude kept the laser source

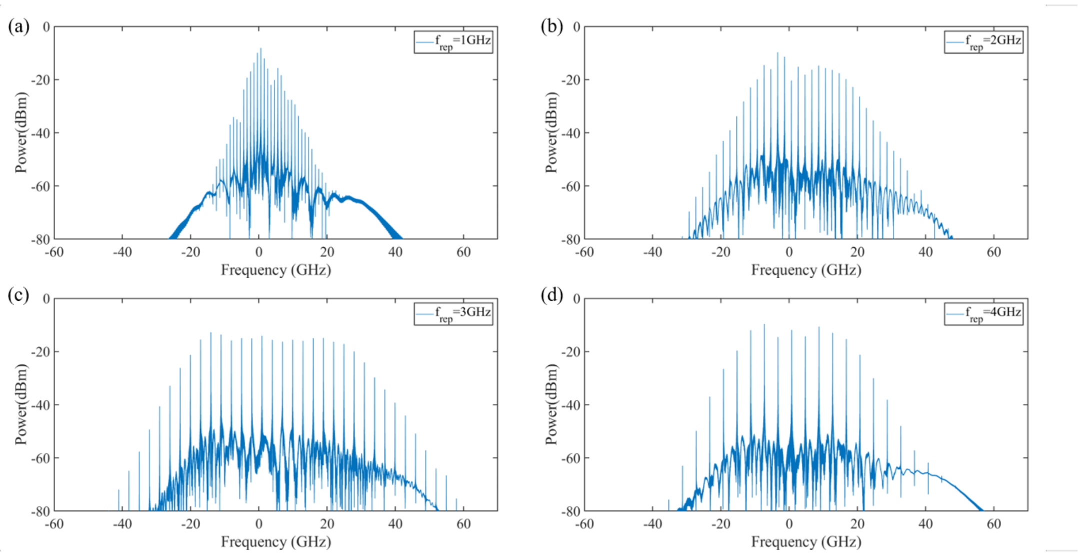

Figure 2.19: Simulation of optical frequency combs generated by gain switched laser biased at 30 mA and modulate with 13 mA amplitude for frequencies ranging from 1 GHz to 4 GHz.

operating just above the laser threshold of 17 mA. Figure 2.19 shows the optical comb when the switching amplitude did not go below the lasing threshold. In all four cases, optical comb generation is seen. Figure 2.20 shows the reduced frequency noise for each case when compared to 2.15. This is further confirmation that modulation current above the laser threshold is essential for maintaining OFC generation with discrete comb lines. Of the four

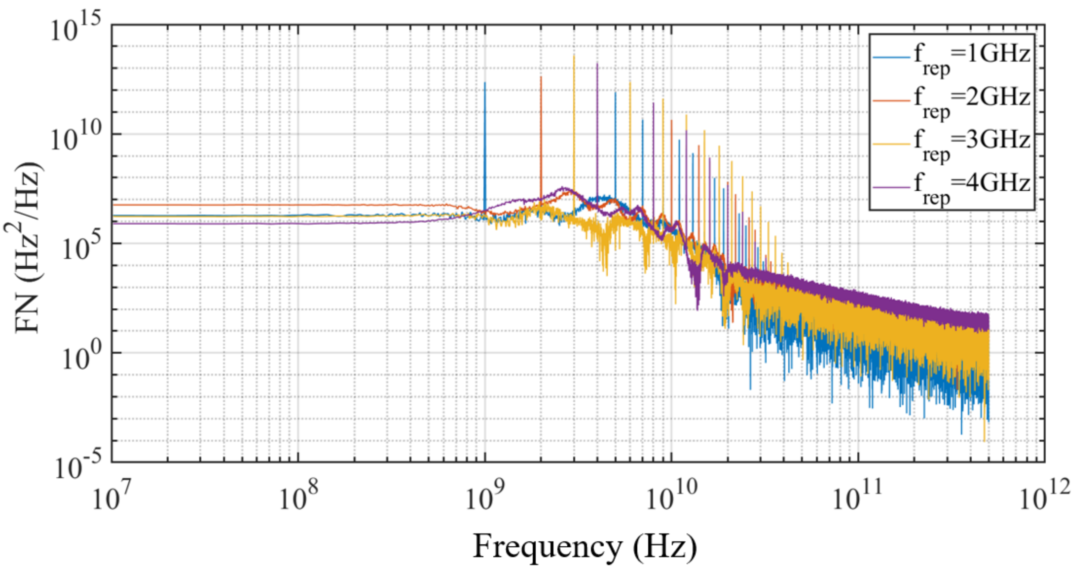

Figure 2.20: Frequency noise spectrum for gain switched laser biased at 30 mA and modulate with 13 mA amplitude for modulation frequencies ranging from 1 GHz to 4 GHz.

comb spectra, the result for the 3 GHz modulation signal shows the best spectral profile, with the largest range of frequency lines in a flat spectral region. The simulation predicted 20 discrete frequency tones above -30 dBm, spanning 60 GHz. For the 1 GHz and 2 GHz cases, asymmetry in the optical pulses resulted in asymmetry in the comb spectra, making them less desirable for many applications. The 4 GHz covered a spectral bandwidth similar to the 3 GHz case but produced fewer comb lines due to the higher repetition rate. This set of simulations was repeated for increasing laser bias currents and the optimal combs for each bias were collected. From this, it was seen that the optimal conditions for frequency comb generation in these laser sources were at frequencies near the RO frequencies and modulation amplitudes just above the laser threshold current.

2.5 Summary

In this chapter, the fundamentals of semiconductor materials lasers were discussed. The design of the 2 μm InGaAs MQW DM laser sources used throughout this thesis was shown. The principle of optical frequency comb formation was demonstrated and the relationship between pulse properties and their resultant OFCs were derived. A summary of the current state of the art for OFC generation at 2 μm showed the gap in this waveband for low power, robust and integrable comb sources. Through numerical simulation of the gain switching modulation regime in recently developed InGaAs MQW DM laser sources, the potential for these semiconductor lasers to be operated at simple comb sources in the 2 μm waveband was shown. Simulations showed optimal modulation conditions were achieved around the RO frequency and when the modulation amplitude remained above the lasing threshold current. In theory, these lasers could have many uses in the domain of 2 μm optical sensing. In the next chapter, we look to show experimental procedures and results for OFC generation using the devices simulated in this chapter.

Chapter 3

Gain Switching of InGaAs MQW Discrete Mode Laser at 2 μm

In Chapter 2, the potential for OFC generation at 2 μm using gain switched InGaAs MQW DM lasers was simulated. It was found that laser bias current, modulation frequency and modulation amplitude were the key parameters dictating the properties of the generated OFCs. In this chapter, OFC generation using InGaAs MQW DM laser diodes at 2 μm is experimentally tested. The effects of laser bias current, modulation frequency and modulation amplitude were studied to maximise comb bandwidth and stability. Section 3.1 covers the experimental measurement techniques used to acquire the information from the optical comb signal. In many situations, novel measurements were required to avoid the limitations of detection equipment in the 2 μm waveband. Section 3.2 describes the results obtained from experiments involving the gain switching of a single laser source; generating an optical comb at 2.002 μm. Section 3.3 describes the process of optical injection locking and its inclusion in the comb generation process as a method of expanding OFC bandwidth and stability.

3.1 Measurement Techniques

Generating and analysing OFCs around 2 μm comes with some additional challenges due to the lack of availability of high-resolution optical spectrum analysers (OSAs) at this wavelength. With detection resolutions (6 GHz) below the frequency comb spacing used in this thesis (0.5 - 4 GHz), OFC presents as broad optical continua. This removes the potential to measure free spectral range (FSR), noise suppression around the comb lines and pulse to pulse coherence. In this thesis, much of the OFC analysis is carried out in the electrical domain using an electrical spectrum analyser (ESA) and an InGaAs photodiode operating at 2 μm. Through analysis of the beating tones generated between the optical comb and an external laser source, many of the comb characteristics can be recovered. The details of this method of comb analysis are explored in this section.

3.1.1 Comb Detection in Electrical Domain

Information about an optical frequency combs repetition frequency, noise, bandwidth and power can be obtained from electrical domain analysis using a photodetector and electrical spectrum analyser. Two of the key methods used are direct detection and heterodyne beat tone detection. First, we need to look at the RF spectrum generated by the direct detection of an OFC. Figure 3.1 shows the RF spectrum generated by an OFC incident on a photodetector. The spectrum generated shows harmonics of the pulse repetition frequency f_{rep}.

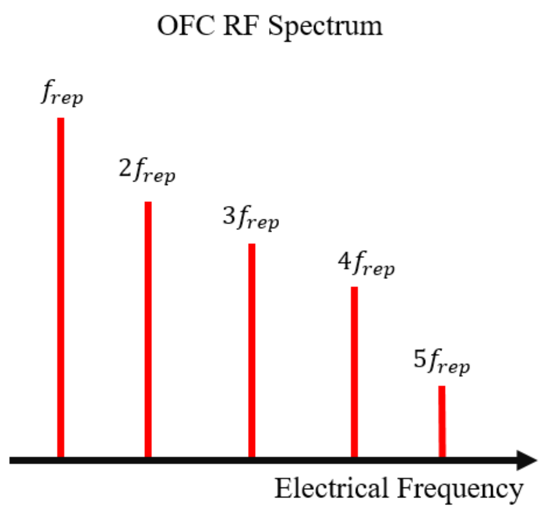

Figure 3.1: RF spectrum generated through direct detection of an OFC with repetition frequency f_{rep}.

Although direct detection on the RF intensity power spectrum can show the frequency spacing generated in an OFC, it gives limited information on the coherence OFC detected. It has been shown that this method retrieves information about the periodic characteristics of the field landing on the photodetector and some information on the pulse jitter through the comparison of noise floor levels [87]. In Chapter 2, it was shown through simulations that there are gain switching regimes where periodic pulse signals produced by the laser source will not form an optical comb due to increased pulse-to-pulse phase noise. In the case where high phase or amplitude noise is present in the signal, the ESA will display pulse repetition frequency harmonics, as expected, but further analysis using a high-resolution OSA would show a broad optical spectrum with no discrete tones, i.e. a continuum. As mentioned, there is currently no OSA operating at 2 μm with sufficient resolution to carry out this analysis. With this limitation, additional measurements are needed to confirm the presence of an optical frequency comb at this wavelength. In this thesis we used a heterodyne beat tone detection method to differentiate between gain switching regimes generating OFCs and continua.

Heterodyne detection is a method used to extract frequency, phase and amplitude information from an optical signal by generating beating tones between it and another optical signal with known properties. The signal with known properties is called a local oscillator and is typically a continuous wave (CW) laser source. An optical beating tone is generated when an optical field containing more than one frequency component is superimposed on a square-law photodetector [101]. For this portion of the thesis we focus on the simplest case, where all optical signals are coherent with the same phase. This allows us to focus on the intensity portion of the heterodyne beating tones generated and how that can be used to differentiate coherent and incoherent gain-switched pulse generation regimes. The electric field produced by two optical signals of different frequencies can be described by:

$$E = E_1 cos(\omega_1 t) + E_2 cos(\omega_2 t) \tag{3.1}$$

where E is the combined electric field, E_1 and E_2 are the amplitudes of the individual electric fields and ω_1 and ω_2 are the frequencies of each signal. When the combined electric field is incident on a square law detector, the intensity of signal produced by the detector is proportional to the square of the incident electric field:

$$E^2 = [E_1 cos(\omega_1 t) + E_2 cos(\omega_2 t)]^2 \tag{3.2}$$

$$E^2 = E_1^2 cos^2(\omega_1 t) + E_2^2 cos^2(\omega_2 t) + E_1 E_2 cos(\omega_1 t) cos(\omega_2 t) \tag{3.3}$$

Through substitution of trigonometric identities for $cos^2(x)$, and the assumption that ω_1 and ω_2 are outside the detection range of the photodetector used, the ω_1, ω_2 and $\omega_1+\omega_2$ terms can be ignored. With this in mind, Eqn. 3.3 simplifies down to:

$$E^2 = \frac{1}{2}E_1^2 + \frac{1}{2}E_2^2 + E_1 E_2 cos((\omega_1 - \omega_2)t) \tag{3.4}$$

Eqn. 3.4 can be represented in terms of intensity of the signal produced at the photodetector through:

$$I = I_1 + I_2 + 2\sqrt{I_1 I_2} cos(\theta) cos((\omega_1 - \omega_2)t) \tag{3.5}$$

where θ is the angle of polarisation between the electric fields and is at a maximum when the fields are parallel. The DC portion of the equation is represented by $I_1 + I_2$ and the RF portion, i.e. the beating tone, is represented by $2\sqrt{I_1 I_2} cos(\theta) cos((\omega_1 - \omega_2)t)$. This is the simplest case of two lasers of different frequencies and the same phase landing on a photodetector surface. In this case, a single beating frequency would be observed on an ESA, which is connected to the photodiode. The frequency of this beating tone would be equal to the frequency difference between the two lasers and the amplitude is a combination of the individual amplitudes of each signal.

To analyse the coherence of a pulse train, i.e. the formation of an OFC or continuum, heterodyne beat tone detection can be used. For this test the pulse train is the signal being analysed and a continuous wave laser, that we call a probe laser, is used as a local oscillator. The probe laser frequency is set between two frequency tones of the suspected OFC, as per Fig. 3.2(a). The frequency of the probe laser is selected to be near one of the OFC frequency tones, making sure it is not exactly in the middle of two comb tones. This means that the OFC lines all share a different frequency spacing with the probe laser, allowing for the generation of beating tones that are individual to each comb line. The individuality of beating tones is required, as beating tones

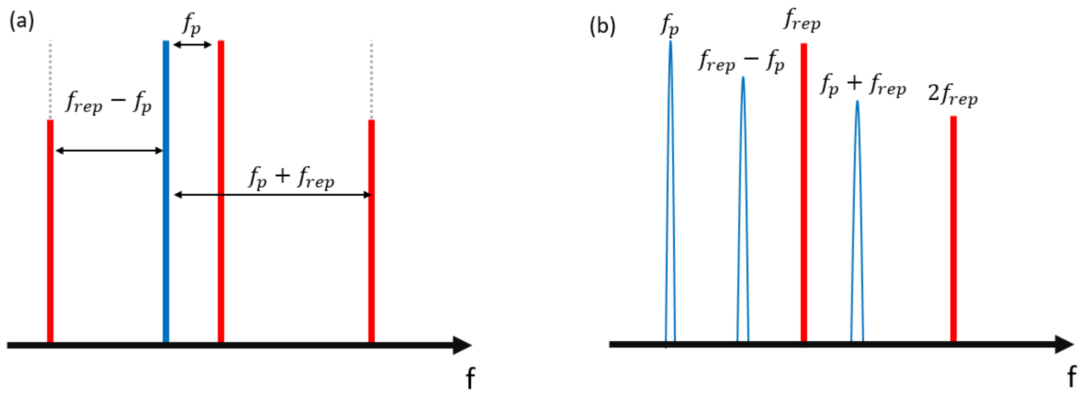

Figure 3.2: (a) Heterodyne measurement showing an OFC (red) beating with a local oscillator called the probe laser (blue) (b) Beating signals between the probe laser and frequency tones of the OFC.

generated by more than one comb line interaction with the probe laser contain a mix of the amplitude and phase information of each of the comb lines. Figure 3.2(b) shows the electrical spectrum generated by Fig. 3.2(a), with both heterodyne beating tones (blue) and direct detection frequencies (red). To confirm the coherence of a train of optical pulses, the amplitude of the beating tone generated between the local oscillator and OFC can be monitored. Simply, in the case where no beating tone is generated, it can be said there are no discrete comb frequencies present for the local oscillator to beat with. This measurement allows for the identification of coherent and incoherent gain-switched pulse generation regimes, without the need for a high-resolution OSA.

3.2 Gain Switched Comb Characterisation

This section covers the experimental generation of OFCs in the 2 μm wavelength region using gain switching of semiconductor laser sources. The lasers used were InGaAs MQW DM lasers, as described in Section 2.1.3. The effects of different switching conditions were studied to achieve an optimal OFC with large bandwidth and low noise characteristics. The key parameters studied included laser bias current, modulation current amplitude and modulation current frequency. The potential switching frequencies of the MQW laser are studied through the frequency response measurements, and the coherence properties of the optical comb are studied through heterodyne detection methods.

3.2.1 Gain Switching Experimental Setup

Figure 3.3 shows the experimental setup used for the generation and detection of a gain switched OFC in the 2μm wavelength region. Figure 3.3(a) shows the portion of the setup used for OFC generation. The OFC was generated by gain switching an InGaAs MQW DM laser source, as shown in Section 2.1.3. The laser was biased above threshold and the modulation current was supplied by an SMR20 Rohde & Schwarz RF Generator. The RF modulation current was also passed through a 20 dB RF amplifier. Figure 3.3(b) shows the probe laser, which was used to generate heterodyne beating tones with the comb source laser, returning information about the phase and coherence of the OFC. Isolators were used in both sections to reduce optical feedback to the laser sources, particularly from the TDFA spontaneous emissions. Polarisation controllers were used to maintain parallel polarisation between the probe and comb laser, which maximised the amplitude of the beating tones generated. Figure 3.4 shows the LI curves for both the DM and probe laser sources. Both sources had a lasing threshold around 15 mA and maximum output power of approximately 1 mW. Once these two signals are combined through an optical coupler, they were amplified using a Thulium doped fibre amplifier (TDFA). The amplifier generated a large bandwidth amplified spontaneous emission spectrum, with high net optical power [102]. The amplifier used was designed as part of this thesis. The development and design of this amplifier is covered extensively in Chapter 5. To prevent saturation or damage to the detectors, a

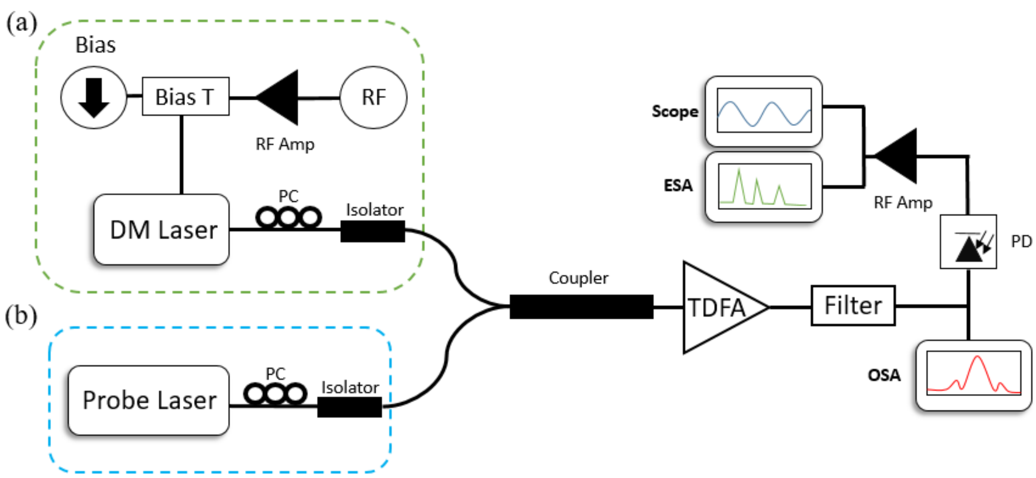

Figure 3.3: Gain switching setup for comb generation and analysis where (a) is the comb generation section and (b) is the probe laser used for heterodyne detection of the comb lines.

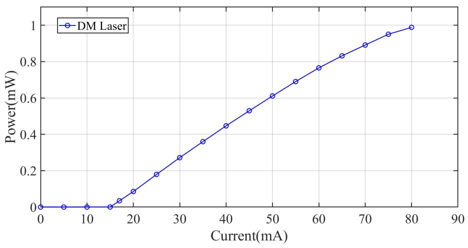

(a)

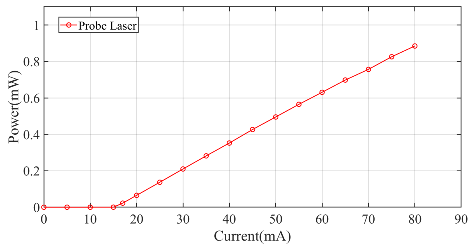

(b)

Figure 3.4: LI curves for the (a) DM Laser and (b) Probe laser.

mechanical filter was used to remove a large portion of the amplified spontaneous emission. This filter allowed for a tuneable 5 nm wavelength window to pass through around 2 μm. The comb was analysed in both the optical and electrical domains. A Yokogawa AQ6375B long-wavelength optical spectrum analyser, with a detection range of 1200 nm to 2400 nm at 6 GHz resolution, was used to detect the optical spectrum of the comb generated. As the comb repetition rates used were below this 6 GHz resolution, the measurement only gave a rough outline of the comb shape and side mode suppression ratio. For a more detailed analysis of the comb, the informationwas converted to the electrical domain using an InGaAs ET-5000 photodetector developed by EOT, which had a 12.5 GHz bandwidth and a 1.3 A/W photoresponse at 2 μm. The electrical signal from the photodetector was amplified and sent to an Agilent E4407b ESA and Keysight 86100D Infiniium DCA-X Wide-Bandwidth Oscilloscope. This allowed the heterodyne beating interaction and shape of the optical pulses generated by the gain switched laser to be monitored.

3.2.2 Comb Source Frequency Response

The simulations of OFC generation through gain switching, presented in Chapter 2, showed the frequency response and relaxation oscillation frequency (RO) are key to understanding the limits and operating range of gain switched laser sources. Figure 3.5 shows the measured frequency response of the MQW laser which was used as a comb source in this experiment. The frequency response is shown for increasing bias current from 20 mA to 50 mA. It was seen that increasing bias current led to an increase in bandwidth and a slight reduction in power at lower frequencies. The increase in RO frequency and bandwidth is due to the increase in photon density in the laser cavity at higher bias currents. The maximum 10 dB bandwidth was measured to be 5 GHz

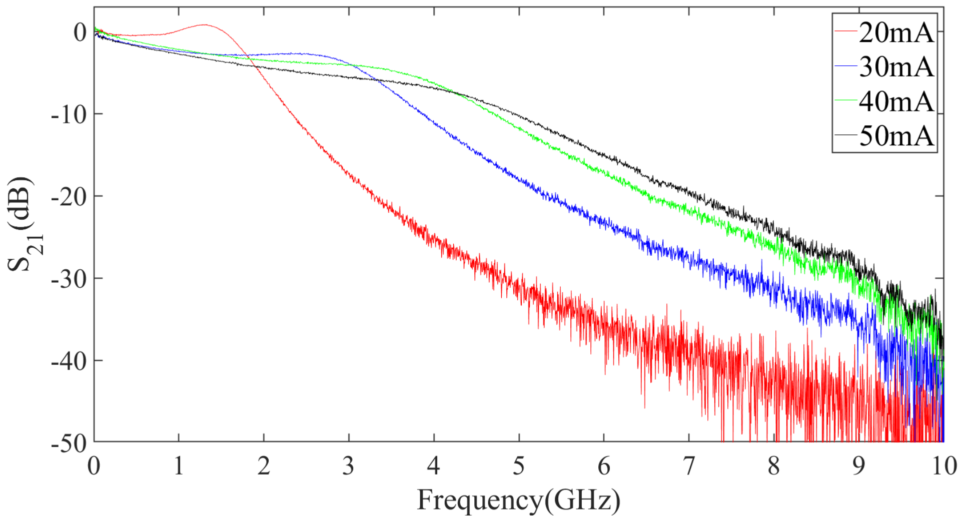

Figure 3.5: Frequency response of MQW laser diode for increasing bias currents.

when biased at 50 mA. This is a relatively small bandwidth when compared with devices operating at other more developed wavelengths, like 1550 nm, but for the application of optical sensing, a lower frequency response is desirable. The benefit of low repetition frequency OFCs, for sensing applications, will be elaborated on in Chapter 4. The relaxation oscillation frequency of the laser source, biased at 20 mA, was detected in the S21 profile through the resonance peak in Fig. 3.5. At 20 mA bias, the relaxation oscillation frequency was detected at approximately 1.4 GHz, as predicted through simulations in Table. 2.1. The resonance peaks for relaxation oscillation frequencies at biases beyond 20 mA were less prominent but assumed to be approximately the values predicted in the simulations.

3.2.3 Modulation Amplitude and Comb Coherence

Using the setup shown in Fig. 3.3, the effects of varying modulation frequency and amplitude on the generation of optical combs were studied. In Chapter 2, it was shown that modulating gain switched lasers near their RO frequency allows for broad coherent frequency combs to be generated, while the sources are not switched below the laser threshold. The broadening of the OFC bandwidth was due to the increased pulse compression with increasing modulation amplitude. This is in agreement with similar experimental predictions [87]. To experimentally test the upper limit of the applied modulation amplitude, and therefore the comb bandwidth, the maximum modulation amplitude which could be applied to the 2μm laser sources, while maintaining coherence between the optical pulses produced, was measured.

Typically, coherence is determined through the carrier noise ratio (CNR) of OFC recorded in the optical domain using an OSA, which is not an option at 2 μm. In this experiment, the coherence of the OFCs was determined through time jitter measurements of the optical pulses on a sampling oscilloscope and analysis of the beating tones generated through the previously described heterodyne detection method. Timing jitter describes the variation in the temporal pulse position. In the case where pulses are seeded by spontaneous emission, the spontaneous onset of the pulses produce an increase in variation of temporal pulse position [103]. Through measuring timing jitter, switching conditions that result in pulses formed from spontaneous emission, can be identified. The root mean square (RMS) timing jitter was measured using the Keysight 86100D Infiniium DCA-X Wide-Bandwidth oscilloscope in combination with the 86107A Precision Timebase trigger module.

Figure 3.6 shows the RMS jitter values and pulse width recorded for optical pulses generated through gain switching of an InGaAs MQW DM laser, operating at 2.002 μm, with increasing switching amplitude. The pulse width was measured using the ET-5000 photodetector, which had a rise time of 28 ps. The fast rise time should be sufficient to accurately measure the laser pulse widths, but an autocorrelator could also be used for maximum accuracy. The

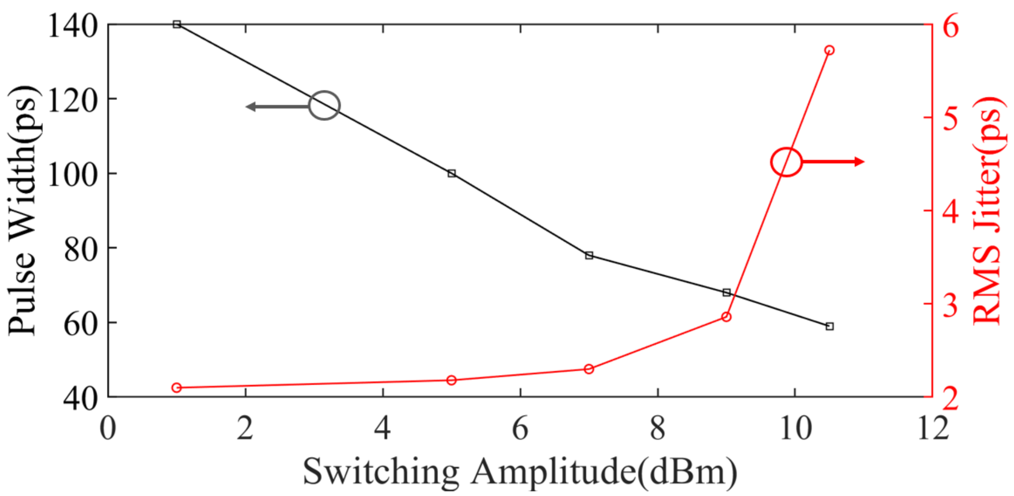

Figure 3.6: Recorded timing jitter and pulse width for InGaAs MQW DM laser modulated at 2 GHz with increasing switching amplitude at 30 mA bias.

laser was biased at 30 mA with a modulation frequency of 2 GHz. This modulation frequency was selected as it was below the RO frequency of the laser. This allows for the demonstration of clear coherence loss in measurements without the potential for above RO coherent effects, such as period-doubling. As the switching amplitude was increased, a near linear reduction in pulse width was measured, but also a clear jump in timing jitter for higher switching amplitudes was observed. From this result, it was inferred that the pulses produced for switching amplitudes beyond 7 dBm were seeded by spontaneous emission and lacked coherence.

To further confirm the loss of pulse-to-pulse coherence, the heterodyne beating spectra between the OFC an probe laser was captured, as shown in Section 3.1.1. This was done for a low jitter and high jitter switching amplitudes. Figure 3.7 shows the heterodyne signal generated between the probe laser and optical comb at these two switching amplitudes. As described in Fig. 3.2(b) in Section 3.1.1, the heterodyne beating tones present as broad peaks and the direct detection of the pulse repetition frequency can be seen at multiples of 2 GHz. The red line shows the signal detected when the modulated laser is switched with 7 dBm and the black signal when switched with 10 dBm. When the switching amplitude is 7 dBm, clear beating tone pairs are generated between the repetition frequency signals. These beating tones represent the beating between the probe laser and discrete comb lines. The beating tones are broad due to uncorrelated phase noise between the comb source and probe laser. In contrast to this, when the comb source is switched at 10 dBm, no

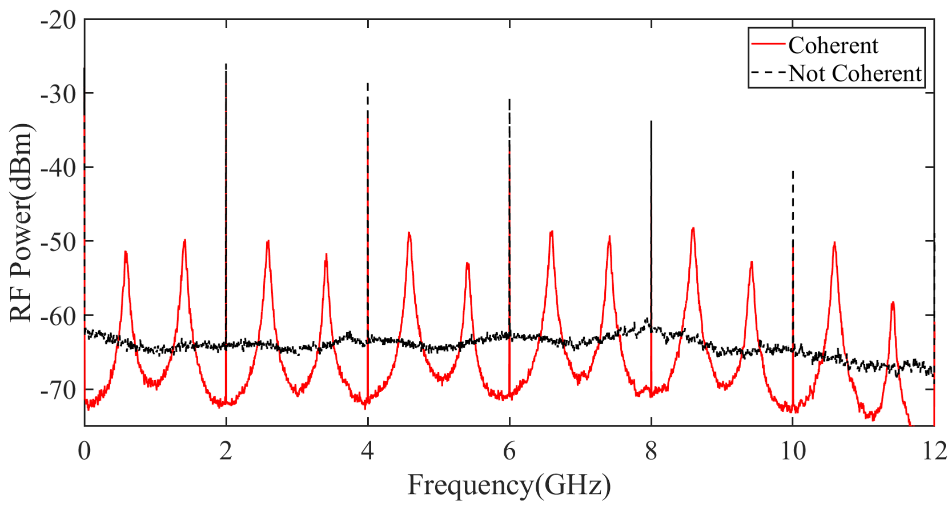

Figure 3.7: Electrical spectrum detected by the heterodyne detection setup where the comb detected is coherent (red) and not coherent (black).

Table 3.1: Optimal GS modulation amplitudes for different modulation frequencies.

Frequency	Switching amp.(dBm)	Phase noise(dBc/Hz)
500 MHz	0	-66
1 GHz	3	-64.7
2 GHz	7	-60
3 GHz	8	-57.5

beating tones are generated and the noise floor displays a 10 dB increase. This shows that there are no discrete tones present for the probe laser to beat against, or the OFC CNR is very low. From this, it can be concluded that the pulse-to-pulse coherence is lost and no comb or a comb with very low CNR is generated. This is in line with the results obtained for the jitter increase with switching amplitude.

These measurements were repeated for modulation frequencies ranging from 500 MHz to 3 GHz to find the ideal switching amplitudes to achieve narrow pulses while maintaining good pulse-to-pulse coherence for each frequency. Table 3.1 shows the optimal switching amplitudes for each modulation frequency and a measured phase noise value in each case. An increase in the maximum switching amplitude is seen with increasing modulation frequency. This is due to the carriers not fully depleting at higher modulation frequencies, allowing for the pulses to be seeded by coherent light in the cavity. This effect is much larger around and beyond the relaxation oscillation frequency of the laser [89, 90]. This can be seen in the much larger switching amplitudes for 2 GHz and 3 GHz modulation. The phase noise was calculated through analysis of the heterodyne beating tone generated. By measuring the RF spectral power density in a 1 Hz bandwidth, 10 MHz from the beat tone peak power, then getting the ratio of that power to the carrier power, the noise in decibel relative to carrier per hertz (dBc/Hz) at 10 MHz can be found [104]. This value contains the combined phase noise of the two laser sources, the comb and the probe laser, which are uncorrelated. As the phase noise value for the probe laser is constant between measurements, the evolution of the noise values indicates an increase in phase noise in the comb source laser as the switching amplitude and frequency increases.

3.2.4 Modulation Frequency and Comb Spectra

With the modulation amplitudes selected for each operating frequency, the spectral profile of each modulation regime was analysed to find the optimal OFC spectrum, i.e. with maximum spectral bandwidth. Figure 3.8 shows the pulse profiles collected from a sampling oscilloscope at the modulation frequencies and amplitudes listed in table 3.1. As the frequency of the modulation was increased the departure of the optical signal shape from the electrical signal became more apparent. Note, the electrical signal was sinusoidal. This changing signal shape is due to the expected nonlinear response of the laser carriers when switched at large amplitudes and frequencies. In the 500 MHz case, almost no compression was seen. The pulse width was approximately 1 ns and the profile was sinusoidal. As the modulation amplitude and frequency were increased the gain switching process started to occur, where the sudden switching on of the laser caused a large rise in optical power which was quickly depleted. In the case where the modulation frequency was 3 GHz, the pulse width was measured to be 73 ps.

Figure 3.9 shows the optical comb profiles produced by each of the pulse shapes shown in Fig. 3.8. As expected, the comb profile becomes more broad as the pulse width is reduced at higher modulation frequencies and amplitudes. This is also in line with the results predicted in Fig. 2.19. The combs produced in the 500 MHz and 1 GHz regimes had narrow bandwidths

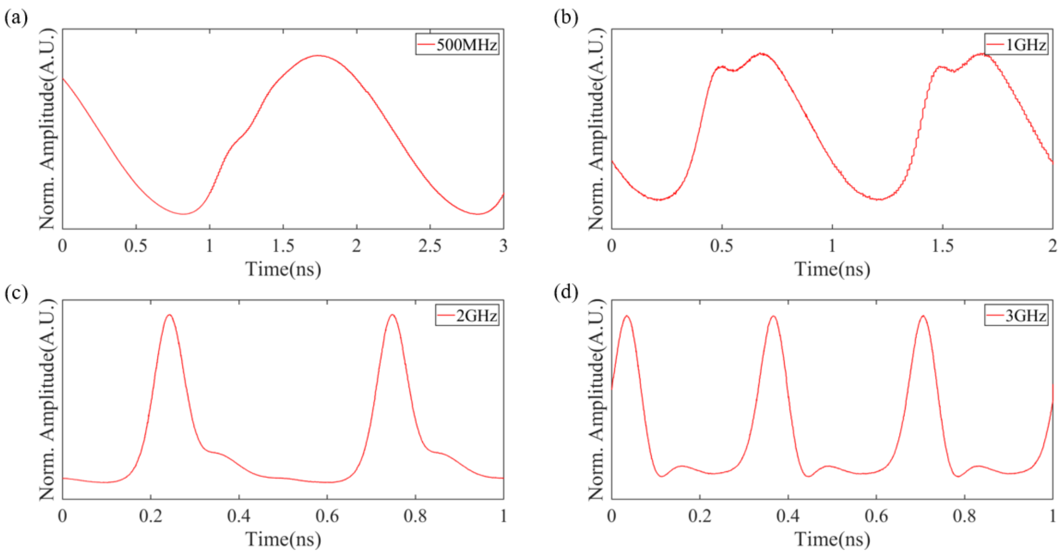

Figure 3.8: Pulse profiles generated from gain switched laser with frequencies ranging from 500 MHz to 3 GHz at their maximum switching amplitudes.

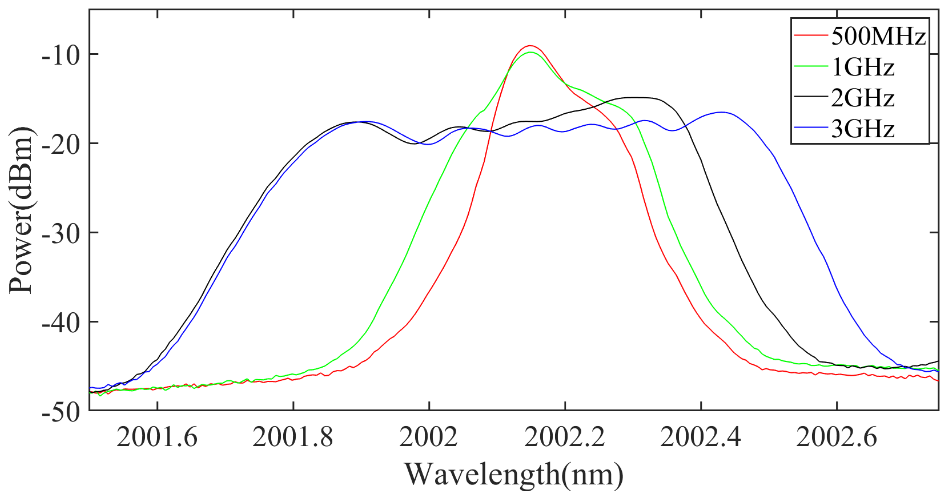

Figure 3.9: Optical comb profiles generated by coherent pulses at frequencies from 500 MHz to 3 GHz.

and lacked a flat spectral region, as they do not have the pulse compression necessary to generate a broad comb. The combs generated at 2 GHz and 3 GHz both displayed broadening due to the narrow nature of the pulses produced in these regimes, 80 ps and 73 ps respectively. The 3 GHz comb produced the most desirable profile, with a 1 nm spectrally flat region centred at 2002.2 nm. Through the optical spectrum, the side mode suppression ratio was measured to be approximately 30 dB. As predicted through simulation in Section 2.4, the switching conditions which produced the best OFC profile, at 30 mA bias, was 3 GHz repetition frequency and modulation amplitude near the laser threshold.

3.2.5 Swept Heterodyne Detection of 3 GHz Frequency Comb

With the comb generation potential of the 2 μm laser sources demonstrated in the previous section, we looked to take the comb with the best general profile and resolve the individual comb lines in the electrical domain. The 3 GHz optical comb was selected as it displayed a broad flat spectrum in the optical domain. To resolve the individual frequency tones present under this comb profile, a swept heterodyne detection method was used. Figure 3.10 describes this detection method. Figure 3.10(a) shows a frequency comb and probe laser in the optical domain. The probe laser is temperature tuned to initially be outside of the comb bandwidth. The temperature is then reduced, tuning the

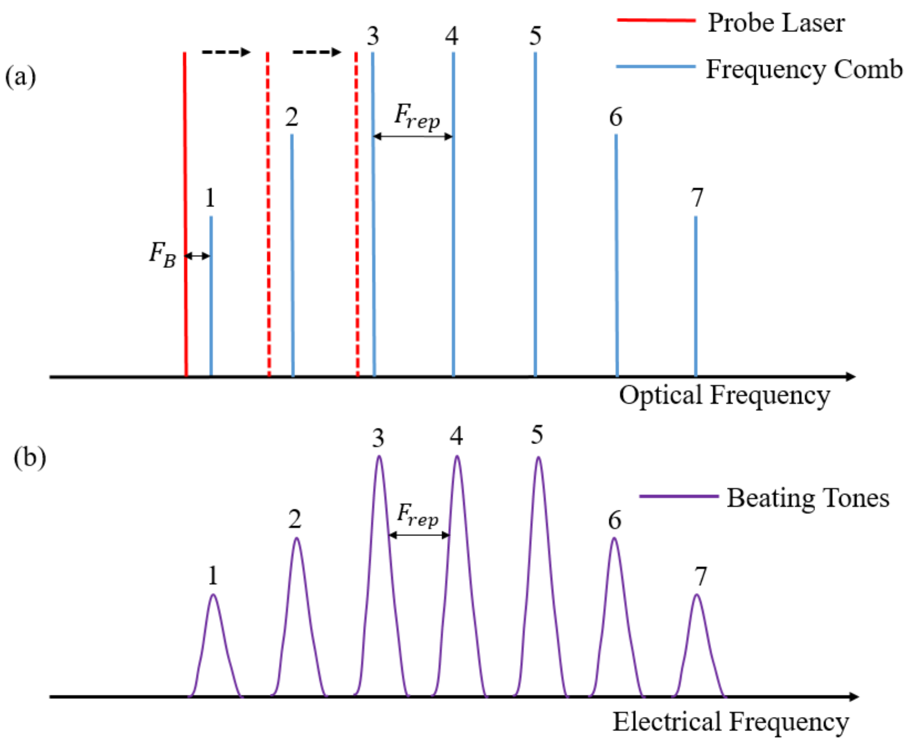

Figure 3.10: Description of the swept heterodyne detection method (a) Frequency comb and probe laser spectra in the optical domain with probe laser being temperature adjusted to sweep across the comb frequency tones; (b) Resulting RF spectrum consisting of beating tones collected from the interaction between the comb and swept probe laser.

frequency until a beating tone is generated with the first frequency of the optical comb. The beat note is recorded and the probe laser is tuned to the next comb line, again generating a beating tone. With this process, the probe laser is swept across the whole comb bandwidth, collecting beat notes between the probe laser and each comb line, as shown by the dashed lines in Fig. 3.10(a). The collected beating tones can then be plotted separated by the modulation frequency, reconstructing the comb in the RF domain, see Fig. 3.10(b).

Fig. 3.11 shows the results obtained for the swept heterodyne measurement when carried out on the 3 GHz comb described in Section 3.2.4. The red dashed line shows the optical spectrum recorded in Fig. 3.9, converted to the frequency domain and centred to overlay with the beating tones recorded. The beating tones were generated between the comb and the swept probe laser, which was operating with -8 dBm peak power and centre wavelength of 2002 μm at 25°C. This power was selected to be maximised while avoiding

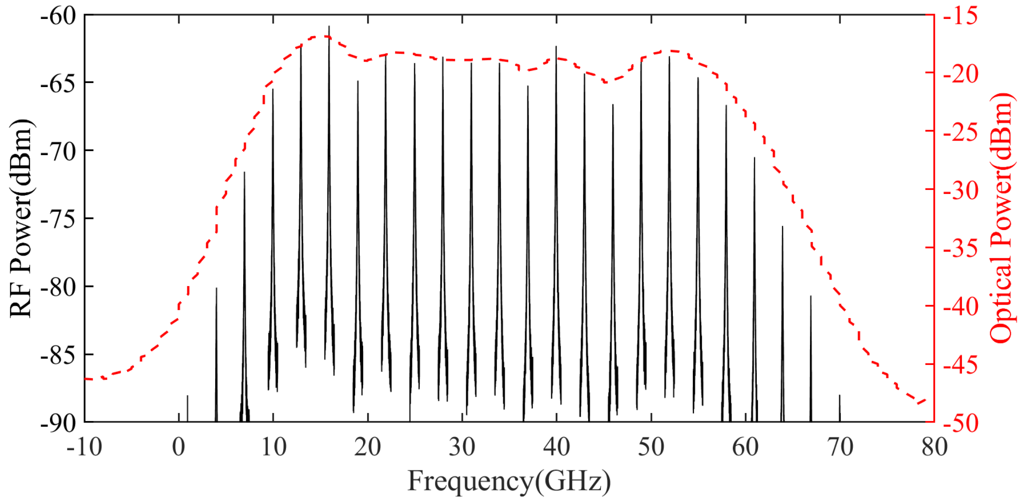

Figure 3.11: Plot of recorded comb spectrum for 3 GHz gain switched frequency comb in the optical and electrical domain.

saturation of the photodetector. The polarisation of the optical comb and probe lasers were tuned to be parallel as the beating tone amplitude is maximised when this is the case. The swept heterodyne measurement showed 19 beating tones within a 10 dB flatness range. The amplitude profile of the beating tones had a very strong correlation with the optical spectrum previously recorded. The beating tones had an average full width half maximum (FWHM) of 5 MHz. This is likely far greater than the linewidth of the individual comb lines as the lack of phase correlation between the probe laser and comb source cause broadening of the beating tone. This demonstration of beating tone detection for a comb at this wavelength was the first step in the realisation of a gain switched compact comb source in the 2 μm wavelength region. Through this RF detection, we showed that these compact lasers could be used in sensing applications where conversion of optical data to the electrical domain is standard [105].

3.3 Gain Switched Comb With Injection Locking

In the previous section we showed the generation of an optical frequency comb at 2 μm using gain switching of semiconductor laser sources. It was shown that the OFC bandwidth was expanded as the modulation current amplitude was increased, due to increased pulse compression. The modulation amplitude, and hence the OFC bandwidth, was found to be limited by spontaneous emission when the laser was switched below the laser threshold current. In the case where pulses were seeded by spontaneous emission no comb was generated, due to the lack of pulse-to-pulse coherence. In this section, we discuss and demonstrate how optical injection locking of the comb source laser can be used to overcome the loss of pulse-to-pulse coherence caused by spontaneous emission seeding. This allows for larger modulation amplitudes to be applied to the comb source, leading to optical combs with increased stability and broadened frequency bandwidths.

3.3.1 Injection Locking

Injection locking is a phenomenon that was first observed in 1665 through the synchronisation of clock pendulums. Dutch physicist Christian Huygens observed that the pendulums of clocks, regardless of their initial phase, would synchronise over time to have the same phase. This was found to be due to vibrations translated between the clocks through a common medium, the surface they were resting on and sound waves travelling through the walls [106]. This mechanism was then demonstrated in the realm of electronics in 1919, where a feedback circuit was used to synchronise two electrical oscillators [107]. In 1966, the first demonstration of the injection locking mechanism in lasers was seen [108]. This mechanism will be referred to as

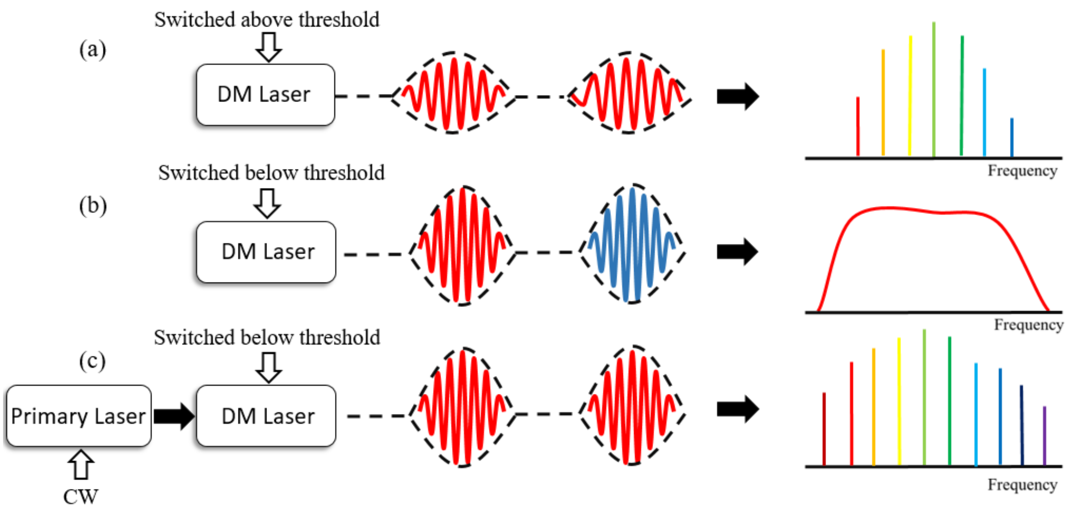

Figure 3.12: Three regimes of gain switching; (a) Laser switching amplitude maintained above laser threshold, preventing pulses from being seeded below threshold (b) Laser switched with larger amplitude, increasing pulse compression of the pulses but coherence is lost due to spontaneous emission below laser threshold seeding the pulses (c) Injection locking used to restore coherence between pulses while maintaining increased pulse compression from the increased switching amplitude, leading to a comb with large bandwidth.

optical injection locking (OIL) through the remainder of this thesis. It was shown that introducing the periodic field of one laser, the primary laser, into the gain medium of another laser, the secondary laser, with similar frequency, would cause the output field from the secondary laser to lock to that of the primary laser. In this scenario the phase and frequency of the secondary laser is said to be locked to the primary laser phase and frequency. It is the process of phase-locking that is of particular interest in gain switched comb generation applications. It has been demonstrated that injection locking of gain switched lasers can improve the bandwidth and reduce noise levels in the combs they produce [109, 110]. This is due to the phase stabilisation of the pulses produced through the gain switching mechanism. We have shown, experimentally and numerically, that coherence between pulses is lost when the laser is switched to an off state where consecutive pulses are generated through spontaneous emission, Fig. 3.12(b). To overcome this, the lasers were not allowed to enter this off state for long enough to cause full depletion of the coherent light in the cavity. This was done by limiting the amplitude of the switching voltage applied to the device, Fig. 3.12(a). By limiting the modulation amplitude the OFC bandwidth was also limited. By using injection locking, with coherent light from an external laser, to seed the optical pulses produced by the gain switched source, the pulse phase becomes locked to the external source. This allows for the gain switched laser to be switched below laser threshold while maintaining the pulse-to-pulse coherence required to produce an optical comb with discrete frequency tones, Fig. 3.12(c).

3.3.2 Characterisation of Optically Injected Gain Switched Comb Source

Figure 3.13 shows the experimental setup used for the generation of an improved frequency comb through gain switching in conjunction with injection locking. A primary laser was injected into the comb source through a circulator designed for the 2 μm wavelength region. A polarisation controller was added to the primary laser to ensure stable injection lucking with the comb source laser [111]. The primary laser used was an InGaAs MQW DM laser, similar to the comb and probe lasers. The output of the injected comb source was launched through a TDFA to amplify the optical signal, then through a filter to remove as much amplified spontaneous emission as possible. The comb was monitored using the same detection setup and heterodyne detection methods

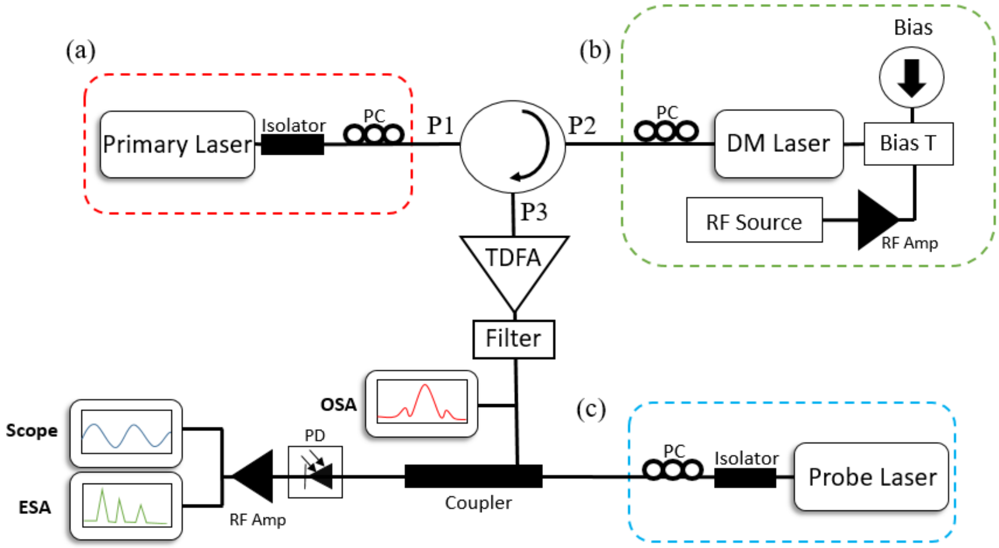

Figure 3.13: Experimental setup for comb generation through gain switching and optical injection; (a) Primary laser used to inject the comb source (b) Gain switched comb generator (c) Probe laser used for heterodyne detection of the optical comb.

as in Section 3.2.5. For this characterisation, we first looked at whether the injection mechanism was able to restore the coherence of the optical comb by analysing the heterodyne beating spectrum. Pulse timing jitter and general profile were recorded on an oscilloscope. Figure 3.14 shows the oscilloscope and heterodyne beating data collected for injected and uninjected gain switched laser. The laser was switched with a modulation amplitude of 17 dBm and a frequency of 3 GHz. For the injected case the primary laser had a centre wavelength of 2002.2 nm and -7 dBm power at the point of entering the comb source laser. For the uninjected case (blue) no beating tones are detected and the pulse trace in the time domain has large amplitude fluctuation and a mean RMS timing jitter of 11.4 ps. These two indicators show that the pulses being produced here lack the coherence required to generate an optical comb with discrete frequency tones. Once the primary laser is introduced, the injection locking process restores coherence to the optical pulses allowing for comb generation to occur in this switching regime. The plots for the injected case (red) show clear beating tone generation and clean optical pulse profile in the time domain, with measured mean RMS jitter of 3.3 ps. A phase noise measurement was again carried out by looking at the phase noise in 1 Hz bandwidth 10 MHz from one of the beating tone peaks. The phase noise was measured to be -69 dBc/Hz, reducing the noise by 11.5 dBc/Hz when compared to the uninjected 3 GHz comb from Table. 3.1.

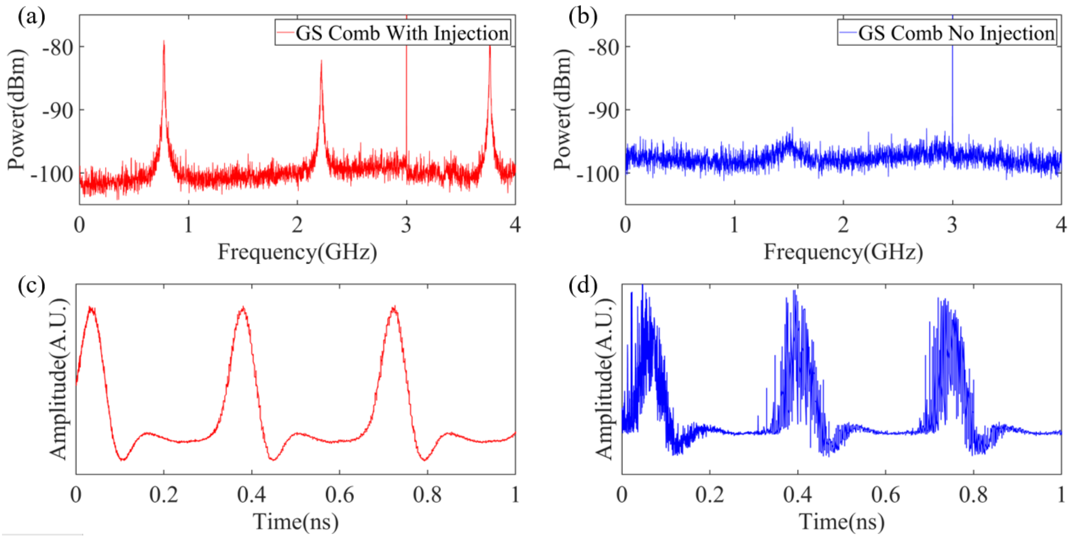

Figure 3.14: Comparison of the injected (red) and uninjected (blue) scenarios for comb generation at 3 GHz with 17 dB switching amplitude; (a)/(b) shows the results for the heterodyne beating tone detection; (c)/(d) shows the time traces recorded from an oscilloscope.

Figure 3.15 compares the pulse profile for the 3 GHz comb, switched at 17 dBm with injection and 8 dBm without injection respectively. The key difference is shown in the increase of peak pulse power and the reduction in pulse width for the injected case. The pulse width was reduced from 73 ps to 60 ps, in line with previous observations that increasing switching amplitude reduced pulse width. Finally, a swept heterodyne characterisation of the injected comb was carried out.

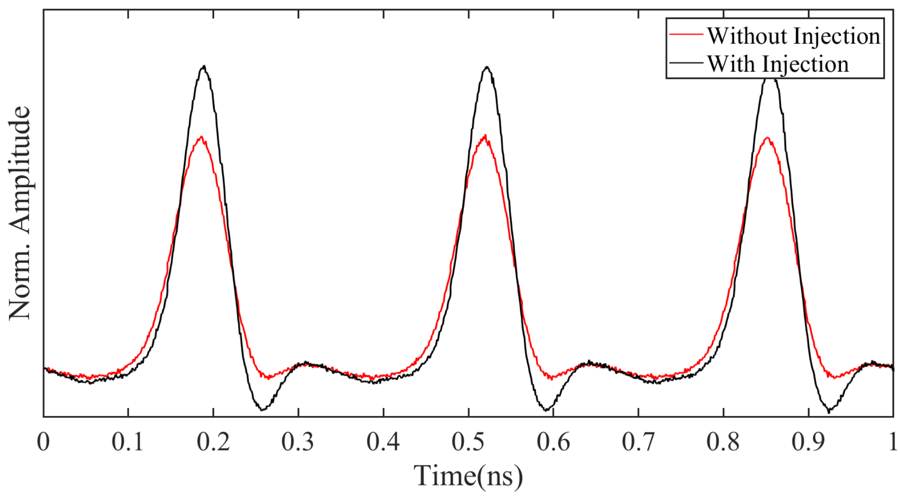

Figure 3.15: Time domain pulse traces for gain switched laser modulated with 17 dB (black) and 8 dB (red) switching amplitudes.

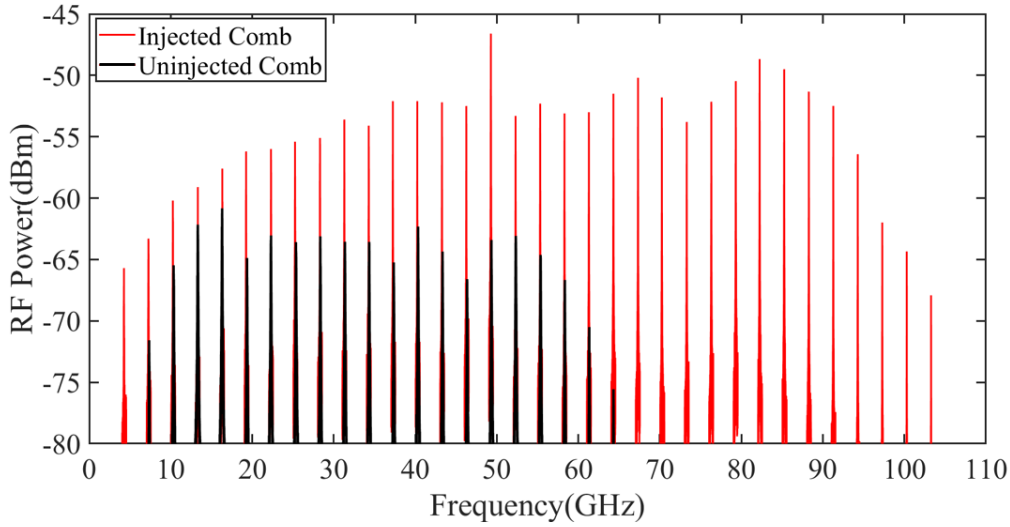

Figure 3.16: Gain switching setup for comb generation and analysis where (a) is the comb generation section and (b) is the probe laser used for heterodyne detection of the comb lines.

Figure 3.16 shows the data collected from the swept heterodyne detection of the injected comb, compared with the detection of the injected comb, compared with the results previously obtained for the uninjected comb. The increased pulse compression, from the higher achievable modulation amplitude in the injected comb, led to a large expansion in comb bandwidth. The injected frequency comb spanned 103 GHz, with 29 beating tones in a 10 dB flatness range. This was an improvement on the 19 tones over 70 GHz from the uninjected source. The outlier at 50 GHz is the beating tone generated between the probe and the primary laser signal.

3.4 Summary

In this chapter, gain switched frequency combs were demonstrated experimentally in the 2 μm wavelength region using InGaAs MQW DM lasers. These combs were characterised through a swept heterodyne detection method, overcoming the low resolution of devices used for optical domain analysis at this wavelength. An optical comb with 19 tones with 10 dB flatness, in the RF domain, was demonstrated using a simple architecture consisting of a laser source and RF current source. With injection locking to one of the comb teeth, the performance of the comb source was vastly improved by restoring the pulse to pulse coherence in high amplitude switching regimes. The number of tones generated in the injected regime was 29 with 10 dB flatness in the RF domain. This comb was centred at 2002 nm spanning 103 GHz. The combs demonstrated in this chapter could be a key enabling technology for optical sensing in the 2 μm wavelength region. However, the requirement of using the swept heterodyne technique to characterise the quality of individual comb lines is not ideal. The swept heterodyne measurement is useful for characterisation but can be time consuming. In the next chapter, we explore methods to implement the 2 μm OFCs in sensing applications, while removing the requirement for the swept heterodyne technique and vastly reducing the time required to characterise individual comb lines.

Chapter 4

Dual Frequency Comb at 2 μm

In Chapter 3 we introduced the first OFC using gain switched lasers in the 2 μm wavelength region. However, there are still challenges associated with these GS-OFCs, in particular, the time consuming swept heterodyne detection method. In this chapter, the 2μm gain switched frequency combs are implemented in a dual frequency comb (DFC) setup, allowing for a large reduction in acquisition time of the comb data, and reduced requirements for broad electrical detection bandwidth. Section 4.1 discusses spectroscopy methods, focusing on how DFCs can offer vast improvements when compared to prominent modern spectroscopy setups. The advantages and disadvantages of broad source, laser and OFC spectroscopy methods are also explored in this section. Section 4.2 covers the experimental setup and describes the effect of uncorrelated phase noise in dual comb setups and how mutual injection locking was used to overcome this issue. The effect of OFC mirroring and beat tone mixing above the Nyquist frequency is explored, explaining the effect of injection symmetry in DFCs and how it can be detected. Section 4.3 shows the experimental results obtained for the first gain switched dual frequency comb in the 2 μm wavelength region, including analysis of the comb bandwidth, stability and acquisition time.

4.1 Spectroscopy Methods

As mentioned in the introduction, spectroscopy is one of the key applications that 2 μm laser technologies could benefit. There are numerous methods to carry out spectroscopic measurements, using a variety of optical sources. In this section we cover some of these methods and why OFCs, as developed in Chapter 3, hold particular utility in spectroscopy applications. Spectroscopy is the study of the absorption, emission, scattering and reflection interactions between light of specific wavelengths and materials [112, 113]. Through looking at these interactions, information about the material can be obtained, from simple identification to information on the molecular structure. Spectroscopy is a vast field with numerous methodologies, beyond the scope of a single thesis. Typically, spectroscopic applications are broken down into the type of photon/material interaction used to interrogate the sample and the type of light used. In this thesis, we focus on absorption spectroscopy and how a variety of optical sources are used to carry out this procedure [114]. As different molecules have different electron and vibrational energy states, they each have a unique absorption spectrum dictated by the allowable energy transitions. This unique absorption spectrum is often referred to as a molecule's absorption fingerprint [115]. Absorption spectroscopy uses this uniqueness of absorption spectra to identify molecules through monitoring wavelengths absorbed from an optical spectrum that interacts with the molecules under test. Figure 4.1 demonstrates the principle of absorption spectroscopy, where the broad spectrum from an optical source is passed through a sample chamber containing an unknown molecule. When the spectrum is detected again after exiting the chamber, the absorption lines of the unknown molecule can be seen. These unique absorption lines allow for the identification of the molecule. The diagram, Fig. 4.1, shows an example of absorption spectroscopy where a broad continuum is used as the probing optical source, however, relying on a spectrum analyser to observe the

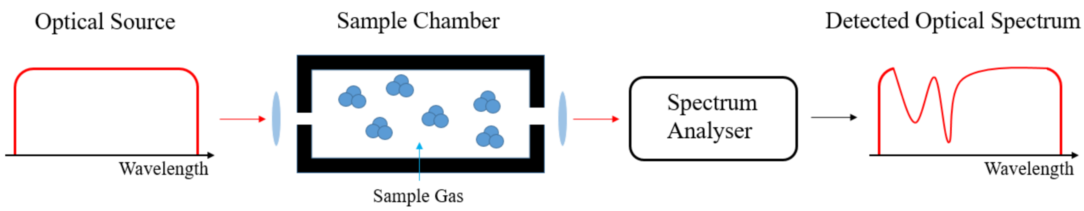

Figure 4.1: General setup used for absorption spectroscopy where a sample gas is interrogated with a broad optical source.

absorption is not practical due to the potential resolution limits of the device and the long acquisition time. The majority of optical spectroscopic techniques involve some form of down conversion of the detected frequencies to allow for detection in the electrical domain with the aid of a photodetector. In practice, numerous types of optical sources are used for this purpose, each with their own advantages and disadvantages. Some of the more popular forms of absorption spectroscopy use swept single frequency lasers, optical frequency comb (OFC) and dual frequency comb (DFC) architectures. In this section we will discuss the basic principles of single frequency, OFC and DFC based spectroscopic measurement setups.

4.1.1 Laser Spectroscopy

Laser spectroscopy, based on single frequency lasers, has been the most commercially successful form of laser spectroscopy [116]. This is due to the low complexity of the setup required to carry out measurements and the relatively low cost of narrow linewidth semiconductor laser sources. For absorption spectroscopy, one could use a single source laser to directly target a single energy transition of a specific molecule, but this removes much of the identification power of broad spectrum analysis. As a substitute for detecting absorption at many wavelengths simultaneously, swept laser sources are typically used. These sources are wavelength tunable narrow linewidth laser with a known wavelength change over a swept time period. Figure 4.2 shows a generic experimental setup for a swept single source laser-based spectrometer. Here a single source laser is swept through a range of wavelengths over time, recording the optical power after passing through the sample using a photodetector. Given that the wavelength at each time step of detecting the power was known, the absorption spectrum across the swept

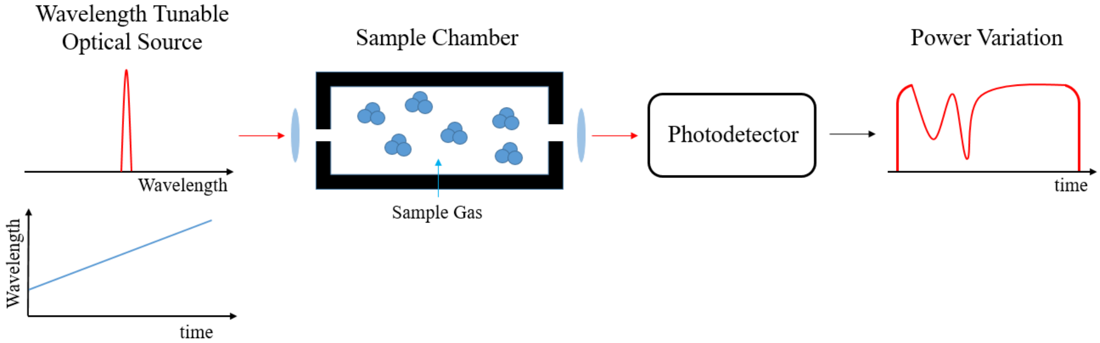

Figure 4.2: Absorption spectroscopy using a single-mode swept laser source.

wavelength range can be found. Swept single frequency laser spectroscopy is resolution limited by the linewidth of the laser source. Assuming a narrow linewidth tunable laser is available at the desired sensing wavelength, the resolution is then set by the increment of the time step when sweeping the laser source. For high-resolution spectra, the acquisition times for these setups are typically of the order of minutes [117, 118]. These setups are also limited by the availability of tunable optical sources at the desired sensing wavelength. To the best of our knowledge, there is no narrow linewidth tunable laser source currently available in the 2 μm region.

4.1.2 Frequency Comb Spectroscopy

Michelson baser Fourier transform spectroscopy has been one of the most successful spectroscopy measurement techniques over the last 50 years [65, 119]. Applications like Fourier-transform infrared spectroscopy (FTIR) have become a staple for sample analysis in laboratory and industrial applications with many spectrometers using this technique commercially available [120]. Figure 4.3 shows an experimental setup of a Fourier transform spectrometer, with an OFC as the optical source. First, consider a single wavelength source. The light from the source is split by a beam splitter where it is sent on two different optical paths. One of these paths has a fixed mirror with set path length P1; the other has a movable mirror with variable path length P2. Considering the interference between the two paths at the source wavelength once they return to the beam splitter, constructive and destructive interference occur depending on the path length difference between the two. Maximum interference occurs when the path difference is one quarter of the source wavelength, resulting in a half wavelength difference on the round trip. By moving the mirror over some distance, where destructive and constructive interference happens many times, an oscillating power can be detected on a photodetector. This detected spectrum is called an interferogram. Through calculating the fast Fourier transform (FFT) of the interferogram, an optical spectrum can be reconstructed. By passing the light through a sample before detection, the power change in the interferogram, and the resulting FFT spectrum, represents the absorption of the sample. This method of down converting optical frequencies to frequencies that can be detected by a photodetector, and then reconstructed through FFTs, has been expanded to use OFCs at the optical source. By using an OFC, many frequency lines in the sample can be probed simultaneously, allowing for better

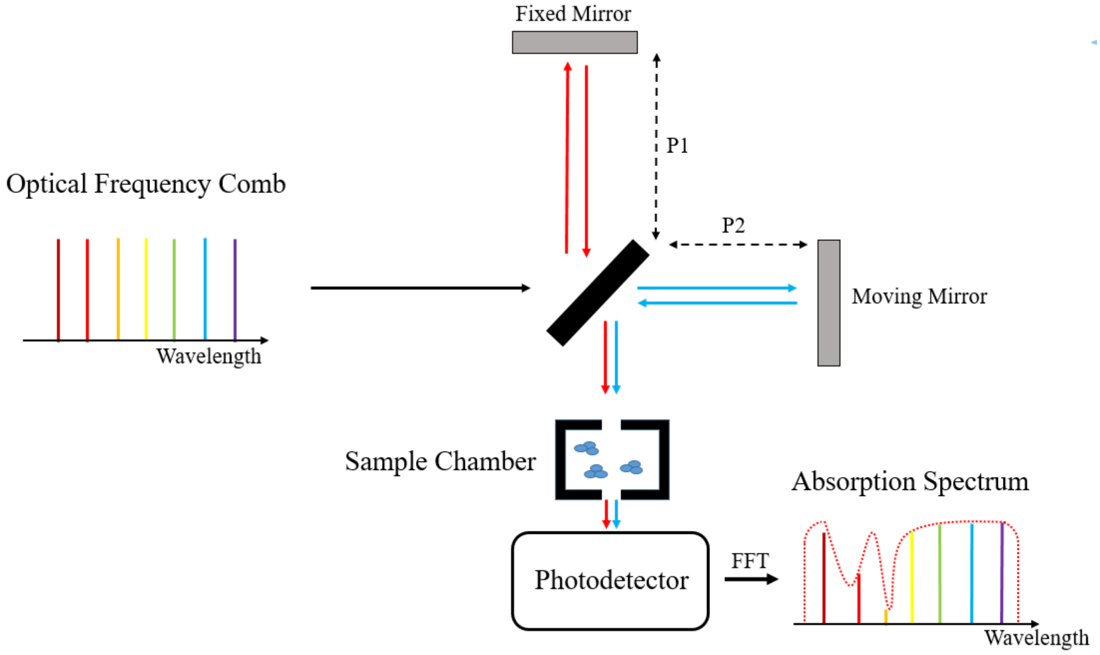

Figure 4.3: Michelson interferometer based OFC Fourier transform spectrometer.

identification of molecules and more complex mixtures. Note that broadband sources are also used in the setup above to simultaneously detect numerous absorption features, however, the comb based approach offers better resolution and reduced detection times due to increased SNR values in OFC based FTIR [121]. The limitations with interferometer based spectroscopic setups are their dependence on moving parts. The requirement of moving mirrors results in bulky equipment which can have slow acquisition times.

4.1.3 Dual Frequency Comb Spectroscopy

Dual frequency combs (DFCs) attempt to solve the issues of moving parts in interferometric spectrometers while maintaining the simultaneous probing of many molecular transitions [122, 43]. In a dual frequency comb setup, the down conversion of optical frequencies to frequencies detectable by a photodetector is achieved through heterodyne beating tones generated between two combs. This technique is similar to the heterodyne interaction we discussed in Chapter 3. Figure 4.4 shows the principle of frequency down conversion using two frequency combs. Two OFCs are generated with slightly different repetition frequencies f_1 and f_2, where $f_2 = f_1 + \Delta f$, where Δf is typically in the Hz-kHz range. When these two combs are combined and

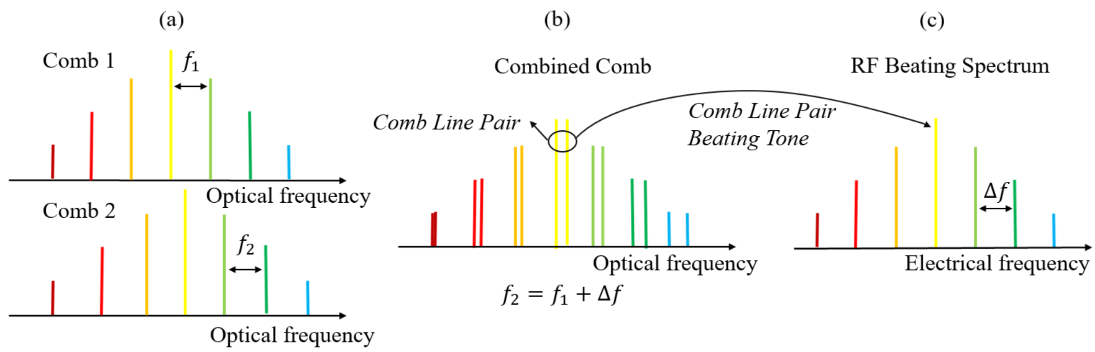

Figure 4.4: Principle of frequency down conversion in dual frequency combs where (a) are two combs with slightly different repetition rates; (b) is the combined combs detected on a photodetector and (c) is the resulting RF beating spectrum containing a down converter image of the original frequency comb.

detected on a photodetector, beating tones are generated between each comb line pair at multiples of Δf. Considering a frequency comb with bandwidth V_{opt}, in the optical domain, the RF beating tone spectrum can be produced with an electrical bandwidth of V_{elec}:

$$V_{elec} = \frac{V_{opt}}{C} \tag{4.1}$$

$$C = \frac{f_1}{\Delta f} \tag{4.2}$$

C is called the compression factor, describing the compression of the frequency comb in the optical domain to the electrical domain. The upper limit on the value of the compression factor is given by:

$$V_{opt} \leq \frac{f_1}{2} C \tag{4.3}$$

Once the compressed frequency comb bandwidth exceeds half the repetition frequency of the comb, the beating tones begin to overlap in the electrical domain, preventing a 1 to 1 imaging of the frequency comb. This upper limit on the detection frequency bandwidth is referred to as the Nyquist condition [123]. Once the combs are aligned so the lowest frequency line in both combs overlap and Eqn. 4.3 is satisfied, an image of the OFC can be generated in the RF domain with beating tones unique to single comb line pair interactions. Figure 4.5 shows a diagram of how a DFC could be utilised for spectroscopic applications. Here one of the OFCs is passed through a sample, exciting many transitions in the molecule simultaneously. Once the OFC passes through the sample, it is coupled with a second comb with a slight repetition rate offset. As

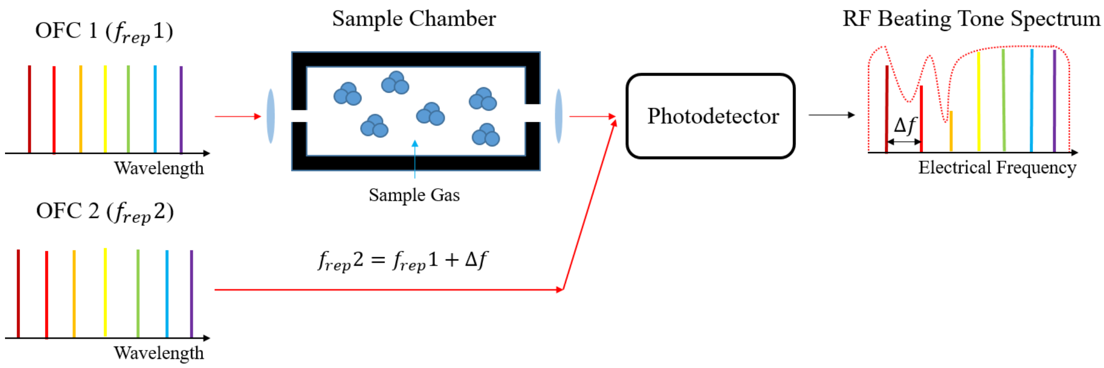

Figure 4.5: Spectrometer based on dual frequency comb architecture.

shown in Fig. 4.4, the resultant beating spectrum detected on a photodetector shows a reduction in beating tone powers at absorbed wavelengths. The resolution of this DFC is limited by the frequency spacing of the comb. Reducing the frequency spacing gives an increased resolution of the molecular absorption fingerprint in the OFCs bandwidth. The acquisition times for architectures like this are near real-time. The limit of the minimum time required to resolve a single down converted RF spectrum is $1/\Delta f$. Typically, this is in the millisecond range or below [124]. With this and Eqn. 4.1-4.3, the trade-off between acquisition time, optical bandwidth and repetition frequency can be seen. Beyond the advantages in acquisition time, the setup is simplistic with no moving parts and has the potential for full photonic integration. With the demonstration of a semiconductor based frequency comb source in the 2 μm wavelength region in Chapter 3, a potential ultra-compact simplistic spectroscopic detection device could be realised.

4.2 Coherence and Interference in Gain Switched Dual Frequency Combs

In this section, we discuss and demonstrate the effects of mutual coherence and interference between OFCs in DFC architectures. Through experimental demonstration, we show some of the key properties of DFCs and the measurement techniques required to characterise the DFC spectra. When collecting the beating spectra from two interacting OFCs in a DFC setup, the phase correlation between the two combs is paramount. High phase correlation between the two OFC allows for the generation of narrow beating tones between comb lines. With sufficiently narrow tones, the OFC information can be compressed, as shown in the previous section, into a narrow detection bandwidth without beat tone overlap. To explain this we can add a phase term to the RF intensity portion of the previously derived heterodyne beat note equation (Eqn. 2.5). This allows the beating tone dependence on phase difference between two comb lines to be analysed. The RF beat tone intensity is now described by:

$$I_{RF} = 2\sqrt{I_1 I_2} cos(\theta) cos(2\pi(f_1 - f_2)t + (\phi_1(t) - \phi_2(t))) \tag{4.4}$$

where $\phi_1(t)$ and $\phi_2(t)$ are the time dependant phases of the two frequency comb lines. This is still a simplified case as we have assumed, until now, that the signal frequencies are the same as the instantaneous frequency, which actually fluctuates with time. The instantaneous frequency of both signals can be defined as:

$$f_1 = \frac{d}{dt}(2\pi f_{01} + \phi_1(t)) = 2\pi f_{01} + \frac{d\phi_1(t)}{dt} \tag{4.5}$$

$$f_2 = \frac{d}{dt}(2\pi f_{02} + \phi_2(t)) = 2\pi f_{02} + \frac{d\phi_2(t)}{dt} \tag{4.6}$$

where f_1 and f_2 are the instantaneous frequencies of the two signals respectively. The phases of each signal are described by $\phi_1(t)$ and $\phi_2(t)$. The signal centre frequencies are defined as f_{01} and f_{02}. In the case described in Chapter 3, f_1 and f_2 equal f_{01} and f_{02}, as coherence was assumed, leading to cancellation of the phase terms. Now, in the case where two combs in a DFC setup have uncorrelated phase, the beat tone linewidth will be large as it results from the summation of the phase noise in both sources. With broad beating tones, reducing the frequency difference, $\Delta f = f_1 - f_2$, between the two OFCs, can result in an RF spectrum where the beating tones overlap or are unresolved. To address this issue there have been many phase-locking techniques used to correlate the phase of OFCs in DFCs setups, with varying degrees of success. Some techniques use analogue electronics, digital processing or computer algorithms to correct for phase differences between the frequency combs. These techniques allow for free running uncorrelated DFCs to be used for sensing, however, their performance has not come close to matching that of cavity locked systems [65]. Cavity locked DFCs use an optical injection technique to lock the phase evolution of the frequency combs to an external CW laser source. Through this method, the phase evolutions of the two OFCs are locked with very high coherence and long term stability. With this in mind, we set out to design a setup that took advantage of the gain

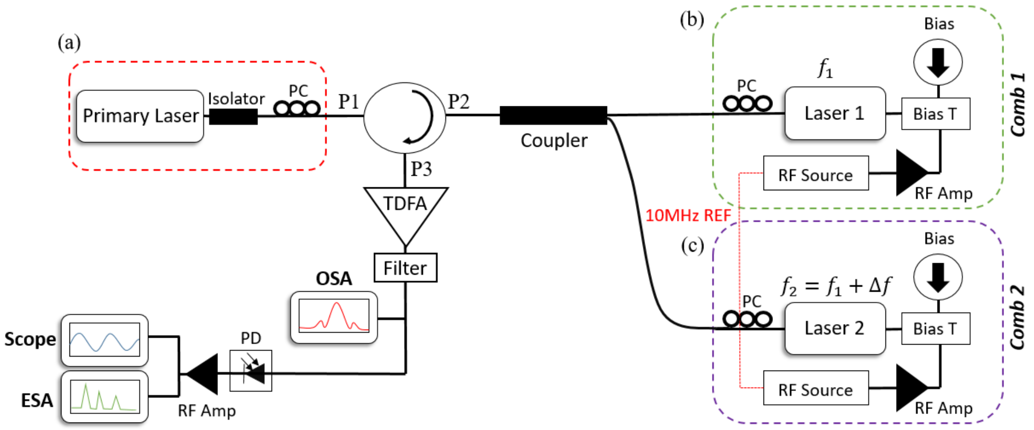

Figure 4.6: Experimental setup used to generate a coherent DFC through gain switching and injection locking semiconductor lasers operating at 2 μm.

switched OFC sources shown in Chapter 3 and a mutual injection locking, to generate a coherent DFC in the 2 μm wavelength region.

Figure 4.6 shows the experimental setup used to generate a coherent DFC through gain switching and injection locking of the InGaAs MQW DM lasers. A circulator, in combination with a 50/50 bi-directional coupler, was used to couple the primary laser, through P1, to both comb sources (Laser 1 and Laser 2) via port P2. Figure 4.7 shows the LI curve and frequency response characterisation of laser 1 and laser 2. The primary laser polarisation was tuned to allow for optimal injection locking of both lasers. Throughout all experiments, the injected power was -8 dBm for both Laser 1 and Laser 2. This power was measured after splitting of the primary laser signal at the coupler.

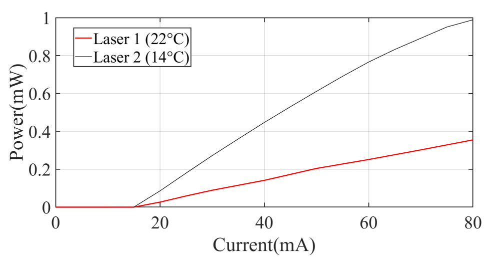

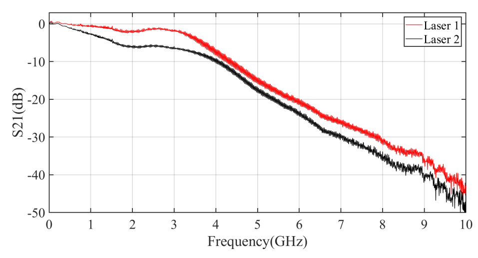

Figure 4.7: (a) LI curves and (b) Frequency responses for Laser 1 and Laser 2 in the DFC setup

Laser 1 and Laser 2 were biased using two independant current sources. The lasers were modulated using two RF current sources, which were locked to a common 10 MHz reference. The coherent DFC output was launched back through the circulator, exiting P3. The DFC optical signal was amplified using a TDFA and analysed using an OSA, sampling oscilloscope and ESA. To maximise the spectral overlap between the two OFCs, the emission wavelengths of the lasers were tuned through the device temperature. Laser 1 and 2 had an emission wavelength of 2002 nm at 22°C and 14°C respectively.

4.2.1 Mutual Injection Locking and Nyquist Aliasing

Injection locking of semiconductor lasers is well established and, and in Chapter 3, was shown to efficiently phase lock gain switch lasers at 2 μm. Through injection locking of two gain switched semiconductor lasers, the phase evolution of the two OFCs can be synchronised, allowing for the generation of ultra-narrow beating tones. Figure 4.8 shows beating tones generated between a single comb line pair in a DFC setup with and without (free running) mutual optical injection of the gain switched laser sources. These results were generated and captured using the setup shown in Fig. 4.6. In this plot, the free running DFC beating tone is shown in blue and the injection locked DFC in red. It can be seen that the free running DFC produces a much broader beating tone than the injection locked case. The FWHM of the

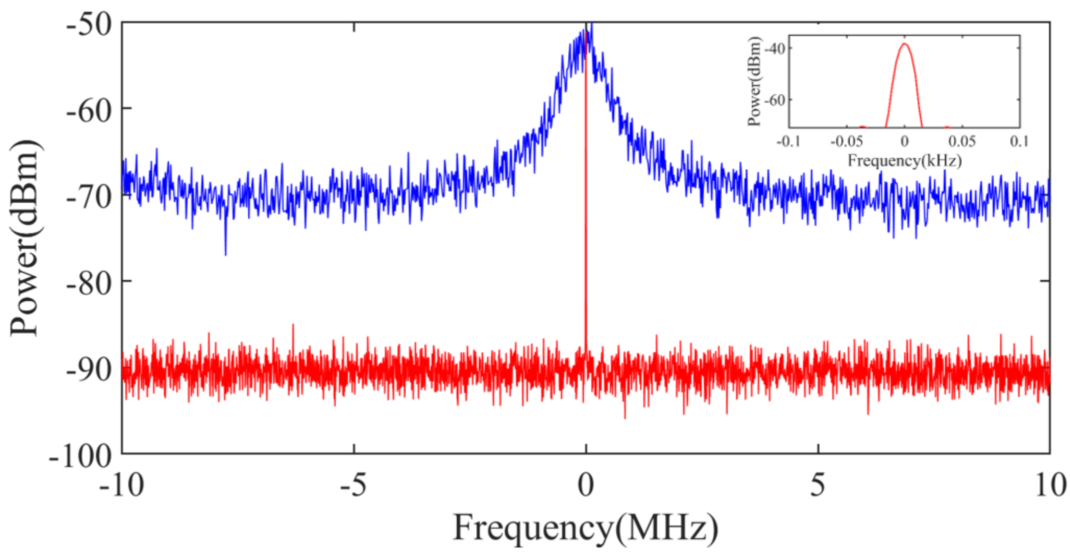

Figure 4.8: Beating tone generated between a single comb line pair in a free running DFC where the combs lack mutual coherence (blue) and an injection locked DFC with mutual coherence between the OFCs (red).

free running beat was measured to be 500 kHz. This trace was taken with 10 kHz resolution over a 30 ms sweep time. The FWHM of the injected tone was measured to be 11 Hz, taken with the maximum ESA resolution of 1 Hz, see top right Fig. 4.8. The much lower FWHM in the injection locked case shows the high coherence between the two combs in the DFC. There is also a clear reduction in the noise around the beating peak, showing a more general reduction in pulse-to-pulse noise in the injected OFCs. Figure 4.9 shows the effects of beat tone broadening on the acquired RF spectrum in a DFC setup. Note, both spectra were captured with 100 kHz resolution over a 300 ms sweep time. In Fig. 4.9(a) and (b), there are two RF beating tone spectra

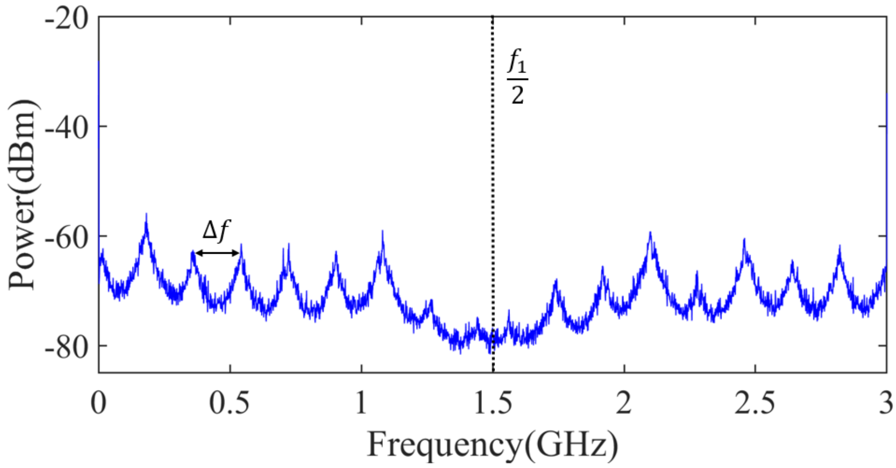

(a)

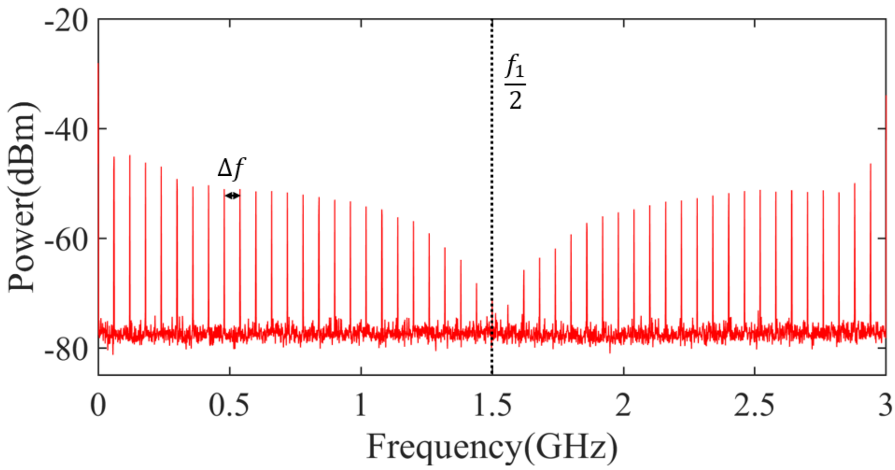

(b)

Figure 4.9: DFC beating tone spectra for (a) free running OFCs with no phase correlation between them and (b) mutually injected OFCs locked to a CW primary laser.

generated, mirrored around the frequency $\frac{f_1}{2}$, the Nyquist frequency. Mirroring occurs as for a beating tone generated at Δf, another is generated with the opposite comb line at $f_1 - \Delta f$. For the generation of broad DFC spectra with many beating tones, the frequency difference between the two OFCs must be small, allowing for all beating tones to be generated below the Nyquist frequency. The rationale for this was covered in Section 4.1.3. The potential effects of exceeding this frequency will be covered in this section, but first, we look at the effects of free running and injection locking on the DFC RF beating spectra. Figure 4.9(a) shows the RF spectrum generated by two free running OFCs generated. For this result, Laser 1 and Laser 2 were modulated with frequencies of 3 GHz and 3.18 GHz, resulting in a Δf of 180 MHz. Laser 1 and Laser 2 were modulated with switching amplitudes of 0 dBm and 4 dBm respectively. The broad beating tones limit the number of DFC comb line pair interactions that can be monitored below the Nyquist frequency, as reducing the Δf value would result in a loss of information due to overlap between neighbouring beating tones. Figure 4.9(b) shows the RF spectrum generated from a mutually injection locked DFC setup, where the lasers are modulated with 3 GHz and 3.06 GHz, resulting in a Δf of 60 MHz. With the reduced Δf and beat tone linewidth, the switching amplitudes could be increased to allow for the generation of OFCs with a larger bandwidth. The lasers were modulated with switching amplitudes of 12 dBm and 14 dBm respectively. The increase in detectable RF beating tones, each of which represents an optical comb line pair, shows the requirement for optical injection in DFC setups. This is of particular importance when f_1 is small, creating a limited detection frequency range below the Nyquist frequency. In the scenario where f_1 is much larger, say over 100 GHz, having a larger Δf would be less of an issue and injection locking of the two OFC sources may not be needed. However, the value of f_1 limits the sensing resolution of a DFC, making lower values more desirable.

In the case where the comb detection bandwidth exceeds the Nyquist frequency, overlapping of the mirrored beating tones can occur, referred to as aliasing. Figure 4.10(a) shows a scenario where the OFCs are modulated at 3 GHz and 3.099 GHz, resulting in a detection bandwidth which exceeds the Nyquist frequency. In this figure, the blue dashes outline the beating tones which are multiples of Δf, the primary comb, and the green dashes outline the beating tones which are multiples of $f_1 - \Delta f$, the mirrored comb. The issue

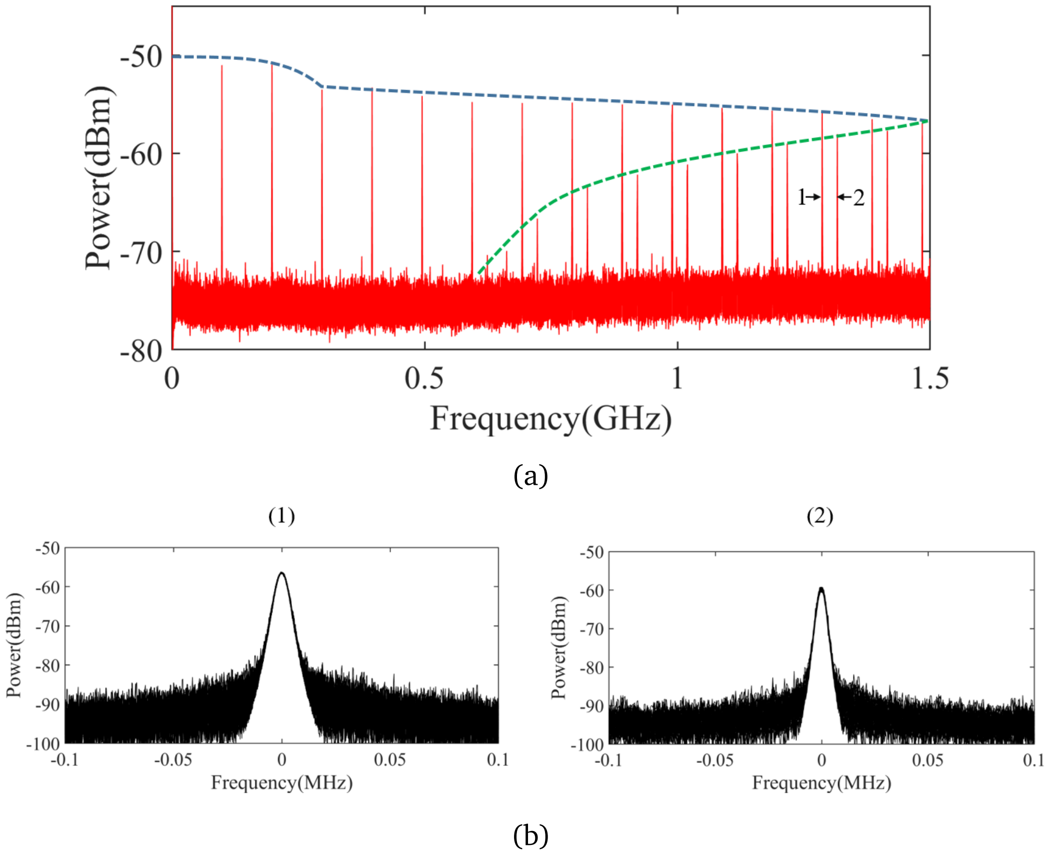

Figure 4.10: DFC RF beating spectrum where comb detection bandwidth exceeds the Nyquist frequency; (a) The blue dashes outline the primary comb and the green dashes outline the mirrored comb; (b) a collection of 50 sweeps with 10 kHz resolution for beating tones labelled 1 and 2.

with this scenario is the difficulty in removing the mirrored comb from the primary comb spectrum. Figure 4.10(b) shows a beating tone from the main comb and the mirrored comb recorded over 50 sweeps at 10 kHz resolution. Both beating tones are stable with minimal power fluctuations. However, this is not the case when the mirrored comb and primary comb share beating frequencies. Figure 4.11 shows the DFC beating spectrum when the OFCs are modulated at 3 GHz and 3.1 GHz, resulting in the mirrored and primary comb sharing beating frequencies. When recording the spectrum of one of the shared beating tones, Fig. 4.11(b), a beat tone power fluctuation (ΔP) is observed, allowing for the identification of beating tones generated by more than one OFC comb line pair interaction. This is of particular importance for managing injection symmetry, which will be discussed in the next section. With the detection window limited to a frequency bandwidth of $\frac{f_1}{2}$, free running OFCs are not an option for DFCs with low repetition frequencies, as is

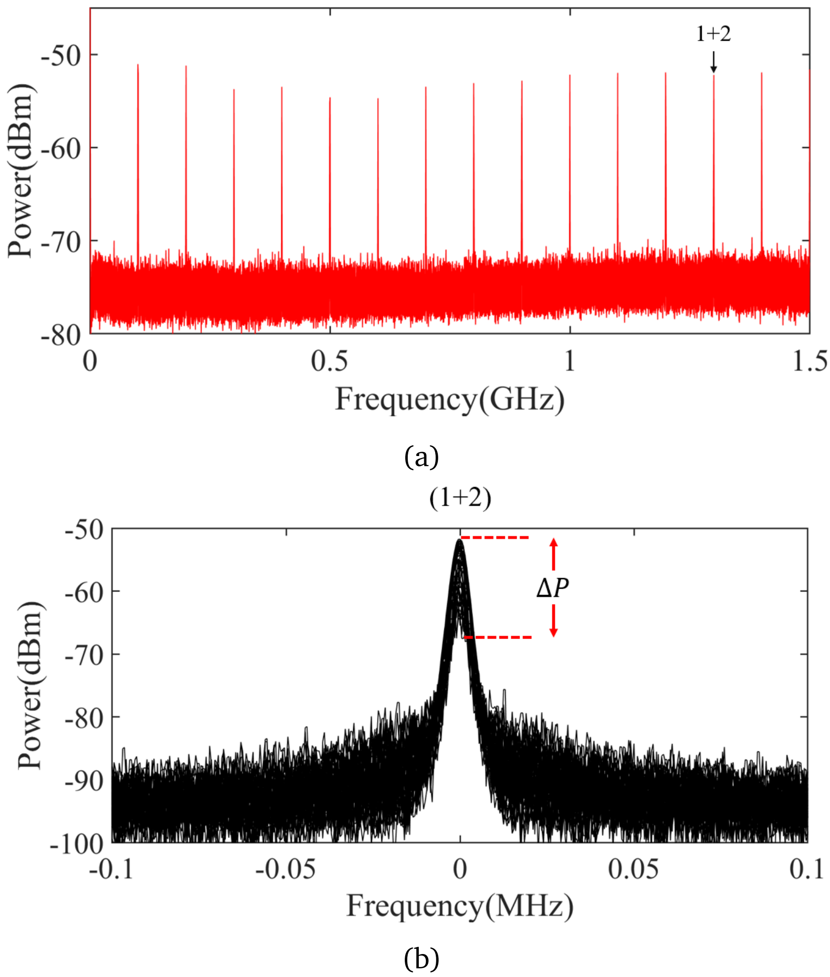

Figure 4.11: DFC RF beating spectrum where comb detection bandwidth exceeds the Nyquist frequency and the mirrored comb shares beating frequencies with the primary comb; (a) RF beating spectrum with shared beating tone frequencies making the mirrored and primary combs indistinguishable; (b) a collection of 50 sweeps with 10kHz resolution for the mixed beating tone labelled 1+2, showing large power fluctuations (ΔP).

the case here. Through the results shown above, it is clear that OFCs generated using gain switched semiconductor lasers and low repetition frequencies, require mutual coherence to produce RF beating spectra that are well resolved and compressed to a bandwidth below the Nyquist frequency.

4.2.2 Injection Symmetry Interference

When using a mutual injection locking technique for optical combs, the issue of beat tone symmetry arises. Figure 4.12(a)(i) shows how mutual injection locking leads to repetition of the beating frequencies around the injection frequency, f_{inj}. When detecting the DFC beating frequencies in the electrical domain, Fig. 4.12(a)(ii), the RF frequencies are generated from multiple comb line pairs, resulting in aliasing. This makes it impossible to identify the properties of the OFC. The repetition of beating frequencies is another form of aliasing similar to that which occurs when the comb detection bandwidth exceeds the Nyquist frequency. There are many approaches used to tackle the issue of beat tone symmetry in DFCs. The most popular of which is frequency shifting through interferometric setups including acousto-optic modulator (AOMs) [125, 126]. Frequency shifting recovers the maximum amount of beating tones, as it removes all symmetry around f_{inj}, but requires additional expense and complexity. The approach used in this project was asymmetric injection to a near edge comb line [127, 128]. This approach allowed for a simple and effective solution to DFC generation in the 2 μm waveband, where sourcing optical components can be difficult and costly. Figure 4.12(b)(i) demonstrates the premise of asymmetric injection and how it can be used to remove the majority of beating symmetries from the DFC. This method works by tuning f_{inj} away from the centre frequency of the OFCs, resulting in the majority of the symmetry around f_{inj} being removed. This allows for RF detection of beating tones unique to single comb line pair interactions, i.e. no aliasing, see Fig. 4.12(b)(ii). In practice, injection locking to the outermost comb line is not possible due to the instability of injection at those frequencies. This is due to the primary laser coupling to the secondary laser side modes, as

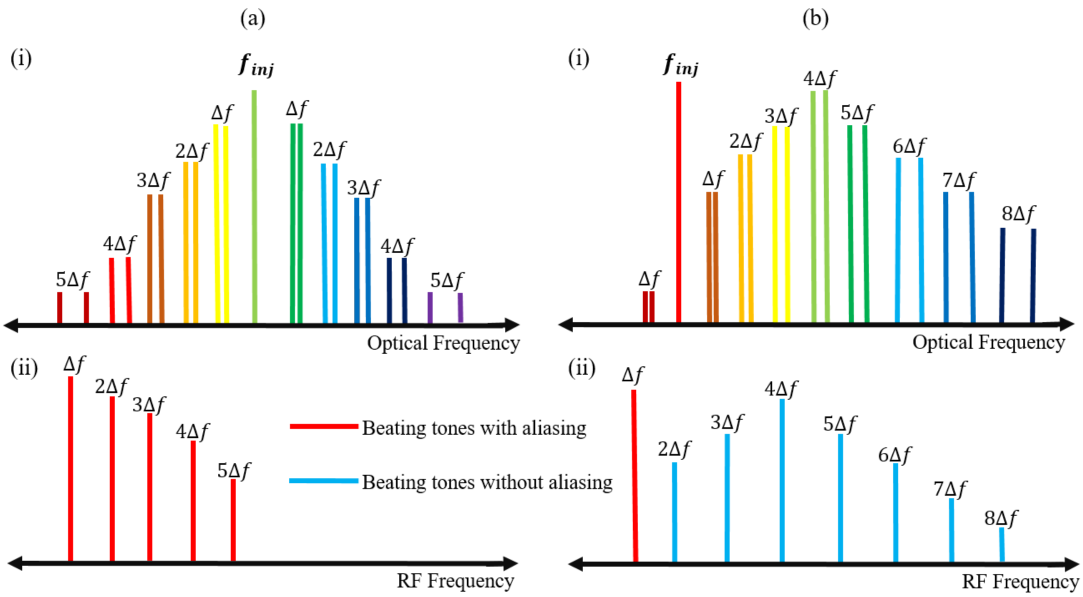

Figure 4.12: Illustrations of (a) symmetric and (b) asymmetric optical injection regimes in the (i) optical and (ii) electrical domains.

will be seen in section 4.3.1. This leaves some beat tone aliasing still present when using the asymmetric injection method, as shown by Δf in Fig. 4.12(b)(ii). We will refer to the portion of the DFC not influenced by symmetric beating tones as the functional bandwidth, shown by blue beating tones in 4.12(b)(ii).

Identification of aliased beating tones due to injection symmetry can be done in the same way as was shown for aliasing due to beat tone overlap beyond the Nyquist frequency, Fig. 4.11. Figure 4.13 shows the DFC beating spectrum collected when the OFCs were modulated with repetition frequencies of 3 GHz and 3.06 GHz respectively. Asymmetric injection was used to establish mutual coherence between the OFCs, removing the majority of the beating tone symmetry. Figure 4.13(b) shows how beating tones with and without aliasing differ in their power fluctuation. For Fig. 4.13(b)(1), the case where a beating

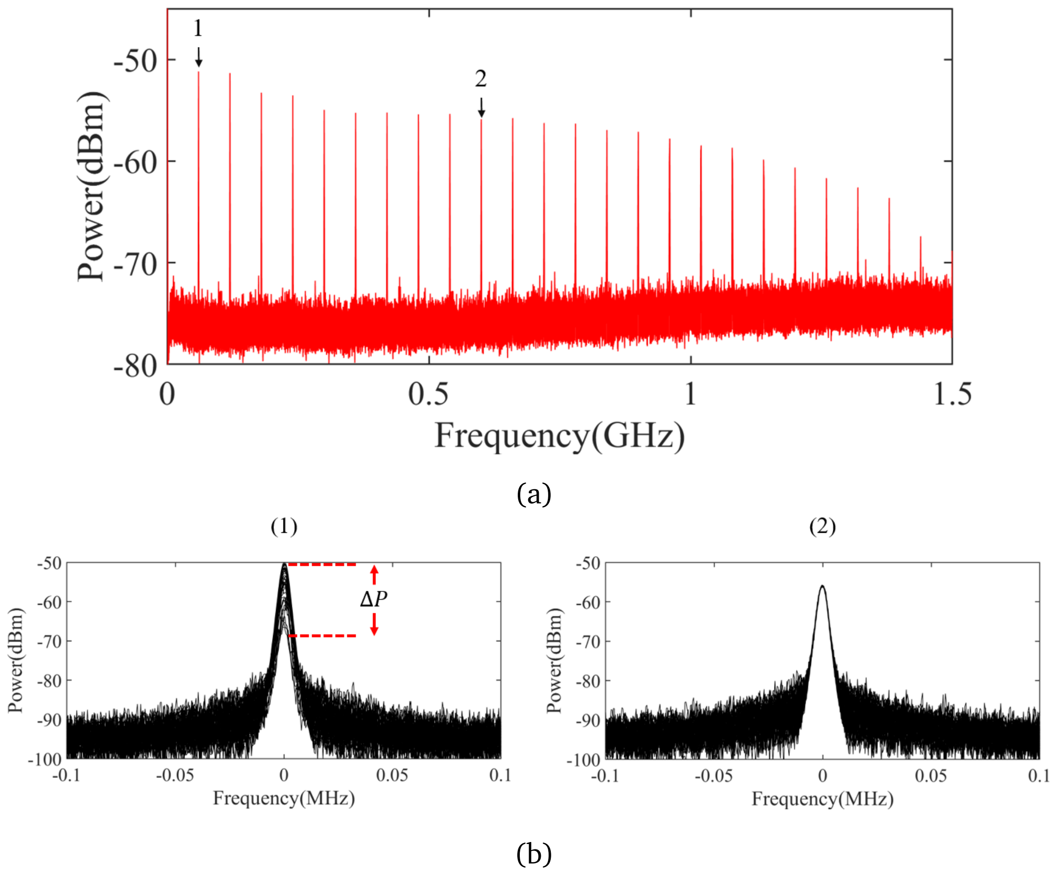

Figure 4.13: (a) Asymmetrically injection locked DFC beating spectrum; (b) Collection of 50 beating spectra with 10 kHz resolution for (1) a beating tone generated by multiple comb line pairs due to symmetry around the injection wavelength and (2) a beating tone generated by a single comb line pair.

tone is generated by more than one comb line pair symmetric around the injection frequency, a large beating tone power fluctuation is observed, as was the case for shared beating tone frequencies beyond the Nyquist frequency. Figure 4.13(b)(2), shows a beating tone recorded from the same spectrum, without a symmetric beating tone present. No power fluctuation is seen in this case. Through this method of identification of aliasing through ΔP values, asymmetric injection can be used to generate DFCs with known functional bandwidths.

4.3 Characterisation of Gain Switched DFC at 2 μm

In this section, we take the experimental setup and measurement techniques shown in Section 4.2 and generate a range of DFCs operating in the 2 μm wavelength region. For this characterisation, we looked at three DFC parameters. First, we studied the DFC injection locking range to determine the maximum injection detuning achievable in the asymmetric injection locking scheme. Second, we tested a variety of OFC modulation frequencies, aiming to increase the potential sensing resolution of the DFC by reducing the OFC frequency spacing. Lastly, we analysed the effect of comb compression on the detected DFC RF spectrum by reducing the frequency difference (Δf) between the OFCs.

4.3.1 Dual Frequency Comb Locking Range

With the functional bandwidth of the DFC limited by the potential symmetry between the beating frequencies around the injection frequency, we examined the injection locking range of the OFCs. Through maximising the asymmetry around the injection frequency, the functional bandwidth of the DFC could be optimised. For this experiment Laser 1 was modulated at 3 GHz with 12 dBm switching amplitude, Laser 2 was modulated at 3.06 GHz with 14 dBm modulation amplitude. Both lasers were biased at 30 mA and were injected with -8 dBm of optical power from the primary laser. Figure 4.14 shows the optical and electrical spectra generated by the DFC for a range of optical injection detunings. The detuning wavelengths were measured relative to the comb centre wavelength of 2002 nm. The shaded region in the electrical spectra shows beating tones which were generated by multiple comb line

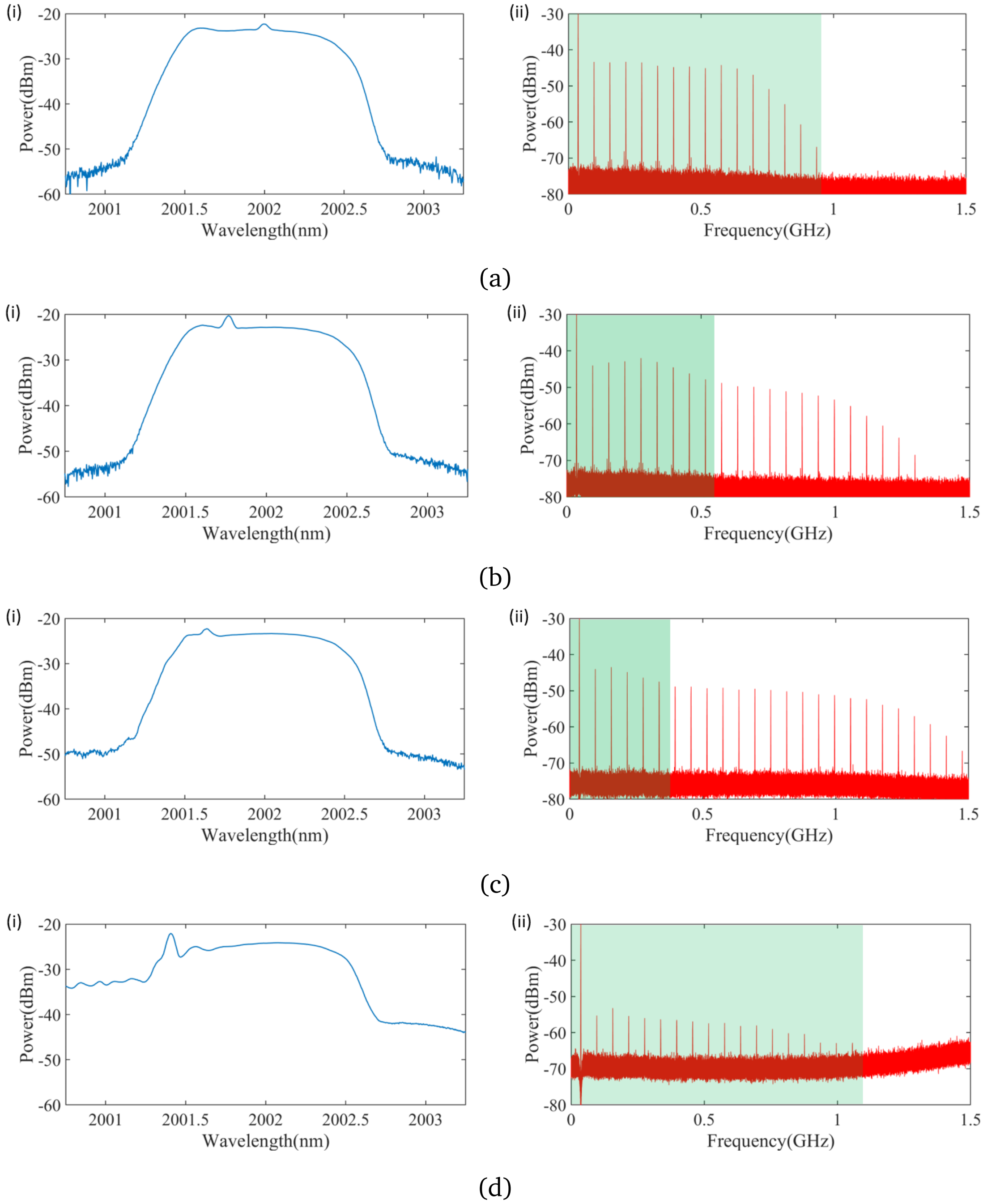

Figure 4.14: (i) Optical and (ii) electrical spectra for DFC with injection wavelength detuning from 2002 nm of (a) 0 nm, (b) 0.2 nm, (c) 0.4 nm, (d) 0.6 nm; The shaded portion of (ii) indicate frequencies at which symmetric beating tones cause a ΔP to exceed that of beating tones generated by single comb line pairs.

pairs, symmetric around the injection frequency. These tone were selected as the ΔP values exceeded 2 dB, the power fluctuation present in beating tones generated by a single comb line pairs for the selected modulation and detection parameters. The electrical spectra were captured at 100 kHz resolution with a sweep time of 128 ms. Figure 4.14(a) shows the case where the detuning of the injected laser from the comb centre wavelength is 0 nm. In this case the DFC is entirely symmetric, resulting in the minimum number of unique beating tones being generated. All beating tones were generated by more than one comb line pair, leading to a DFC with zero functional bandwidth. For Fig. 4.14(b) and (c) the detuning from 2002 nm was increased to 0.2 nm and 0.4 nm respectively. As the detuning increased the number of unique beat frequencies and functional comb bandwidth increased, due to increased asymmetry around the injection frequency. The maximum functional bandwidth achieved was 57 GHz for a detuning on 0.4 nm. When the detuning was increased to 0.6 nm, Fig. 4.14(d), the laser side mode began to unlock. As the frequency combs produced around the lasers main mode are reproduced at the side modes, unlocking of the side modes also cause issues with symmetric shared beating frequencies. This resulted in another regime in which the DFC had zero functional bandwidth.

4.3.2 Dual Frequency Comb Resolution

For DFCs, the resolutions they can achieve in sensing applications is equal to the comb line spacing. In chapters 2 and 3 it was shown that the optimal modulation frequency for the lasers used in this project was approximately 3 GHz. With the improved comb stability in the presence of optical injection, the repetition frequency could be reduced, improving the potential sensing resolution of the DFC. In this experiment, the OFC laser sources were modulated under the same amplitudes and biases as in the previous section. The repetition frequency of Laser 1 was varied from 3 GHz to 1 GHz, with Laser 2 modulated with frequencies required to keep the full DFC beating spectrum below the Nyquist frequency. Figure 4.15 shows the DFC beating spectra recorded for different OFC modulation frequencies. Through reducing the repetition frequencies of OFCs from 3 GHz and 3.06 GHz, Fig. 4.15(a), to 2 GHz and 2.02 GHz, Fig. 4.15(b), the number of beating tones detected increased from 24 to 44. The increase in beating tones is attributed both to the

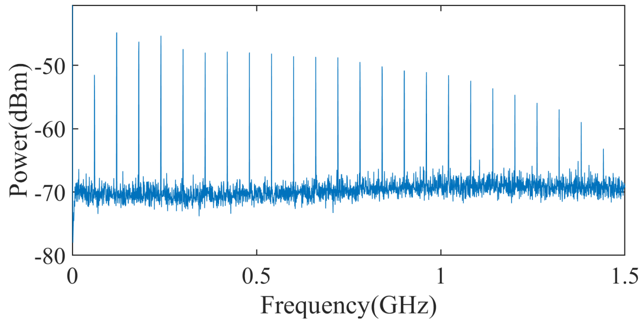

(a) $f_{rep} = 3$ GHz $\Delta f = 0.06$ GHz

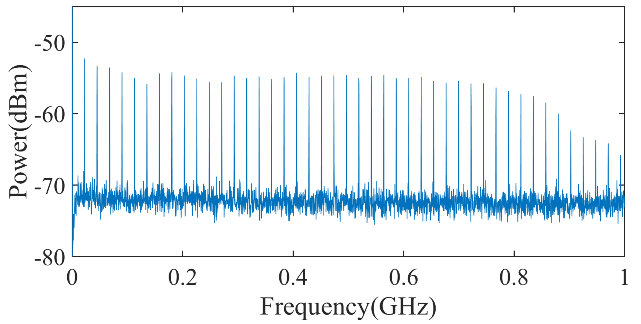

(b) $f_{rep} = 2$ GHz $\Delta f = 0.02$ GHz

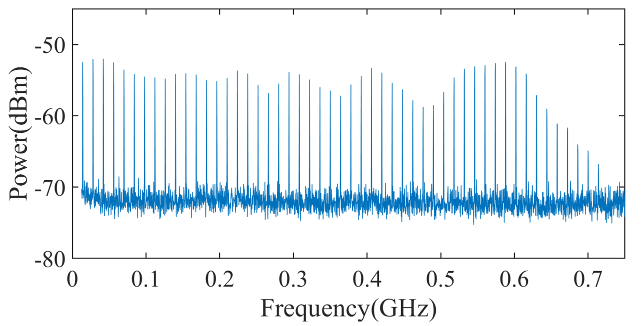

(c) $f_{rep} = 1.5$ GHz $\Delta f = 0.014$ GHz

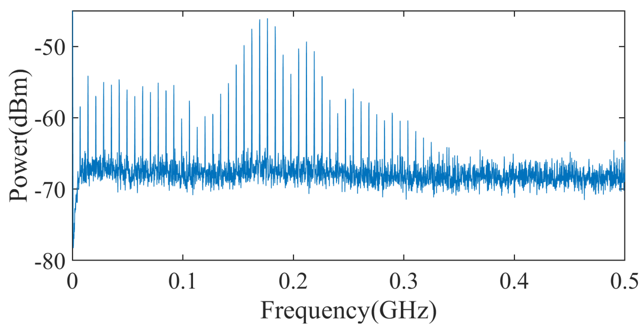

(d) $f_{rep} = 1$ GHz $\Delta f = 0.007$ GHz

Figure 4.15: DFC beating spectra for varying repetition and offset frequencies

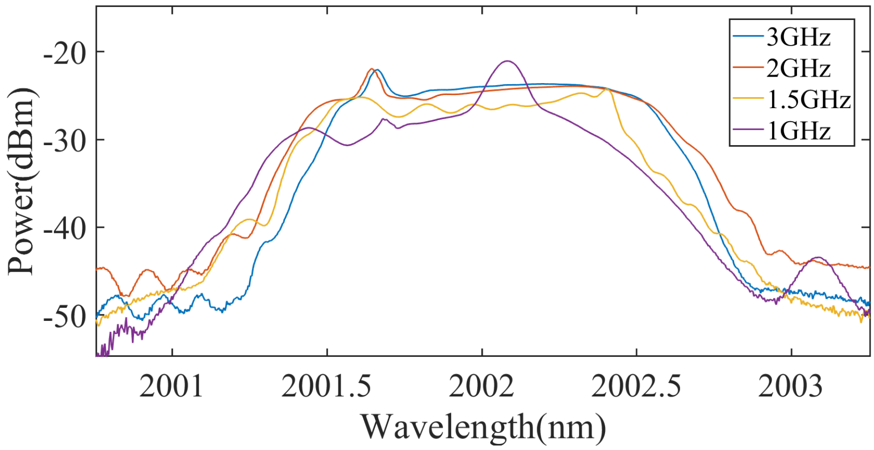

Figure 4.16: Optical spectra for DFCs with repetition frequencies ranging from 3 GHz to 1 GHz.

increase in comb line density in the optical spectrum and a slight increase in the overall optical bandwidth of the DFC, see Fig. 4.16. A reduction in beating tone SNR was also observed for the 2 GHz DFC. When modulated at 3 GHz the beat note SNR of mid spectrum beat at 0.72 GHz, was measured to be 21 dB. For the DFC modulated at 2 GHz, the mid note beat SNR at 0.497 GHz, was measured to be 17.4 dB. In DFCs it has been shown that SNR scales with increasing comb lines [129]. The SNR of a DFC ultimately determines its potential detection sensitivity. When the repetition frequency was lowered to 1.5 GHz, stable optical injection could no longer be achieved around 2001.6 nm. This was due to the laser side mode around 2001 nm unlocking under this injection regime. For the 1.5 GHz DFC the injection wavelength was switched to the opposite side of the OFC, at 2002.5 nm, where the side mode around 2003 nm remained locked. Although the number of comb lines generated in this case increased to 51, the lack of flatness in the beat tone spectrum makes this regime somewhat undesirable. Reducing the repetition frequency to 1 GHz, Fig. 4.15(d), caused the comb to lose the majority of its desirable spectral properties. A stable injection locking wavelength was difficult to achieve near an edge comb line. Instead, a stable injection could be achieved around 2001.7 nm, which resulted in an increased symmetry around the injected wavelength and an asymmetry in the Optical spectrum of the DFC. With a large flat spectral region and 44 beating tones spanning 88 GHz, 2 GHz was shown to be the optimal repetition frequency to operate the 2 μm DFC.

4.3.3 Comb Compression and Acquisition Time

Two of the key benefits of DFC architecture are the compression of OFC information into narrow sensing bandwidth and the improved acquisition time for RF spectra. In previous sections, all DFC spectra we collected for the maximum value of Δf required to capture the full DFC spectrum in the frequency range below the Nyquist frequency. The spectra were collected with 128 ms acquisition time per spectrum and 100 kHz resolution. Taking the results for the 2 GHz DFC, an SNR of 17.4 dB was achieved for beating tones in the flat section of the RF spectrum. As mentioned in the previous section the detection resolution of a DFC is determined by the comb line spacing and the sensitivity by the SNR. In this section, we explore the detection parameters and DFC compression to maximise SNR while minimising acquisition times.

Fig. 4.17(a) show DFC spectra recorded at resolutions ranging from 100 kHz to 3 kHz for Δf equal to 0.02 GHz, compressing the DFC data into a 1 GHz detection bandwidth. Through increases in ESA resolution and acquisition time, a large increase in SNR is observed. Note the SNR values were taken from the beating tone at 0.5 GHz. The SNR increased from 17.4 dB, for 100 kHz resolution, to 29.8 dB, for 3 kHz resolution. This came with an acquisition time penalty, increasing from 128 ms to 143 s. Through the reduction of Δf, the compression of the DFC RF spectrum increases, resulting in a reduced detection bandwidth and a reduced acquisition time. Table 4.1 shows how increasing the compression of the DFC spectrum reduces the acquisition time, while minimally affecting the achieved SNR. As the detection bandwidth is reduced, the resolution required to resolve the RF beating tones increases.

Detection Bandwidth	Δf (GHz)	Sweep time	SNR (dB)
1 GHz	0.02	12.9 s	25.9
500 MHz	0.01	6.44 s	25.5
50 MHz	0.001	644 ms	25.8
5 MHz	0.0001	64.4 ms	22.2

Table 4.1: Sweep time and SNR for DFC spectra captured with different compression factors.

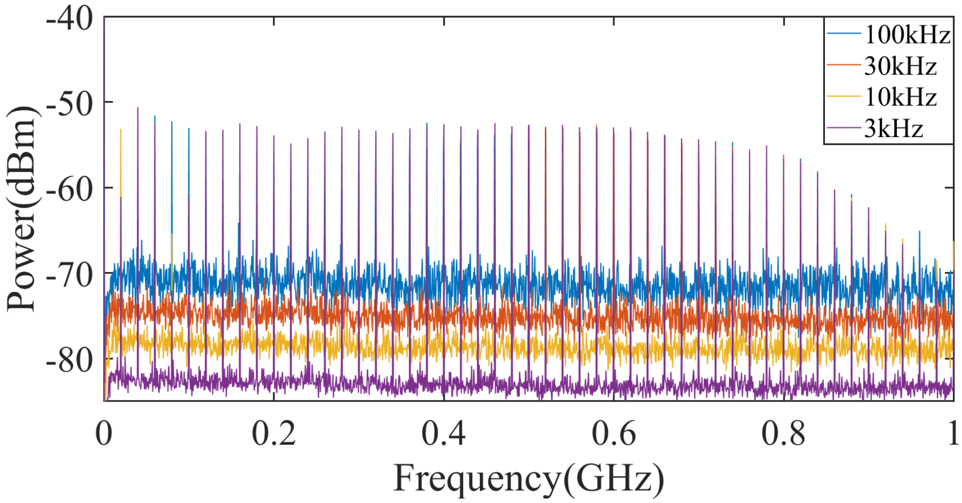

(a)

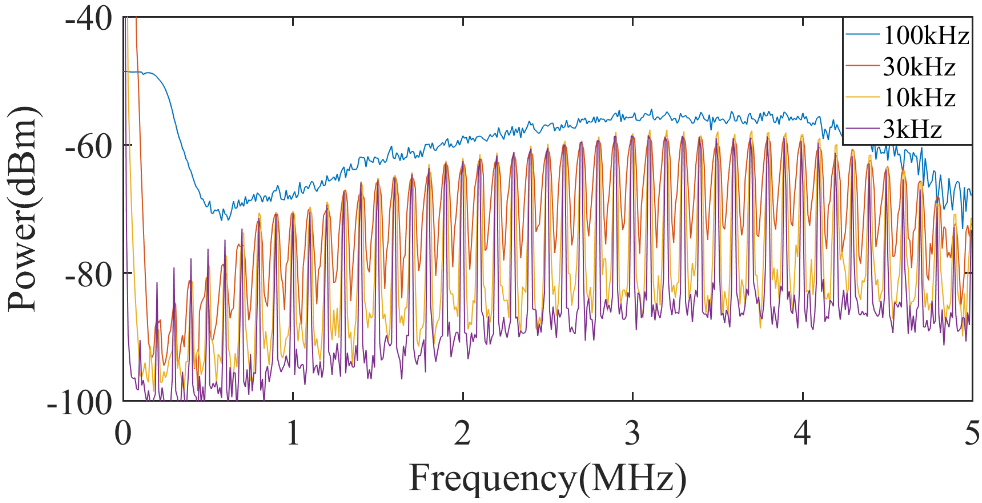

(b)

Figure 4.17: DFC RF beating spectra detected at increasing ESA resolutions and sweep times for (a) $\Delta f = 0.02$ and (b) $\Delta f = 0.0001$.

For the case where the DFC is detected in a 5 MHz bandwidth, see Fig. 4.17(b), the SNR values are no longer preserved for the lower resolutions, 100 kHz and 30 kHz. For 10 kHz the SNR was reduced by approximately 3 dB, but the tenfold reduction in acquisition time still makes this a desirable resolution. Through averaging of the DFC beating spectrum, the SNR can also see sizeable improvements. Figure 4.18 shows 25 DFC beating spectra in the case where there is no averaging (red) and averaging over 10 sweeps (black). The spectra were captured with single sweep time of 64 ms and resolution of 10 kHz. Through averaging, the SNR was increased from 22.2 dB to 27.5 dB. Beyond SNR reduction, averaging is also required to reduce the peak power

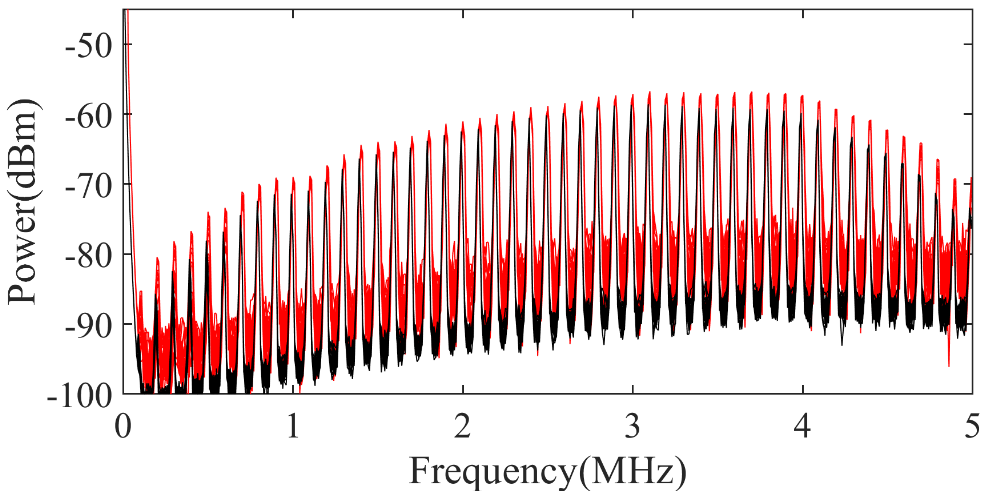

Figure 4.18: Collection of 25 DFC beating spectra detected with 10 kHz resolution for 64 ms individual sweep times with no averaging (red) and averaging over 10 sweeps (black).

fluctuations (ΔP). Without averaging a ΔP of 1.07 dB was measured for a mid-beating tone in the RF spectrum, at 2.49 MHz. With averaging over ten sweeps ΔP was reduced to 0.28 dB. Additional averaging over 20 and 50 sweeps only resulted in a slight reduction of ΔP to 0.21 dB.

With the resolution for the DFC detected in a 5 MHz bandwidth limited to 10 kHz and below, the Δf was increased to allow for a lower sweep resolution to be used. Using a lower ESA resolution in combination with averaging, a DFC

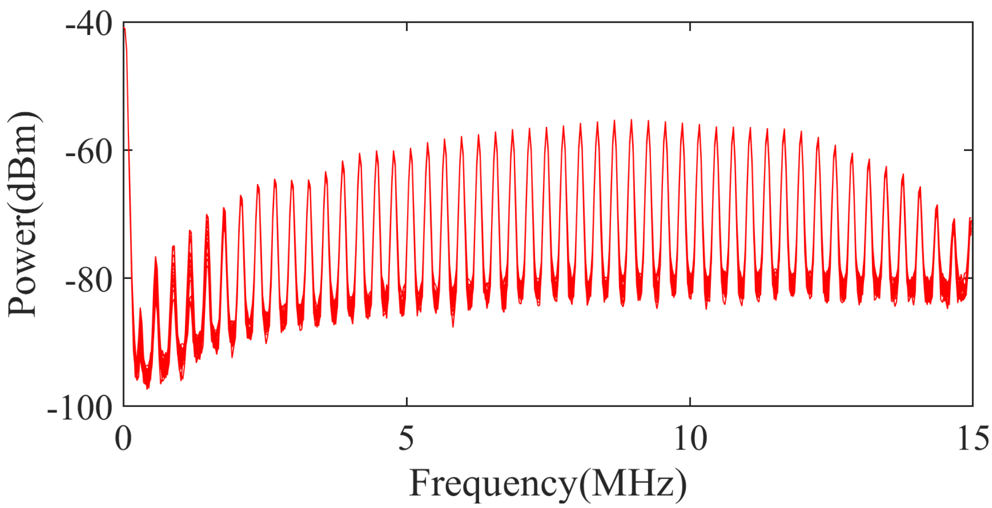

Figure 4.19: Collection of 25 DFC beating spectra detected with 30 kHz resolution for 5 ms individual sweep times averaged over 10 sweeps.

spectrum with both fast acquisition time, high SNR and minimal ΔP was generated. Figure 4.19 shows the beating spectra collected from the DFC with a Δf of 0.0003 GHz, resulting in a detection bandwidth of 15 MHz. The sweep time for an individual spectrum was 5 ms with 30 kHz resolution. The resulting comb spectra had a total acquisition time of 50 ms with an SNR of 25.7 dB and ΔP of 0.31 dB. The total number of comb lines generated was 49, translating to 98 GHz in the optical domain. As described in Section 4.3.2, some of these beating tones are not useful as they contain information from more than one comb line pair. This can be seen in the increased ΔP visible in the first 6 beating tones in Fig. 4.19. Taking this into account, 43 usable frequency lines were generated, which describe an 86 GHz functional optical bandwidth.

4.4 Summary

In this chapter, we discussed the topic of optical spectroscopy including broadband, swept laser and OFC approaches. The concept of DFC based spectroscopy was described allong with its potential to overcome some of the limitations in current spectroscopic systems. We demonstrated a DFC operating in the 2 μm wavelength region using mutually injection locked gain switched lasers. The effects of beating tone interference due to DFC RF spectra exceeding the Nyquist frequency and beating symmetries around the optical injection frequency were shown. For the optically injected DFC, the optimal repetition frequency was shown to be 2 GHz, producing a DFC spanning 98 GHz. The effects of DFC beating spectrum compression on SNR and acquisition time was explored. This showed a large variety of operating and detection conditions that can be selected depending on an applications need for high SNR or low acquisition time. Through compression of the DFC spectrum to a 15 MHz bandwidth, a DFC spectrum with 25.7 dB SNR, 50 ms acquisition time and 0.31 dB peak power fluctuation was demonstrated. This is the first time to our knowledge that coherent DFC has been demonstrated in the 2 μm wavelength region. In the conclusion of this thesis, we discuss the potential for the application of these DFCs and further research that could be carried out to improve and advance the proposed 2 μm DFCs.

Chapter 5

Development of Thulium Doped Fibre Amplifiers

Optical amplification is key in the testing and development of technologies in the 2 μm wavelength region. As the majority of devices in this waveband are in an early stage of development, optical losses are high and fine-tuned amplifiers are needed to maintain sufficient optical power for device testing. In this chapter, we discuss both the fundamentals of optical amplification at 2 μm using Thulium doped fibre amplifiers (TDFAs) and the development of TDFAs optimised for long-wavelength amplification between 1850 nm and 2 μm. The amplifier developed facilitated the experiments carried out in chapters 3 and 4. This chapter is broken up into four sections. Section 5.1 covers the physical fundamentals behind fibre amplifiers, from amplification through stimulated emission to optical pumping. Section 5.2 discusses the properties of the element Thulium and its use in rare-earth-doped fibre amplifiers. In Section 5.3, the experimental results are shown for four TDFAs in which the optical pumping schemes and doped fibre length were varied in an attempt to optimise gain in the 2 μm wavelength region. Section 5.4 summarises the results of the chapter and the merits of the fibre amplifiers developed.

5.1 Optical Amplification

There are many similarities between fibre amplifiers and lasers. They both rely on the previously described process of stimulated emission to generate amplified coherent light at a selected wavelength. Chapter 2 discussed the three key components of a laser source: a gain medium, a method of exciting the electrons in the gain medium and an optical cavity to provide resonant feedback. Similarly, fibre amplifiers consist of an excited gain medium but do not require an optical cavity. This allows light to make a single pass through the excited gain medium and achieve amplification through stimulated emission. Unlike the semiconductor gain media described in Chapter 2, a fibre amplifier's gain medium consists of a glass fibre with an additional element added to the glass. Through excitation of the added element, optical emissions can be achieved and guided through the fibre. In this section, we will discuss the fundamentals of achieving optical amplification using fibre gain media. By discussing the energy level properties of atoms, we will show how the cycle of optical absorption and emission can be used to generate amplification at desired wavelengths.

5.1.1 Atomic Absorption and Emission

In Chapter 2 we discussed the discrete energy levels of atoms and the formation of energy bands in semiconductor laser crystals. We discussed how the bandgap properties of semiconductor materials can be engineered to create stimulated emission when electrons are promoted to the conduction band. Fibre amplifier optical gain media typically consist of a glass fibre doped with a rare-earth element. The type of glass fibre and rare-earth element can be selected to optimise amplification at a variety of wavelengths. In fibre amplifiers, the electrons of the rare-earth elements are excited through photon absorption. For excitation through photon absorption to occur, the photon energy must be equal to the energy difference of the current electron state and the available excited state [130], see Fig. 5.1. In the case of optically excited gain media, a two level system as shown in Fig. 5.1 cannot be used to amplify light. With the energy absorbed and energy emitted by the electron transition being equal, a population inversion can not be achieved [131]. To use an optically excited gain medium for light amplification, the pump energy must promote an electron to an energy level higher than the desired emission energy. This is not possible in the simple two-level energy structures shown in

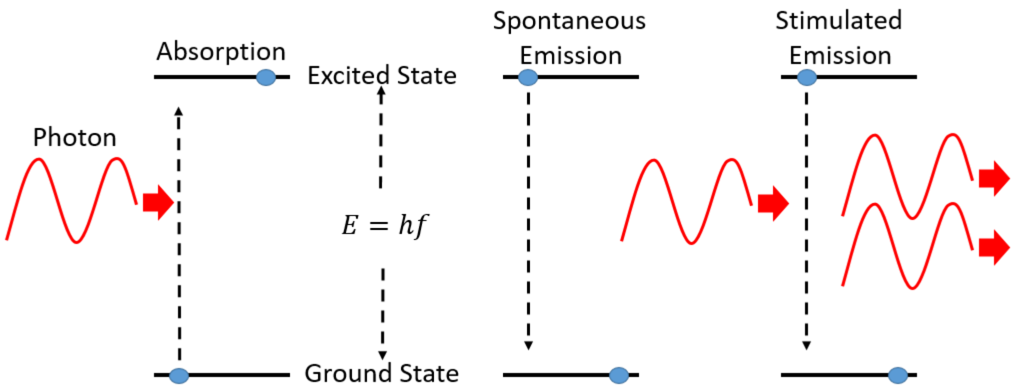

Figure 5.1: Description of the atomic absorption and emission processes.

Fig. 5.1, but can be achieved in reality due to processes that cause the energy levels in atoms to broaden and split, creating more energy levels which the excited electrons can occupy.

5.1.2 Energy Level Splitting in Atoms

Although the energy levels in atoms are discrete, some processes cause these energy levels to split and broaden. This results in additional discrete energy states around the original energy level. The structure of energy levels in an atom can be broken up into three main categories: the gross structure, fine structure and hyperfine structure. The gross structure describes the energy levels of an atom that contains spinless non-relativistic electrons [132]. This is a simplified case in which the energy levels depend only on the orbital kinetic and potential energy of the electrons. The energy levels are described by the principal quantum number of the electron state n, which in turn is described by the Azimuthal quantum number l [133]. The Azimuthal quantum number describes the orbital angular momentum of the electron and has non-negative integer values 0 to n-1. This simplistic representation of energy levels in an atom results in energy levels like the singular ones described in Section 5.1.1. The fine structure describes the splitting of atomic energy levels into sublevels due to the consideration of the electron spin in the atom [134].

Unlike the gross structure, which depends only on l, the fine structure takes into account the spin quantum number s, which describes the intrinsic angular momentum of the electron and has a value of $1/2$. The orientation of this momentum s, relative to the orbital angular momentum l, creates two new energy states depending on the total angular momentum J, where $J = l \pm s$.

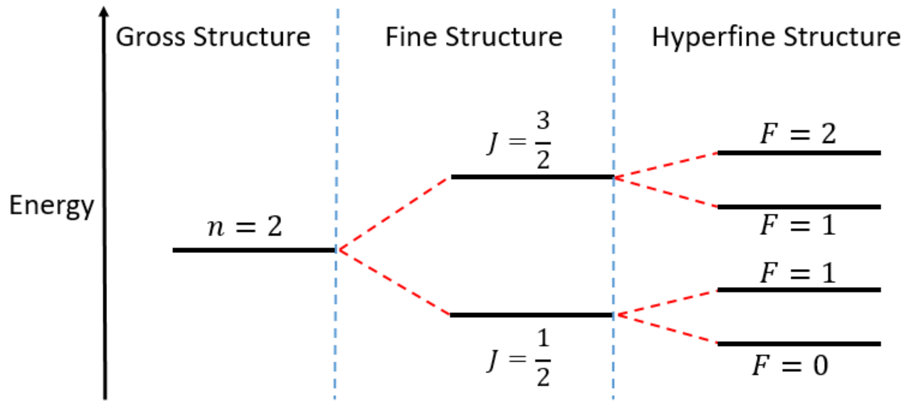

Figure 5.2: Plot of the Gross structure depending on orbital angular momentum and principal quantum number n; The Fine structure with the spin angular momentum taking into account to give the total angular momentum $J = 3/2$ for aligned momenta and $J = 1/2$ for opposed momenta; The Hyperfine structure when the nuclear spin $I = 1/2$.

When the momenta are in the same direction they are added together, giving a higher energy state and, when they are opposed, they subtract giving a lower energy state. Figure 5.2 shows the splitting in the case where $n = 2$, $l = 1$ and $s = 1/2$. This represents the spitting in a hydrogen atom which is the most simplistic case to explain these processes. Beyond the fine structure there is also the hyperfine structure of energy levels [135]. This describes the additional splitting of the energy levels in an atom due to the spin of the nucleus. This effect causes much smaller splitting due to the comparatively small magnetic moment of the nucleus when compared to the electron magnetic moment. The energy splitting is approximately three orders of magnitude smaller than that of the splitting induced by the electron spin in the fine structure but the mechanism is worth noting for a more complete picture of the energy levels in the atom. With the total angular momentum taking the electron spin into account, the more detailed total angular momentum, F, takes the nuclear spin I into account, with $F = J \pm I$. Like the electron spin, the nuclear spin takes on half-integer values when there is an odd number of protons or neutrons in the nucleus. In the case of even protons and neutrons, the net nuclear spin is zero. Much like the fine structure, the hyperfine structure depends on the alignment of the nuclear spin with or against the total angular momentum J, producing lower energies when opposed and higher energies when aligned, see Fig. 5.2.

5.1.3 Stark Splitting

The processes involved in the creation of the fine structure and hyperfine structure are internal and depend on the interactions of the nuclear spin, electron spins and orbital angular momentum. Additional splitting and broadening of energy bands is introduced when external fields acting on the atom are taken into account [136]. The Stark effect describes how an external electric field causes additional splitting and broadening of atomic energy levels through breaking degenerate energy states [137]. A degenerate energy state is one in which the energy value is the same for more than one configuration of the system. This usually implies there is some symmetry between these configurations which have the same energy values [138]. When an electric field is applied to the atom, the symmetry is broken by changing the symmetric distribution of the electrons and nucleus. The electrons and nucleus are pushed and pulled by the electric field creating a new charge distribution in the atom which is not symmetric. The addition of a directional field that affects the electrons and neutrons creates additional states depending on alignment or opposition to the field. The splitting of the energy levels increases with the electric field strength and overlap of the energy levels can occur in strong electric fields, see Fig. 5.3. The splitting is also dependant on the distance of the electron shell to the nucleus. As the distance increases, represented here by increasing principal quantum number n, the electrons in the shell become less bound to the nucleus allowing for them to be moved more by the electric field, increasing the intensity of the energy level splitting.

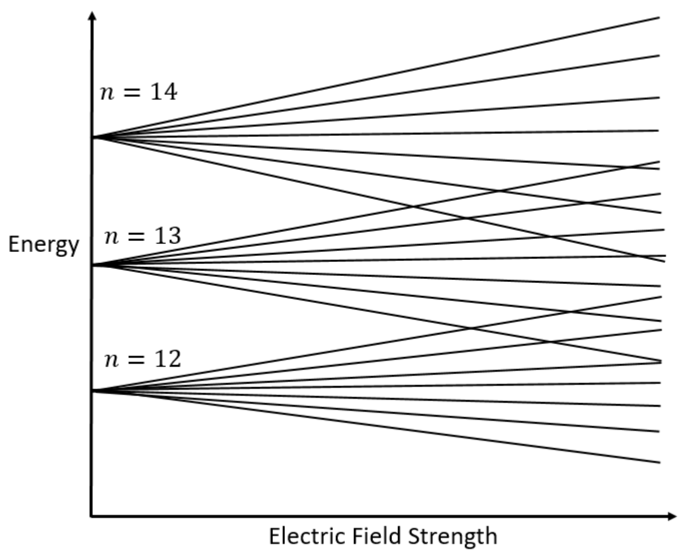

Figure 5.3: Plot of the Stark splitting of energy levels in the hydrogen atom.

Fig. 5.3 shows the splitting of energy levels due to the Stark effect in the hydrogen atom. The Stark effect is a very important part of the description of emission energies of fibre amplifies as the Stark effect is the dominant broadening effect present, leading to emission spectra spanning hundreds of nanometers [139].

5.1.4 Optical Pumping

As mentioned in Section 5.1.1, a two energy level system cannot be used to amplify light through stimulated emission as the energy of the light used to excite the electron is the same as the energy of the light which stimulates emission. Now considering the energy level splitting, which is induced by internal and external fields interacting with an atom, optical pumping can be used to create an excited gain medium that can produce optical amplification, illustrated in Fig. 5.4. This type of optical pumping is called in-band pumping, as the absorption and emission are occurring in the same energy band. In this scenario, a photon of energy hf_1 is absorbed by the atom, promoting an electron into one of the higher energy states. This electron then relaxes to a lower energy level in the band, which can be stimulated to emit by a photon of energy hf_2 where $hf_2{<}hf_1$. Here h is Planks constant and f_i is the frequency of the photon. For the relaxation process to occur, the absorption and emission must be occurring in an atom which is amongst a collection of atoms in an elastic system [45]. The energy lost in the relaxation process is transferred

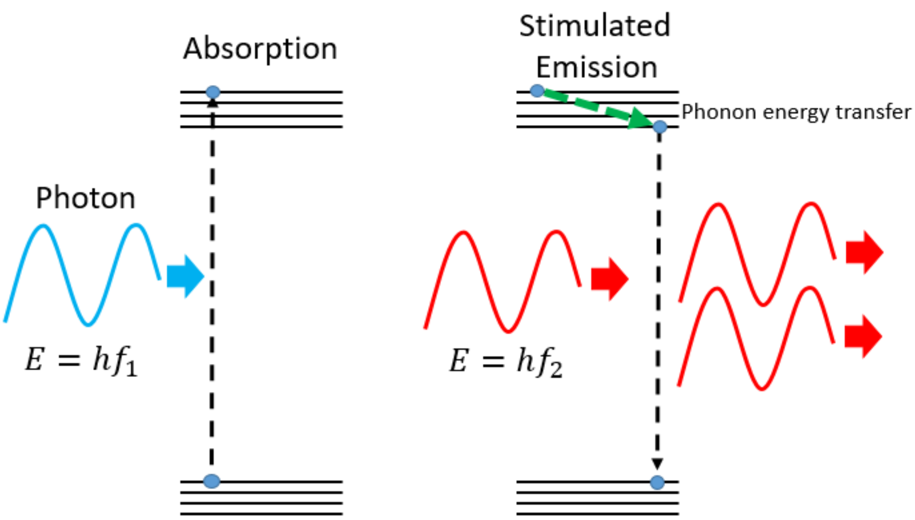

Figure 5.4: Diagram showing in band absorption and stimulated emission in an atom with split energy levels.

through phonons in the elastic collection of atoms [140]. In fibre amplifiers, the process of exciting the electrons through photon absorption is called pumping, and the frequency f_1 is referred to as the pump frequency. The photon that causes stimulated emission is called the signal, with f_2 being the signal frequency. Through this cycle of absorption of light at the pump frequency and stimulated emission of light at the signal frequency, amplification is achieved.

5.2 Fibre Amplifiers

Fibre amplifiers have become an integral part of photonics, seeing widespread use in fundamental research and industrial applications. They were first developed using Erbium-doped silica fibre in the 1980s [141]. Due to the emission wavelength of Erbium matching both the low loss wavelength of silica fibre and the emission band used in optical communications, they were implemented as repeaters for long haul optical communications [4]. This innovation revolutionised optical communications, enabling high capacity long haul optical links. To date, they are still the preferred method used for amplification of long haul fibre communications. In this section, we first discuss the effect of rare-earth ion and glass host selection on fibre amplifier absorption and emission properties. We then focus on the properties of Thulium, the rare-earth ion used for amplification around 2 μm, in more detail. Lastly, we discuss the design concepts for a fibre amplifier operating around 2 μm, based on Thulium doped silica fibre.

5.2.1 Rare-Earth Elements

A fibre amplifier gain medium is based on a glass fibre to which an active element has been introduced. This process of adding an element to a glass fibre is called doping [142]. Fibre gain media are traditionally made using glass fibres which are doped with lanthanide rare-earth elements. The rare-earth elements have properties that make them ideal candidates for fibre amplifier active elements. Due to the electron structure in rare-earth elements, Stark splitting becomes prominent when these elements are added to a glass host [139]. Stark splitting of the energy levels is induced by the electrostatic field preset around the rare-earth elements when they are embedded in a glass host [143]. This electric field causes the degenerate energy levels present in

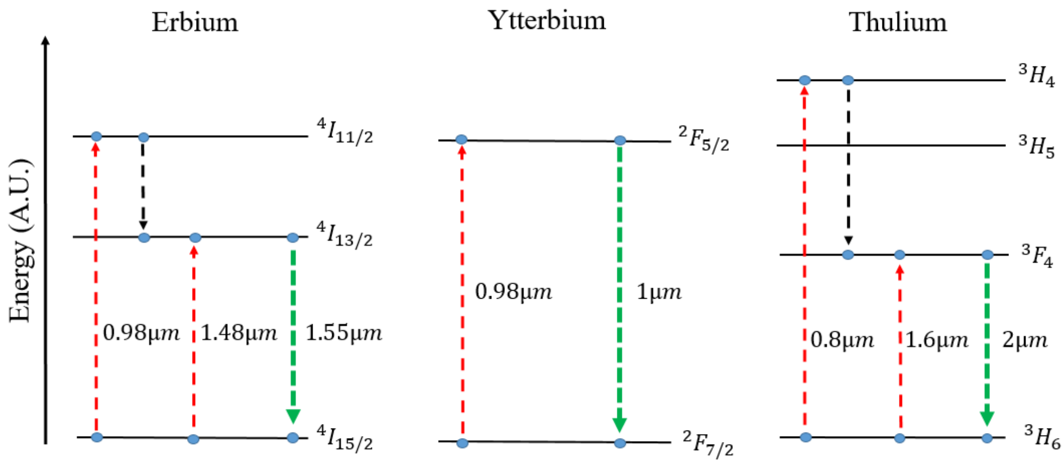

Figure 5.5: Energy level diagrams of earth elements Erbium, Ytterbium and Thulium. In each case red arrows represent absorption wavelengths, black arrows represent nonradiative transitions and green arrows represent emission wavelengths.

the rare-earth elements to split as described in Section 5.1.3. This process, with a particular focus on the rare-earth element electron structure, will be elaborated on in the coming section. The splitting of these energy levels creates a very broad amplification spectrum where many wavelengths can be absorbed and emitted. Broad amplification spectra are much sought after as they allow for versatile amplification of many wavelengths using a single device. The emission and absorption wavelengths of rare-earth elements cover a broad range of the near-infrared spectrum.

Fig. 5.5 shows the simplified energy level diagrams for three rare-earth elements, regularly used in fibre amplifiers. The illustrations are simplified as they do not explicitly show the energy splitting for each energy level. Erbium is used for its emission wavelengths between 1.52 μm and 1.58 μm. Ytterbium enables amplification of signals at 1μm-1.1μm [144]. Thulium, which is the rare-earth element focused on in this thesis, produces emissions between 1.7 μm and 2.1 μm. Up to this point, we have only discussed in-band pumping schemes, where the pump wavelength is absorbed and signal wavelength is amplified by electron transitions in the same energy band. In Fig. 5.5, in-band pumping is shown to work for the three rare-earth elements and is the only pumping scheme for Ytterbium. For Erbium and Thulium, an inter-band pumping scheme is also shown, where a shorter wavelength pump light can be absorbed, leading to electron excitation to an energy level above the first excited state. In this pumping scheme, a inter-band nonradiative process occurs, allowing for the excited electron to fall to the first excited state. This method of indirectly populating the first excited state can be used, in some cases, to achieve an improved conversion efficiency of pump light to signal light. An example of this would be stronger absorption at the lower pump wavelength, allowing for rapid absorption of the pump light, in turn leading to a densely populated first excited state.

5.2.2 Rare-earth-doped Glass Host

The glass host plays an important role in the amplification properties of rare-earth-doped fibre gain media. The transparency at certain wavelengths and mechanical properties of the fibre, such as brittleness, are important to consider when designing fibre gain media. Beyond these considerations, the glass host greatly affects the properties of the rare-earth elements energy levels and electron transitions [145]. For clarity, we will refer to the rare-earth elements as ions as they exist naturally in an ionic state. There are two key interactions that take place when rare-earth ions are introduced to a glass host: ion-dynamic lattice interactions and ion-ion interactions.

Ion-dynamic lattice interactions refer to the interactions that take place between the rare-earth ion and its surrounding glass lattice. One of the primary interactions affected by the lattice is multiphonon transitions. Multiphonon transitions are nonradiative processes where electrons can lose energy to lattice vibrations in a glass host [146]. These relaxations are what allow for electron transitions to the first excited state in indirect optical pumping schemes, as described in the previous section. As the lattice properties of glass hosts differ, different phonon energies are present in each host. For example, silica-based glasses have a high maximum phonon energy, 1100 cm^{-1}, while fluoride glasses have a relatively low maximum phonon energy, 500 cm^{-1} [147]. The phonon energy of a glass host determines the probability of multiphonon transitions occurring. The probability of these transitions is dependant on the number of phonons required to facilitate the relaxation of the electron. High phonon energy glasses have a high probability of nonradiative multiphonon relaxation as they require few phonons to make the transition. This makes glasses like silica desirable for indirect pumping schemes where rapid depopulation from the higher excited state to the first excited state is required. Low phonon energy glasses, like fluoride glasses, have the opposite effect, reducing the probability of multiphonon relaxations. This can be desirable for some applications as it reduces the depopulation time of the upper excited energy level. By doing this, metastable energy levels can be created, allowing for excited-state optical emissions to be achieved. For example, this method of rare-earth doping in a low phonon energy glass host has been used to create Thulium lasers where optical emission occurs between the third and first excited state ($^3H_4 -^3 F_4$), emitting at 1.47 μm [148].

Ion-ion interactions describe the processes which can take place between two or more rare-earth ions in the glass host. Two processes that fall into this category are cross relaxation and energy transfer upconversion. Cross relaxation is an ion-ion energy transfer process where an electron in one ion can transfer its energy to an electron in a neighbouring ion. In doing this the first electron is relaxed to a lower energy level and the second electron is promoted to a higher energy level [149]. Cross relaxation transfers energy through a reorientation of the spins in dipolar-coupled ions. As a dipole-dipole interaction, cross relaxation is dependant on the distance between the ions in the glass host. Through increasing the concentration of the ions, i.e. reducing the potential distances between ions, the cross relaxation process can become more prominent [150, 151]. The cross relaxation process can be used to increase the efficiency of fibre amplifiers and will be discussed in more detail, as it relates to Thulium doped fibre amplifiers, in Section 5.2.5. Energy transfer upconversion is an ion-ion interaction, similar to cross relaxation, where an electron falls to a lower energy level, transferring its energy to an electron which is promoted to a higher energy level. For upconversion processes, the final state of the electron which has received the energy promotion is above the energy achieved through the pumping mechanism [152]. Upconversion can be both a desirable and undesirable process. Upconversion lasers use the process to populate additional excited states beyond the energy supplied by the pump laser absorption. An example of this is infrared-pumped visible lasers [153]. Upconversion can also lead to unwanted depopulation of the desired emission energy level and result in nonradiative electron transitions from the emission level excited state. As these nonradiative processes are dipole-dipole interactions, which again are distance dependant, there is an upper limit on the concentration at which ion doping can be used while avoiding excess upconversion. This effect of reduced lasing efficiency at high ion concentrations is called concentration quenching [154].

5.2.3 Thulium Absorption and Emission Spectra

Thulium (Tm3+) is the rare-earth ion of choice for amplification around 2 μm [155]. As is common with rare-earth ions, Tm3+ is trivalent. This is shown by the plus three positive charge on the ion. It has been shown that rare-earth ions have a few atomic structural properties which make them ideal choices for light generation sources when embedded in a glass host. Emission from rare-earth ions occurs in the $4f$ electron shell [156]. This shell would usually have the largest radius in the atom as it is the outer shell but, in rare-earth ions, this shell contracts to have a radius smaller than the $5s$ and $5p$ shells [157]. The closer proximity to the nucleus and shielding by the outer $5s$ and $5p$ shells reduces the intensity of the Stark effect on the $4f$ shell, which is induced by the electrostatic field in the crystal host [158]. There is still a broadening of the energy levels in this shell but the reduced strength of this Stark effect prevents unwanted overlapping of the energy levels, resulting in a broad energy band with a collection of discrete energy levels for optical emission. Compared to other rare-earth elements, Tm3+ displays one of the largest emission bandwidths, approximately 400 nm ($\approx$35 THz) [159]. This dwarfs some of the commonly used rare-earth ions used for amplification like Erbium, with a 60 nm ($\approx$7 THz) bandwidth, and Ytterbium, with a 100 nm bandwidth ($\approx$27 THz). The broad emission spectrum of Tm3+ around 2 μm, induced by the properties of trivalent ions when embedded in a glass host, makes Thulium doped Fibre (TDF) an ideal material for optical amplification at 2 μm.

Thulium has absorption and emission spectra ranging from 400 nm to 2200 nm, with a variety of ground state and excited state transitions. Figure 5.6 shows this spectrum in the case where Thulium is doped in a silica host [160]. The plot shows the emission (red), ground-state absorption (black) and excited state absorption cross-sections. For applications in the 2 μm waveband, the emissions from the $^3F_4$ to $^3H_6$ energy levels are of interest. When designing a fibre amplifier the choice of pump wavelength has a large effect on the amplification potential. For a Thulium doped fibre amplifier (TDFA), there are two primary pump wavelengths used. Firstly, 1550 nm can function as an in-band pumping wavelength, exciting the $^3H_6 -^3 F_4$ transition. Although the absorption cross section at this wavelength is relatively low, there are benefits to using in-band pumping which will be discussed in the next section. The second pump wavelength is 785 nm, exciting the $^3H_6 -^3 H_4$ transition. This wavelength has the highest absorption cross section in Thulium. Using a

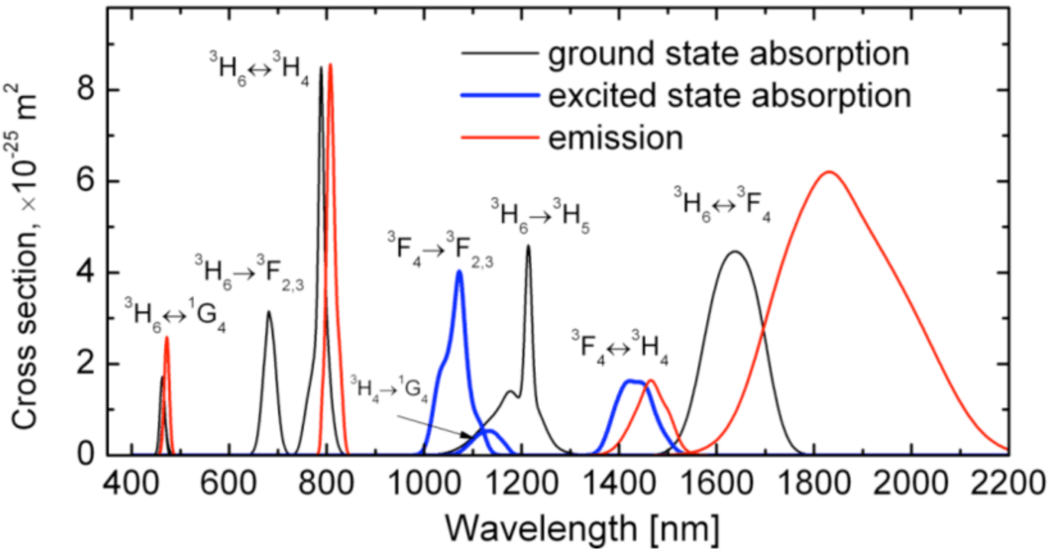

Figure 5.6: Plot of absorption and emission cross sections for Thulium in a silica glass host [160].

wavelength with a high absorption cross section allows for fast and efficient absorption of the pump light over a short length of the fibre. As this is an indirect pumping scheme, exciting the $^3H_6$ energy level, relaxation processes are required to populate the $^3F_4$ level. As discussed in Section 5.2.2, these processes are either multiphonon transitions or an ion-ion interaction. The specifics of these processes as they relate to the 785 nm pumping scheme are discussed in Section 5.2.5.

5.2.4 Pumping at 1550 nm

In this thesis the first TDFA pump wavelength studied was 1550 nm, exciting the transition between the $^3H_6 -^3 F_4$ energy levels. Looking at Fig. 5.6, it can be seen that the absorption cross section at this wavelength is relatively low at $2 \times 10^{-25} m^2$. This would imply 1550 nm is an inferior wavelength to pump Thulium as the absorption process is less efficient, however, there are additional variables that need to be taken into account when choosing a pump wavelength. Due to the decades of development of laser devices at 1550 nm, with telecommunications mostly operating at this wavelength, high power laser diode sources are easy to obtain and relatively cheap when compared to other more specialised wavelengths. Pumping with 1550 nm is also an in-band pumping scheme as the excitation and emission happen in the same energy band. When an electron absorb light at 1550 nm they it loses some of that energy to thermalisation processes, reducing its energy to a level where it can

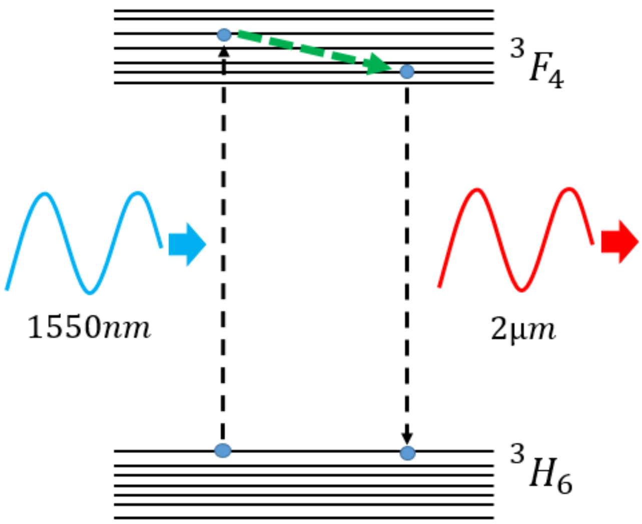

Figure 5.7: Energy level diagram of Thulium(Tm3+) pumped at 1550 nm and emitting at 2 μm.

emit light at 2 μm. These processes are ultrafast, on the order of picoseconds [161]. This allows for an efficient conversion of pump light to lower energy signal light. For indirect pumping schemes, relaxation processes can be radiative or non-radiative, depending on whether they use photons or phonons to reduce the excess excitation energy. The probability of these processes occurring vary and can cause a bottleneck in the amplification process by reducing the efficiency of converting pump light into signal light. For the 1550 nm in-band pumping scheme, the low absorption cross section may reduce the efficiency of the absorption of pump light but the ultrafast thermalisation allows for high pump conversion efficiency.

5.2.5 Pumping at 785 nm

Pumping Thulium at 785 nm holds the advantage of a very high absorption cross section, allowing for efficient absorption at this pump wavelength. This process promotes an electron from the $^3H_6$ to the $^3H_4$ energy level. The emission level ($^3F_4$) is populated through multiphonon transitions and cross relaxation (CR). As discussed in Section 5.2.2, the multiphonon relaxation rate is dependant on the phonon energy of the host glass. As silica is used as the Thulium host for the TDFAs designed in this thesis, the high phonon energy should result in frequency multiphonon transitions. The probability of CR transition is dependant on the doping density of Thulium in the fibre. As the

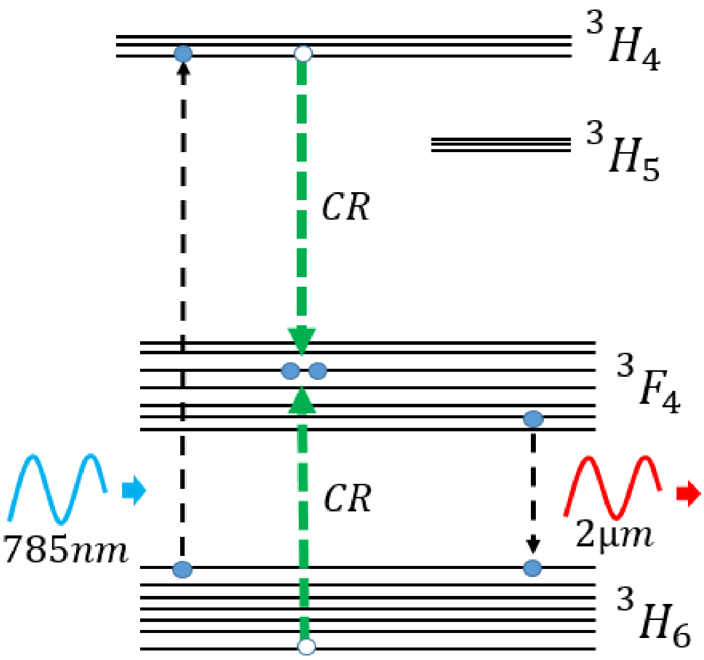

Figure 5.8: Energy level diagram of Thulium (Tm3+) pumped at 785 nm and undergoing cross relaxation allowing emission at 2 μm.

TDF used in this project was proprietary, the doping density was unknown. CR can be a very powerful process as it takes the energy of one photon at 785 nm and converts it into two excited electrons in the desired $^3F_4$ level, which can emit at 2 μm. The amplification potential of this pumping wavelength is dependant on the probability of the CR process occurring. If the probability of CR is low, the 785 nm pumping scheme will be inefficient, relying mostly on multiphonon transitions which are slower than the thermal in-band transitions preset in the 1550 nm pumping scheme. If CR probability is high, the high conversion efficiency of pump wavelength photons to electrons in the $^3F_4$ energy level should outperform in-band pumping schemes.

5.2.6 Amplified Spontaneous Emission

Amplified spontaneous emission (ASE) is produced when the spontaneous emission present in an excited gain medium is amplified through stimulated emission. In laser sources, ASE is suppressed by the optical mode the cavity is designed to support. As fibre amplifiers lack an optical cavity, ASE is only suppressed by the signal laser making a single pass through the fibre. This makes the ASE power dependant on the input signal laser power. This can result in low power input signals being lost below the noise floor generated by the ASE. As spontaneous emission generates photons with random phase and direction, ASE is produced in both directions in fibre amplifiers. Backward ASE, i.e. towards the laser source, can cause damage to the pump or signal laser if appropriate isolators are not used. Forward ASE, i.e. in the same direction as the signal, is a primary contributor to signal to noise ratio (SNR) reduction in fibre amplifiers. This reduction in SNR is described by a value called the noise figure (NF), which is the difference between the input signal and output signal SNR, measured in dB [162]. ASE can have relatively high optical power due to the length of the optical fibre (being of the order of meters) and the broad optical emission spectra of fibre amplifiers. The large fibre length allows for spontaneous emission to be amplified over a long period, accumulating power through stimulated emission. As the out-of-band ASE (i.e. outside the signal bandwidth) power can be quite high, an optical filter is often added to experimental setups to reduce the out-of-band optical power reaching the detector.

5.2.7 Gain in Fibre Amplifiers

The performance of an optical amplifier is based on its ability to produce optical gain at the signal wavelength. Gain is analogous to amplification and is described as the ratio of the input optical power to the output optical power, typically in dB. The amount of stimulated emission that can be achieved at the signal wavelength is dependant on many factors such as the pump power, signal power, amplified spontaneous emission power and the doped fibre length [163]. Figure 5.9 shows a basic design for a fibre amplifier. The amplifier consists of a pump laser (wavelength λ_2) and signal laser (wavelength λ_1) coupled together and sent through a strand of rare-earth ion

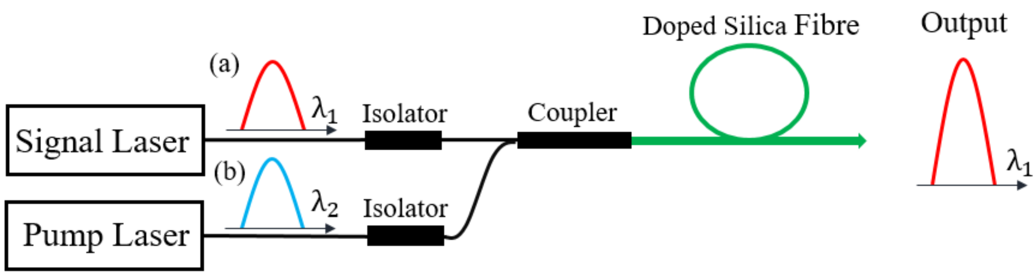

Figure 5.9: Diagram of a fibre amplifier showing: The signal laser output (a) is amplified after passing through the doped silica fibre which was excited using the light from the pump laser (b) where λ_2 is shorter than λ_1.

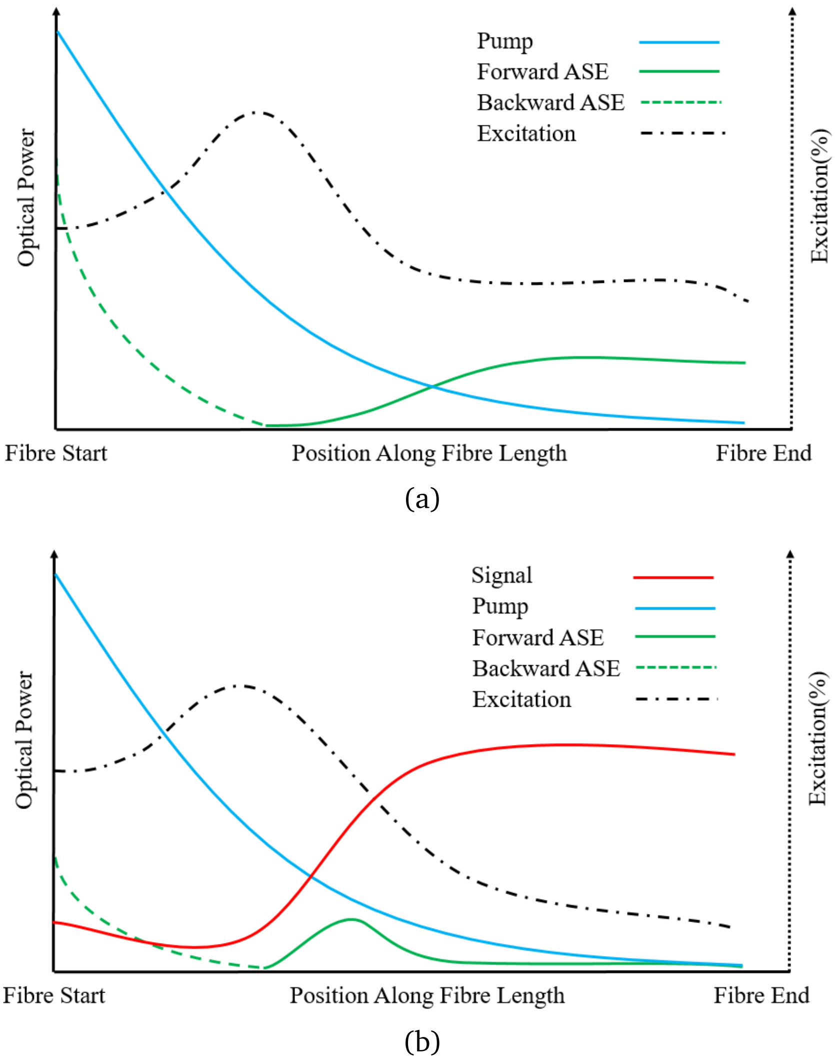

Figure 5.10: Qualitative description of optical power distribution and ion excitation in doped fibre amplifier (a) when no signal laser is present and (b) when a signal laser is present.

doped optical fibre. Figure 5.10(a) gives a qualitative description of the power distribution and ion excitation in a fibre amplifier, in the case where only the pump laser is present. The pump power is absorbed as it passes through the fibre, with the rate of absorption dependant on the ion absorption cross section at the pump wavelength. With no signal laser present, ASE is produced with relatively high power. ASE is produced in both directions in the optical fibre, with backward ASE typically having more power due to the higher excitation densities in the initial part of the fibre length. A minimum in the ASE power can be seen when the excitation density is at a maximum. Figure 5.10(b) introduces the signal laser to the amplifier, resulting in modified power distribution in the fibre. Over the length of the fibre, the signal wavelength stimulated emission achieves gain at a much faster rate than the ASE, resulting in a suppression of the ASE power and reduced excitation of the ions in the fibre. Eventually, the signal gain will saturate, achieving a state where signal wavelength loss and gain balance out. Modifying fibre length to target power distributions which are favourable for high amplification and low ASE power is a key part of fibre amplifier design.

5.3 Experimental Development of Thulium Doped Fibre Amplifiers

In this section we discuss the results obtained from the development and characterisation of TDFAs using a variety of pumping wavelengths and doped fibre lengths. When designing a fibre amplifier it may seem best to operate with high pump power to achieve maximum gain, as increased pump power leads to higher excited populations in the doped fibre resulting in more stimulated emissions. However, for amplification around 2 μm, this high power pumping regime may not be necessary to achieve large amplification in TDFAs. When operating at low pump powers, which are below the pump saturation power of an amplifier, many interesting effects begin to occur. Re-absorption of ASE is a key feature which was studied in an attempt to increase the amplification potential of TDFAs around 2 μm. In this thesis we looked at the effects of pumping at 1550 nm and 785 nm, exciting the Thulium using the $^3H_6 -^3 H_4$ and $^3H_6 -^3 F_4$ transitions respectively. The effects of pumping the optical fibre in one direction or two directions were studied using single and dual pump laser schemes. Mixed pumping regimes where 1550 nm and 785 nm pump lasers were used together were also studied.

5.3.1 Characterisation of Pump and Signal Lasers

Three lasers were used in the initial development of the TDFAs in this thesis; a 1550 nm pump, a 785 nm pump and a 1994 nm signal laser. The LI curves and optical spectra for these three lasers can be seen in Fig. 5.11. The pump lasers used for both the in-band pumping and indirect pumping schemes were multi-mode with a maximum average output power of 250 mW. Multi-mode lasers were selected as they offered a higher average optical power than their single-mode counterparts. The multi-mode nature of the light should not have a significant effect on the amplifier performance as all wavelengths present lie within the absorption regions of Tm3+, so the majority of the optical power should be used for excitation in the fibre. Note that the optical spectra for these lasers were captured on an OSA with 10 dB attenuation to prevent damage to the OSA. Figure 5.11c shows the characterisation of the signal laser operating at 1994 nm. This laser was the same MQW DM laser model as previously used for OFC generation in Chapters 2 through 4 [41]. As we were mainly interested in the small-signal amplification potential of TDFAs, the signal laser was operated between -10 dBm and -20 dBm for all gain characterisations.

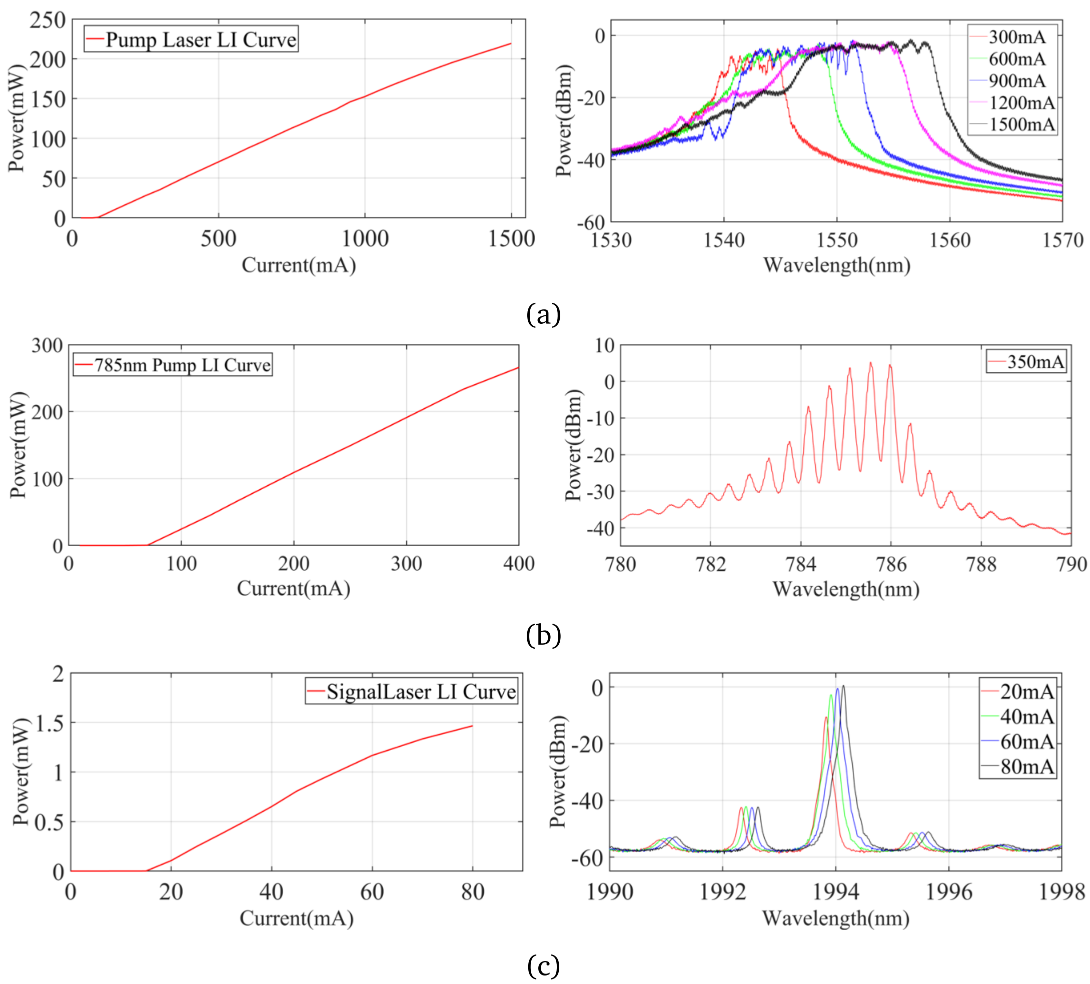

Figure 5.11: Optical Spectra and LI curves for (a) 1550 nm in-band pump laser (b) 785 nm indirect pump laser and (c) 1994 nm signal laser all operating at 25 °C.

5.3.2 TDFA Characterisation Using In-Band Pumping at 1550 nm

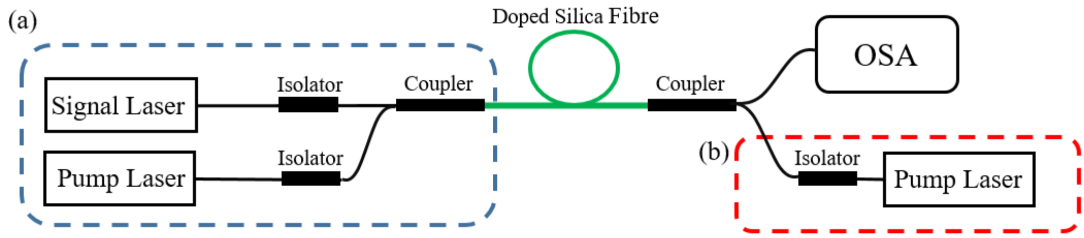

Figure 5.12: TDFA experimental setup where (a) shows the signal laser and forward pumping portion of the amplifier and (b) the backward pumping setup which was required for dual pumping.

When characterising the in-band pumping based TDFA we looked at a collection of optical spectra captured on an OSA. This could capture detailed spectra ranging from 1200 nm - 2400 nm, with a resolution of 6 GHz. Figure 5.12 shows the experimental setup used in the characterisation of the in-band pumped TDFA. A single pump setup and dual pump setup were tested. The dual pump setup allowed for increased pump power to be introduced to the fibre and also showed how pump light distribution through the fibre length could affect gain. This this was achieved by setting the net pump power to be equal for the single and dual pump case and monitoring the difference in the TDFAs output spectra in both cases. Isolators were placed in front of the pump and signal lasers to protect them from the ASE which propagates both forward and backward along the fibre. A specialised WDM coupler was used to combine the pump light at 1550 nm and signal light around 2 μm to reduce the losses at this junction. The optical signal loss at the coupler was measured to be 1.5 dB at 1.994 μm. The isolator loss was measured to be 1 dB at 1.994 μm. The doped optical fibre used for all amplifiers developed in this thesis was TmDF-200, supplied by OFS.

5.3.2.1 Single Pump Regime

For the characterisation of the in-band pumped TDFA, spectra were collected for varying lengths of Thulium doped fibre and a range of optical pump powers. These parameters were varied as they are primary contributors to the gain and spectral properties of fibre amplifiers. Figure 5.13 shows a collection of TDFA emission spectra for increasing pump power. The large spectral peaks seen in Fig. 5.13 show the amplified optical signal after passing through the

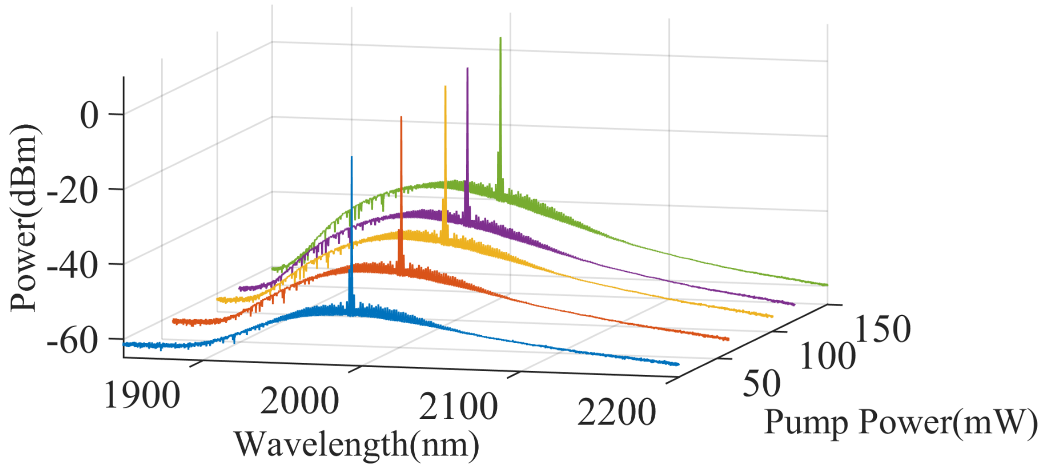

Figure 5.13: Optical spectra collected from TDFA with increasing pump power including the signal at 1994 nm and the broad ASE spectrum spanning from 1850 nm to 2200 nm.

fibre amplifier. Through comparing these output spectra and the spectra of the optical signal prior to amplification, gain and noise figure were calculated. Gain measures the increase in optical power of the signal laser in dB and the noise figure measures the reduction in optical signal to noise ratio (OSNR) in dB after the signal passes through the fibre amplifier. Surrounding the signal peaks, broad spectra are shown. These are the ASE profiles of the fibre amplifier. Information about the energy level populations and energy distribution can also be inferred when looking at the full ASE spectrum shown in Fig. 5.13. Processes such as re-absorption of spontaneous emissions and parasitic lasing can be seen by looking at the changing profile of the ASE spectrum, helping to explain some of the variations in optical gain in different TDFA configurations.

Fig. 5.14 shows the gain and noise figure measured for three doped fibre lengths with increasing optical pump power in the single 1550 nm pump regime. The gain was achieved with a signal launch power of -10 dBm. The OSNR of the signal laser at peak power -10 dBm was 45 dB. The maximum gain was achieved with the 6 m fibre and a pump power of 23.4 dBm. The peak gain for each fibre length was measured to be 13.4 dB for the 6 m fibre, 13 dB for the 4 m fibre and 11.9 dB for the 2 m fibre. The noise figure in all cases was around 5 dB, with very little variation, approximately 0.5 dB. Although the maximum gain was achieved using the 6 m fibre, it can be seen

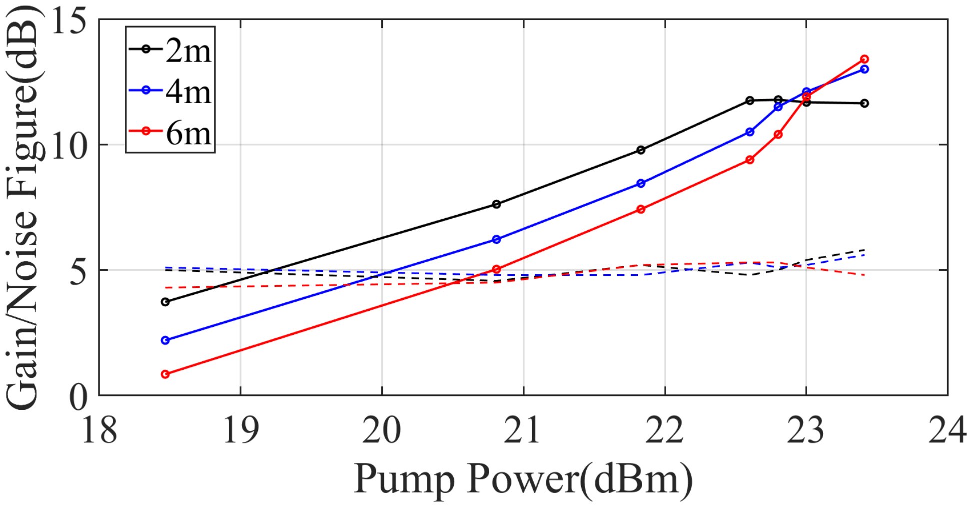

Figure 5.14: Gain (solid line) and noise figure (dashed line) for three fibre lengths pumped with a single pump at 1550 nm with increasing pump power.

that as pump power decreases, higher gain is achieved using shorter fibre. To explain this variation in gain, we looked at the ASE spectra for a case with minimum pump power and a case with maximum pump power in more detail.

Figure 5.15 shows the spectra obtained at the three fibre lengths with pump power of 18.5 dBm. The overall spectral power is low in this case, with all ASE wavelengths below -40 dBm and signal power around the unamplified value of -10 dBm, indicating little to no optical gain. In this case the amplification achieved by the 2 m fibre is just enough to overcome the inherent loss in the doped optical fibre at 1994 nm. As the fibre length is increased these inherent losses are also increased, reducing the gain in the 4 m and 6 m fibre pumped at 18.5 dBm. It is important to note the difference between these intrinsic losses and the losses at shorter wavelengths, from 1850 nm and 1950 nm. The losses seen around 2 μm are a product of typical optical fibre loss mechanisms. The losses which occur between 1850 nm and 1950 nm are more drastic in comparison, as seen in Fig. 5.15. The reduction in optical power at these wavelengths is caused by re-absorption due to the presence of unexcited Thulium in the doped fibre. As the signal wavelength of 1994 nm is outside the absorption cross section of Thulium, it is not subject to these large losses at low pump power and, as we will show later, can actually benefit from this re-absorption process. With the very low pump power used in Fig. 5.15, much of the Thulium is left unexcited in the optical fibre allowing for spontaneous emission to be absorbed multiple times as it passes through the fibre. Each

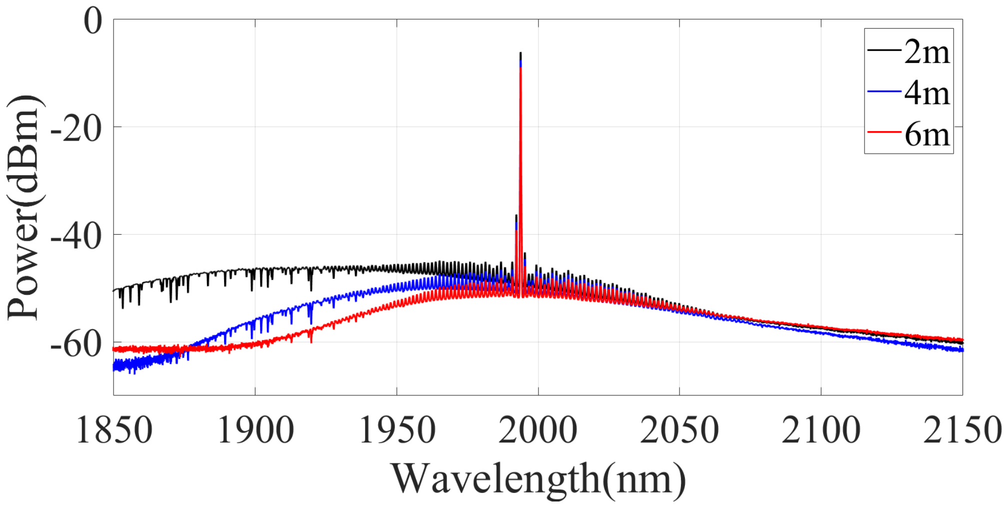

Figure 5.15: Optical spectra for TDFAs with varying fibre length pumped with 18.5 dBm at 1550 nm.

time the shorter wavelength photons are re-absorbed they lose some of their energy due to thermalisation, causing subsequent emission at longer wavelengths. This creates a wavelength shift of the optical gain spectrum.

Fig. 5.16 shows the spectra obtained from the three lengths of fibre with increased optical pump power of 23.4 dBm. Similar to the low pump power case, re-absorption at lower wavelengths can be seen to increase with fibre length. However, in this case, the increase in pump power generates a higher density of excited electrons in the fibre, allowing for increased amplification at the signal wavelength. With 23.4 dBm pump power, the 2 m fibre achieved saturation of its potential amplification. This prevented re-absorption of longer wavelengths and produced an ASE spectrum peaking around -20 dBm. The discrete peaks present are a parasitic lasing effect, likely caused by some reflections at the fibre end facets. For the 4 m and 6 m fibre the concentration of unexcited Thulium in the amplifier was increased, as the fibres were not saturated by the pump power, allowing for re-absorption of ASE from the 1850 nm to 1900 nm region. The re-absorbed light resulted in an increase in amplification of longer wavelengths around 2 μm. In the absence of re-absorption, it would be expected that the gain would be reduced for longer fibre lengths as the intrinsic fibre loss would increase and the excitation density in the fibre would decrease. The results in Fig. 5.16 show that operating these fibre amplifiers below pump saturation can give rise to an increase in gain at longer wavelengths due to the re-absorption of ASE.

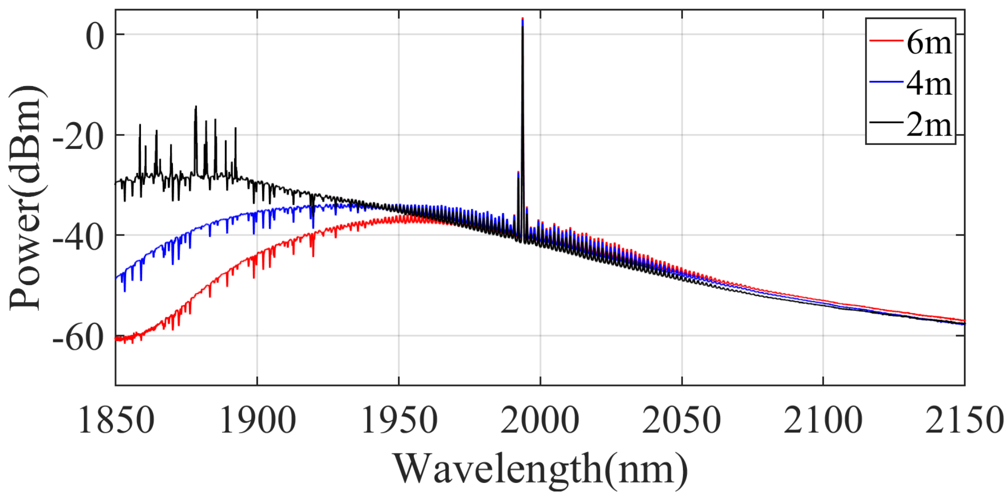

Figure 5.16: Optical spectra for TDFAs with varying fibre length pumped with 23.4 dBm at 1550 nm.

5.3.2.2 Dual Pump Regime

In the previous section, a single pump laser was used to excite lengths of doped optical fibre ranging from 2 m to 6 m. It was seen that with maximum pump power, the gain of the 6 m fibre was increasing linearly, i.e. pump saturation was not achieved. In this section a second pump laser was introduced to increase the amplifier pump power beyond that achievable by a single pump laser, see Fig. 5.12. For this setup, an additional pump laser, of the same model as the first, was used to pump the fibre counter-propagating with the signal beam. This allowed for the optical pump power supplied to the doped fibre to be effectively doubled. The same characterisation process was carried out as in the previous section, analysing several spectra to measure the gain, noise figure and ASE distribution. Figure 5.17 shows the gain and noise figure comparison for the dual pumped and single pumped 6 m TDFAs with increasing pump power. The linear gain increase with pump power continued for the dual pump setup, with a maximum gain of 18.5 dB achieved with a total pump power of 26.4 dBm. This linear increase shows that there is still no pump saturation present at this pump power. Although the added optical power does produce an increase in the gain, it can be seen that the gain achieved in the single pump regime is higher at the same pump power values. As the net optical power introduced to the laser in both cases is the same for values between 21.5 dBm and 23.4 dBm, the key difference is the distribution of the pump power along the fibre. In the case of the single pump, the pump light is absorbed towards the beginning of the fibre then undergoes the

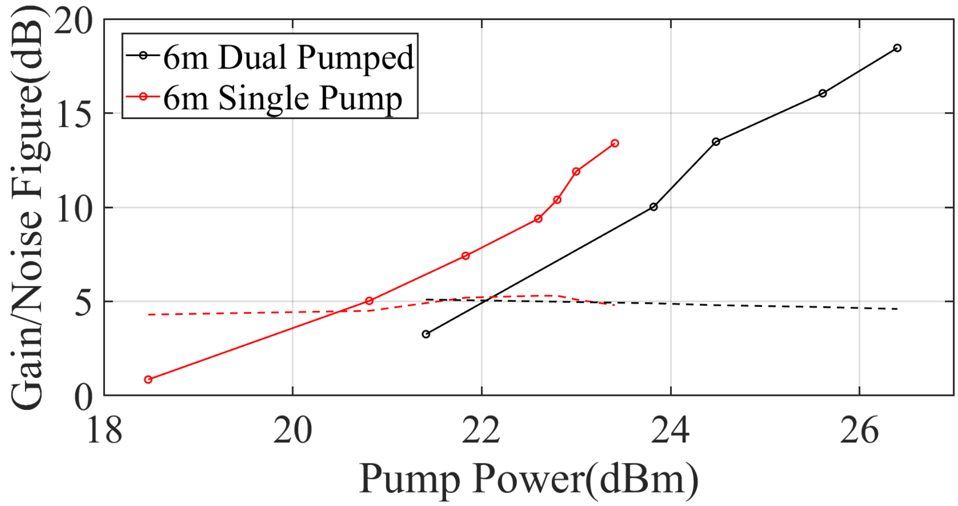

Figure 5.17: Gain and noise figure achieved for dual and single pump TDFAs with 6 m fibre length and 1550 nm pump wavelength.

re-emission and absorption process along the fibre by interacting with the unexcited Thulium which is concentrated towards the end of the fibre. The dual pump setup creates a more even distribution of pump power through the doped fibre, with both ends of the fibre populated with excited Thulium, leaving the middle of the fibre length as the region where most of the re-emission and absorption takes place. Figure 5.18 shows how the distribution of the pump light in the dual pumped setup prevented the more extreme re-emission and absorption seen in the single pump case. In the dual pump setup, emissions between 1850 nm and 1900 nm are more prominent,

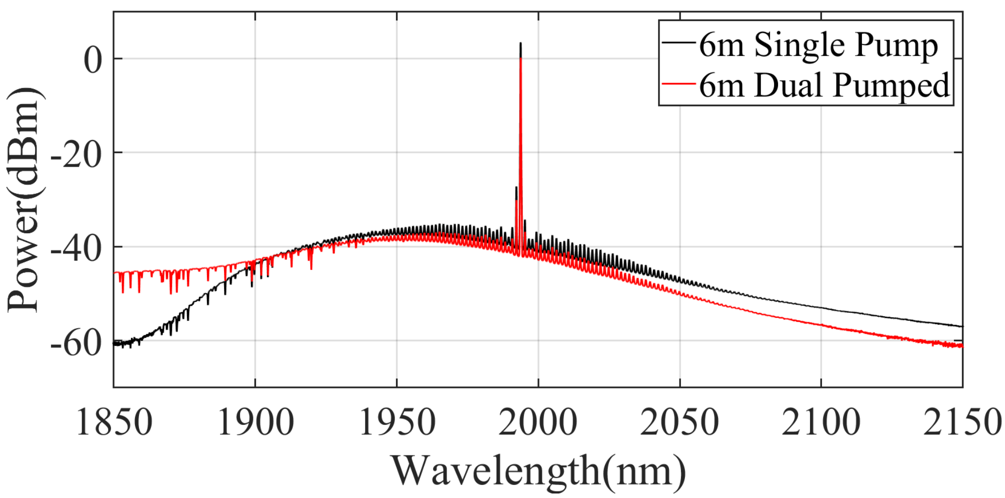

Figure 5.18: Optical spectra for TDFA pumped with a net power of 23 dB in a single and dual pump regime.

with peak power around -45 dBm. This reduces the availability of excited Thulium which can emit at the signal wavelength. The single pump setup produces a spectrum where the optical powers are effectively shifted to longer wavelengths, showing the effectiveness of the re-absorption process for amplification at 1994 nm. Eventually the increased pump power produces higher gains than the single pump, but is less efficient for amplification at longer wavelengths due to the pump light distribution reducing the effective re-absorption of ASE in the fibre.

5.3.3 TDFA Characterisation Using Indirect Pumping at 785 nm

An alternative to the in-band amplifier pumping schemes shown in the previous section are indirect pumping schemes, as described in Section 5.2.5. This section discusses the characterisation of a TDFA which was pumped using an indirect pumping scheme at 785 nm, with a single pump laser. The excitation of the Thulium in this pump regime relies on the process described in Section 5.2.5, where a non-radiative cross relaxation process is required to populate the $^3F_4$ energy level, which can then emit at the desired wavelength around 2 μm. The cross relaxation process converts the energy of a single photon into two excited electrons in the $^3F_4$ energy band. This theoretically offers a much higher efficiency when compared to the in-band pumping at 1550 nm. However, this process is dependant on the population density of the $^3H_4$ energy level, requiring a high population density to keep the probability of cross relaxation high. With the absorption cross section of Tm3+ at 785 nm being more than three times that of the cross section at 1550 nm, the 785 nm pump light is absorbed rapidly in the doped fibre. Rapid absorption leads to a very dense excited population at the beginning of the fibre which can benefit amplification in short fibre strands but, as the fibre length increases, the reduced excited population density towards the end of the fibre brings drawbacks to amplification.

Figure 5.19 shows the gain and noise figure achieved with a 785 nm and 1550 nm pumped TDFA, with signal wavelength of 1994 nm and signal power of -20 dBm. Both amplifiers were pumped in the forward direction with the laser sources shown in Fig. 5.11. Both pump wavelengths had an optical power of 23 dBm. In this experiment the optical fibre length was varied from 0.5 m to 3

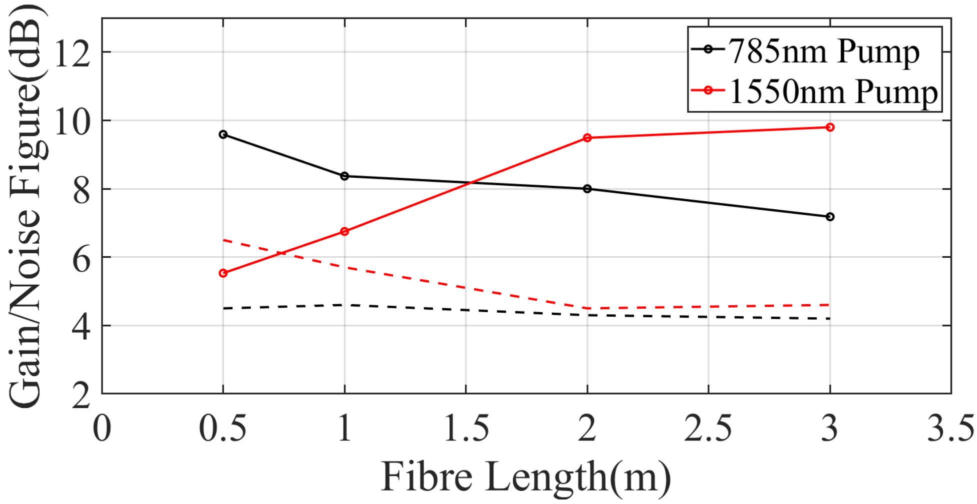

Figure 5.19: Optical gain and noise figure achieved for TDFA pumped with 1550 nm and 785 nm light at 23 dBm for increasing fibre length.

m, instead of the 6 m of the in-band pumping characterisation. This was done as the rapid absorption of pump light at 785 nm made shorter fibres a more efficient choice to achieve maximum gain. Figure 5.19 clearly shows that the indirect pumping scheme produces larger gain for shorter lengths of doped fibre, but unlike the in-band pumping scheme, the gain is reduced as the fibre length is increased. The opposite was shown to be true for the 1550 nm pump regime, where the gain increased as the fibre length was increased. The maximum gain achieved for the 785 nm pump was 9.59 dB with 0.5 m of Thulium doped fibre. The maximum gain achieved with the 1550 nm pump was 9.8 dB with 3 m of Thulium doped fibre. The noise figure for the indirect pumping scheme remained low for all fibre lengths, approximately 4.5 dB with little variation. For the in band pumping scheme the noise figure had a much larger value of 6.4 dB for 0.5 m of fibre, which reduced as the fibre length increased to approximately 4.6 dB. With the low amplification of the signal wavelength in this configuration, there was little suppression of the ASE around the signal wavelength, causing the increased noise figure values.

Figure 5.20 shows the spectra obtained for both pumping schemes for the 0.5 m and 3 m fibre setups. Figure 5.20a shows the 0.5 m fibre spectra, with very broad ASE emission in both cases, spanning from 1700 nm to 2150 nm. As there are relatively large ASE powers between 1700 nm and 1800 nm, we can say there is little re-absorption occurring in such short fibre. With re-absorption minimised, the 785 nm pump produces a greater population density in the emission band when compared to the 1550 nm, leading to larger gain for the indirect pumping setup. The much lower absorption cross section at 1550 nm reduces the rate at which the pump light at this wavelength is absorbed, requiring a longer fibre length in order to generate a large population inversion between the ground and excited state of the Tm3+. When the fibre length is increased the re-absorption process starts to dominate, reducing the output power in the 1700 nm to 1800 nm region for both pumping schemes. As expected for the 1550 nm case, the re-absorption leads to increased gain for longer wavelengths as shown in Section 5.3.2. However, for the 785 nm pumped TDFA the re-absorption process is less efficient in populating the emission band for longer wavelength emission, leading to reduced gain and ASE as seen in Fig. 5.20b. The rapid absorption of the pump

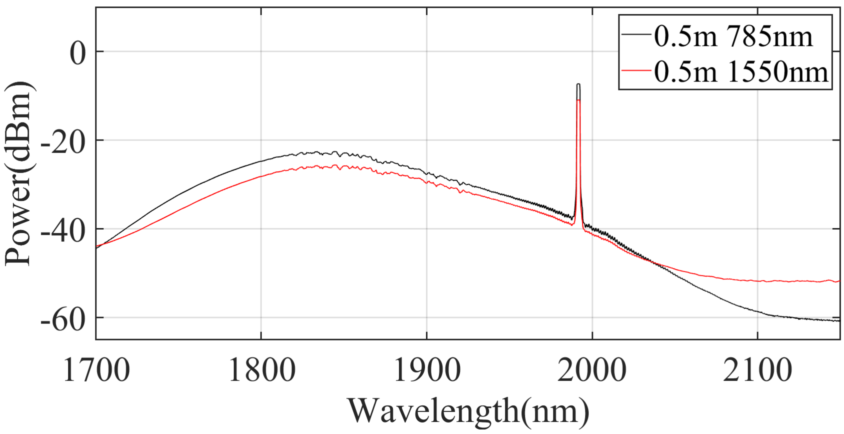

(a)

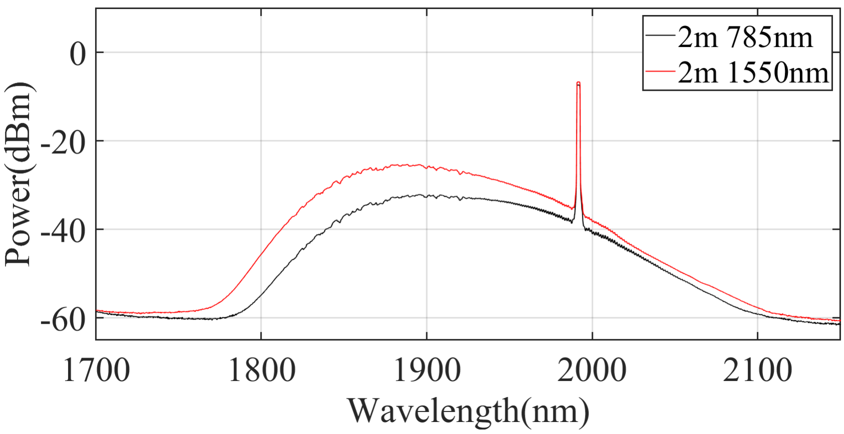

(b)

Figure 5.20: Optical Spectra including ASE for TDFAs of length (a) 0.5 m and (b) 2 m pumped at 1550 nm and 785 nm.

light at 785 nm hinders the amplification potential for longer fibres as there is a very short region at the beginning of the fibre which has a population density in the emission band large enough to produce amplification. With the much lower excited population densities further along the fibre, processes such as cross relaxation and electron transition to the emission band occur less often. For this reason, the 785 nm pump is limited in its potential as a TDFA pumping scheme, particularly when the pump power is not high enough to cause pump saturation in the fibre.

5.3.4 Mixed Wavelength Pumping at 1550 nm and 785 nm

In the previous two sections the potential of 1550 nm and 785 nm pumping schemes for TDFAs were studied, showing benefits and weaknesses in both cases. Pumping at 1550 nm showed the potential for re-absorption to increase gain at longer wavelengths and the 785 nm pumping scheme showed increased gain in very short doped fibres due to Thulium's increased absorption cross section at this wavelength. With these key properties in mind we developed a dual pump TDFA using both pump wavelengths to achieve a short efficient amplifier for longer wavelengths in the Thulium emission spectrum around 2 μm. For this experiment TDFAs with optical fibre lengths starting at 0.5 nm were tested using 23 dBm of pump power at 1550 nm and 23 dBm of pump power at 785 nm. The signal power again was set to -20 dBm to test the small signal amplification potential of the amplifier. To focus on the effects of re-absorption on gain at different wavelengths, three different signal wavelengths were used in this experiment. The three wavelengths used were 1876 nm, 1994 nm and 2045 nm, as shown in Fig. 5.21b. As the optical pump power may have been high enough to saturate the fibre in these TDFAs, we first collected the ASE spectra for five fibre lengths to look for the characteristic reduction in optical power between 1700 nm and 1800 nm. Figure 5.21a shows that, as the fibre length is increased, the re-absorption is seen to occur at these lower wavelengths and increases the ASE power at longer wavelengths, with the exception of the 2.5 m fibre. From the 0.5 m to 2.5 m fibre the ASE peak wavelength was shifted by approximately 50 nm. In the 2.5 m fibre a distinct drop off in ASE power at longer wavelengths can be seen from 2000 nm to 2100 nm. In this case, the re-absorption process is still seen as the peak wavelength shift continues towards longer wavelengths, but the reduction in excited state population density clearly reduces the emissions

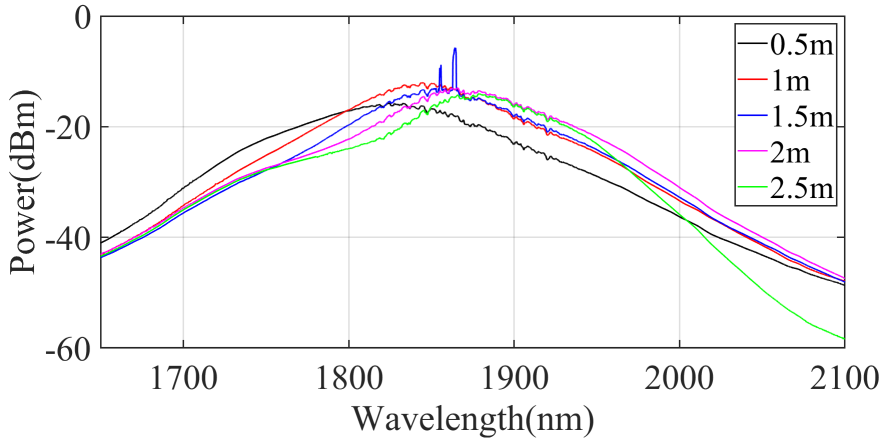

(a)

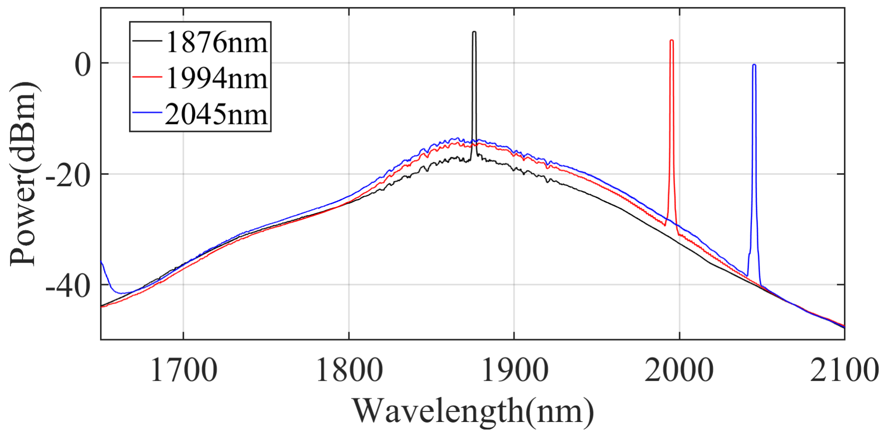

(b)

Figure 5.21: Optical spectra for (a) ASE for increasing fibre length pumped with a dual pumping scheme consisting of a 1550 nm and 785 nm laser both operating at 23 dBm (b) Signal at 1876 nm, 1994 nm and 2045 nm amplified through 2 m of TDF.

beyond 2000 nm. The longer wavelengths are affected more as they are the least optically excited, and have the lowest emission cross section. The effects of having a low emission cross section are also shown in Fig. 5.21b. The three signal wavelengths display different amounts of ASE suppression, with the maximum suppression seen at 1876 nm and the minimum at 2045 nm. When excitation density in the TDFA starts to decline, as in the case in the 2.5 m fibre, the low emission cross section of longer wavelengths prevents them from drawing emissions away from the shorter wavelengths where the emission cross sections are higher.

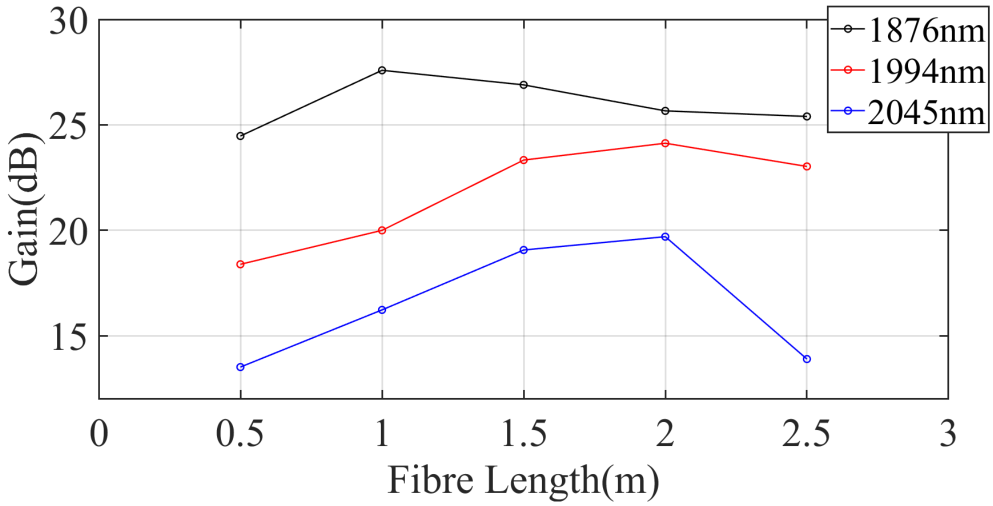

Figure 5.22: Gain achieved at 1876 nm, 1994 nm and 2045 nm for increasing Thulium doped fibre length.

Figure 5.22 shows how the shifting ASE translates into gain at the three tested wavelengths. Through increase of fibre length alone, a gain increase of 34% was achieved at 1994 nm from 18.3 dB at 0.5 m to 24.5 dB at 2 m. This came at a small cost to the amplification at 1876 nm, which saw a 7% reduction in its amplification between 1 m and 2 m. This comparatively small reduction in gain, compared to the increase at 1994 nm, confirms that the majority of the additional gain is coming from wavelengths far below 1876 nm. At 2045 nm a 46% gain increase from 13.5 dB at 0.5 m to 19.7 dB at 2 m was measured. As implied by the ASE spectra in Fig. 5.21a, a sharp falloff in gain is seen in the 2.5 m fibre for the 2045 nm signal. This shows that the emission cross section and excited state density play a key role when designing the TDFAs operating below pump saturation levels. Once the excited state density is reduced past a certain point, the re-absorption effects cannot increase the gains achieved at longer wavelength in the TDFAs. The 2 m fibre length was the optimal length used as increasing beyond this point saw stagnation in gain increase for the 1876 nm and 1994 nm signal, and large gain reduction for the 2045 nm signal.

5.4 Summary

In this chapter the fundamental principles governing amplification through doped fibre amplifiers were discussed. The potential of Thulium ($Tm3+$) as a rare-earth dopant enabling amplification in the 2 μm wavelength region was described and tested. Through variation in pumping regimes and fibre length a TDFA pumped below saturation level was shown to achieve high gain around 2 μm. The effects of in-band and indirect pumping were studied and the effects of pump power distribution using dual pumping regimes was shown. These amplifiers were the first to show the potential of re-absorption of ASE to increase emissions at longer wavelengths in Thulium's emission band. Through length optimisation, gains as high as 24.5 dB were achieved around 2 μm, using 500 mW of mixed wavelength pump power and 2 m of doped fibre. The development of a low pump power TDFA, optimised for amplification around 2 μm, helped enable the development and testing of the OFCs and DFCs shown in this thesis.

Chapter 6

Conclusion

In this chapter, the results presented in this thesis are summarised. Potential avenues for future research are discussed and the thesis is concluded.

6.1 Overview of Results Presented

Chapter 2 focused on the potential for optical frequency comb generation in the 2 μm wavelength region. The current state of the art for OFC generation at 2 μm, Thulium fibre oscillators and GaSb QCLs were discussed. The advantages and disadvantages of each device were shown and the potential benefits of a gain switched semiconductor laser solution was given. A variety of applications that could benefit from the development of a compact OFC source operating in the 2 μm were discussed. These applications included optical communications, integrated silicon photonics, medical sensing and molecular spectroscopy. Through improved strain management between the quantum well structures and the InP platform the devices were grown on, an InGaAs MQW DM laser source was developed, with stable laser emission in the 2 μm wavelength region. Using laser gain switching as a pulse generation method, the project set out to demonstrate a small scale, simplistic and integrable OFC source operating around 2 μm. Through numerical simulation of the laser rate equations, it was shown that three key modulation regimes could arise under reasonable gain switching conditions of the laser sources. In the case where the modulation amplitude caused the laser to switch below the lasing threshold, increased phase noise between pulses induced by spontaneous emission prevented the generation of an OFC. Increasing the frequency of the modulation beyond the laser relaxation frequency resulted in a period-doubling regime, where the phase noise between pulses was reduced and an OFC was generated. Lastly, in the regime where the laser was modulated above lasing threshold, i.e. the laser was not switched off, OFCs were generated with frequency spacing equal to the modulation frequency. The optimal OFCs were found to be generated in modulation regimes where the sinusoidal current had a minimum near laser threshold and a frequency around the laser relaxation oscillation frequency. The simulations predicted the 2 μm laser sources, when biased at 30 mA, could produce an OFC with frequency spacing of 3 GHz spanning approximately 100 GHz, with a 60 GHz spectrally flat region.

In Chapter 3, OFC generation using gain switched InGaAs MWQ DM lasers was achieved at 2 μm. Due to the lack of available high-resolution OSAs in the 2 μm wavelength region, a swept heterodyne beating technique was employed to characterise the frequency comb in the electrical domain. Through this method, the OFC generation regimes predicted by the numerical simulations were verified. Gain switching at 3 GHz with 8 dBm modulation amplitudes, resulted in an OFC being generated with 70 GHz bandwidth and 19 comb lines in a spectral region with 10 dB flatness. With the limiting factor for bandwidth expansion of the frequency combs being the loss of pulse-to-pulse coherence at large modulation amplitudes, optical injection locking was used to restore coherence between the pulses in this scenario. Through OIL, it was found that the lasers could be modulated at 17 dBm while maintaining the coherence required to generate an OFC. Injecting with -8 dBm and modulating at 3 GHz with 17 dBm amplitude, an OFC was generated spanning 103 GHz with 29 comb lines in a spectral region with 10 dB flatness.

Chapter 4 covered the use of the OFC generators, demonstrated in Chapter 3, in a dual frequency comb architecture. In this chapter, some of the most popular methods of spectroscopy were described. Through this, it was shown that there is a gap in the field for a system that is compact and simple with fast acquisition times. A DFC system, based on gain switched lasers, was shown to have the potential to satisfy these conditions. Using mutually injection locked gain switched lasers, a DFC was generated in the 2 μm wavelength region. Through careful selection of the injection wavelength, minimising the beating symmetry around the injected wavelength, a DFC was generated with 49 beating tones and comb line spacing of 2 GHz. Due to symmetry interference, 6 of these comb lines would not be usable in sensing applications. By reducing the difference in modulation frequency between the OFCs to 300 kHz, the DFC could be detected in a 15 MHz bandwidth with a total integration time of 50 ms resulting in a beat tone SNR of 25.6 dB.

Chapter 5 covered the development of a Thulium doped fibre amplifier for the 2 μm wavelength region. Throughout the experiments in this project, a TDFA was required to restore optical power lost through the various OFC systems. With the aim of restoring optical loss, this portion of the project was focused on designing a TDFA that could utilise low pump power to achieve gain optimised for wavelengths near 2 μm. Through experimental analysis of different TDFA pumping regimes, it was found that pumping the TDFA below the pump saturation level, allowed for re-absorption of some spontaneous emission between 1650 nm and 1850 nm. Through this process of re-absorption, the potential gain from wavelengths beyond 1850 nm was increased. Using a 2 m TDF pumped with 785 nm and 1550 nm lasers, each with 23 dBm of optical power, a TDFA with 24.5 dB gain at 1994 nm was produced.

6.2 Future Work

With the 2 μm comb sources developed in this project showing promise for the fast and simple acquisition of spectroscopic information, the first avenue for future work would be to use these devices for CO_2 detection. As mentioned earlier, CO_2 is one of the primary gases which can be detected at 2 μm. To get a sense of the real-world feasibility of the OFCs and DFCs developed in this thesis, the detection sensitivity and integration times required for CO_2 sensing could be studied using a simple single-pass absorption cell method [128, 126]. The sources could also be used in a cavity-enhanced spectrometer, offering increased detection sensitivity [164]. Cavity-enhanced spectroscopy uses a high finesse absorption cell to reflect the OFC light for several cavity round trips, before exiting the cavity to a detector. This increases the effective path length of the absorption cell, which enhances the overall sensitivity of the spectrometer [165, 166].

The benefit of developing a comb source based on semiconductor lasers and a comb detection scheme that requires no moving parts is the potential for integration on a PIC [167, 109, 168]. The design and realisation of a DFC PIC, based on the gain switched 2 μm lasers shown in this project, would have several challenges to overcome. Firstly, the DFC setup used in this thesis would require miniaturisation of some components. As the TDFA used for amplification throughout this thesis is not integrable, a semiconductor optical amplifier (SOA) serving the same purpose would be required. An SOA in the 2 μm wavelength region has recently been developed and integrated on a silicon platform, showing gain comparable to that required by the proposed 2 μm DFC [169, 170]. The SOAs were designed from similar semiconductor materials as the gain switched laser sources shown in this thesis and were grown on an InP platform. Due to the years of research studying approaches to integrate InP on silicon, the DFC in this thesis could also see full integration onto a silicon platform [171, 172, 173]. This would be an ideal case, enabling the mass implementation of these sources in applications such as distributed sensing in smart cities [174, 175].

The primary drawback of gain switched lasers is the low optical bandwidth of the OFCs they produce. In this thesis, OFCs spanning approximately 100 GHz were generated with the aid of optical injection. To expand these OFCs many approaches could be taken. Mach-Zehnder modulators (MZMs) have been implemented as gain switched OFC expansion tools in the past [176]. By passing an OFC through a dual-drive MZM, which is modulated at a frequency multiple of the OFC frequency spacing, the comb can be replicated at the MZM repetition frequencies. This results in a bandwidth expansion and improved spectral flatness for the gain switched OFC. With the recent development of high-speed silicon MZMs at 2μm, photonic integration could remain possible with this expansion method [177]. Another method that can be used to enhance OFC spectral bandwidth is to phase correlate a group of gain switched lasers. This process of phase-locking several OFCs to generate one large OFC has been demonstrated using two gain switched lasers [178]. By using four-wave mixing phase transfer in a saturated semiconductor optical amplifier (SOA), the uncorrelated OFCs entering the SOA leave with the same optical phase. This method of comb expansion offers flexibility in the number of OFC sources used but becomes an expensive architecture as the number of lasers required increases.

More recently, the potential of dissipative Kerr soliton (DKSs) microresonators combined with gain switched OFCs has started to be explored. The research for this particular technology is in an early phase but have potential to enable integrated comb expansion on silicon platforms. DKS microresonators offer octave-spanning frequency combs, which enable application in precise metrology due to their ability to self-reference [179]. Self-referencing is a process used to recover the carrier-envelope offset of an OFC, allowing for the absolute frequency of the OFC tones to be known [59, 180]. One drawback of OFC generation with microresonators is the large frequency spacing they produce, typically around 100 GHz. Particularly for gas sensing applications, OFC frequency spacing in the low gigahertz to megahertz range is desirable. Through combining the low-frequency spacing achieved with gain switched lasers and the octave-spanning bandwidth provided by microresonators, new OFC technologies have been developed which are starting to utilise the benefits of both of these technologies in combination [181, 84]. If these technologies could be implemented in the 2 μm wavelength range using the gain switched lasers shown in this thesis and microresonators designed for this wavelength region, they would prove to be a very powerful sensing tool for many applications.

6.3 Conclusion

Developing optical technologies in the 2 μm wavelength region has the potential to enable a variety of research and commercial applications. High capacity optical communications, nonlinear silicon photonics and molecular spectroscopy are three fields that would benefit from the development of 2 μm photonic devices. Molecular spectroscopy in this wavelength region is of particular interest as it can be used to detect key gases such as carbon dioxide, ammonia and water vapour. The ability to detect these gases enables critical applications such as air quality measurements, industrial process monitoring and non-invasive medical sensing. Optical frequency combs (OFCs) are one of the most powerful and versatile photonics technologies for sensing applications, being used for molecular sensing, distance ranging and velocity measurement, to name a few. Development of OFCs in the 2 μm wavelength region takes advantage of the broad potential for both OFCs and 2 μm photonic technologies. One of the primary drawbacks for current OFCs is the bulky size, high complexity and high cost of current OFC sources.

The work in this thesis established a 2 μm OFC source which was small scale, low complexity and relatively low cost; tackling some of the key issues preventing implementation of OFCs outside of a laboratory setting. Using recently developed low threshold semiconductor lasers and gain switching, OFC sources with 100 GHz optical bandwidths and narrow free spectral range were demonstrated with the aid of optical injection. Given the desired application of gas sensing, the OFC sources were demonstrated in a simple DFC architecture. The DFC demonstration provided insight into the potential future performance of the OFC sources developed. The primary achievements were millisecond acquisition time of spectra spanning 100 GHz and RF signal SNR in excess of 25 dB. With the device power requirements, footprint and complexity approaching a state where commercial implementation may be feasible, the next stage of this work will likely need to focus on bandwidth expansion of the OFC sources and device integration. The approach to tackling these two areas will likely involve silicon photonics, with comb expansion enabled by nonlinear or resonator elements and integration on an SOI platform leading to potential low-cost CMOS compatible photonic devices.

The ability to extract information from an environment is invaluable in many aspects of research and industry, from city planning and environmental monitoring to cutting edge measurements leading to fundamental physical insights. OFCs have proven to be an invaluable tool that could become more ubiquitous if the right criteria are met with regards to operating wavelength, cost, size and complexity. Through the work in this thesis, an OFC source operating in the 2 μm wavelength region was demonstrated in a DFC architecture. The devices developed could contribute to the progression of OFC implementation in many vital fields including research, industrial and public settings.

References

[1] T. H. Maiman, “Stimulated Optical Radiation in Ruby,” *Nature*, vol. 187, no. 4736, pp. 493–494, 1960.

[2] R. N. Hall, G. Fenner, J. D. Kingsley, T. J. Soltys, and R. O. Carlson, “Coherent Light Emission From GaAs Junctions,” *Phys. Rev. Lett.*, vol. 9, no. 366, 1662.

[3] Z. e. a. Alferov, “Effect of heterostructure parameters on the laser threshold current and the realization of continuous generation at room temperature,” *Fiz. Tekh. Poluprovodn*, vol. 4, pp. 1826–1829, 1970.

[4] W. C. Barnett, H. Takahira, C. Baron, and Y. Ogi, “The TPC-5 Cable Network,” *IEEE Communications Magazine*, vol. 34, no. 2, pp. 36–40, 1996.

[5] l. G. P. Agrawa, “Optical Communication: Its History and Recent Progress,” in *Optics in Our Time*, Springer, 2016.

[6] F. Gunning, N. Kavanagh, E. Russell, R. Sheehan, J. O’Callaghan, and B. Corbett, “Key enabling technologies for optical communications at 2000 nm,” *Applied Optics*, vol. 57, no. 22, 2018.

[7] F. Gunning and B. Corbett, “Time to Open the 2-μm Window?,” *Optics & Photonics News*, vol. 30, no. 3, pp. 42–47, 2019.

[8] T. Miya, Y. Terunuma, T. Hosaka, and T. Miyashita, “Ultimate low-loss single-mode fibre at 1.55 μm,” *Electronics Letters*, vol. 15, no. 4, pp. 106–108, 1979.

[9] D. J. Richardson, “Filling the Light Pipe,” *Science*, pp. 327–328, 2010.

[10] C. E. Shannon, “A mathematical theory of communication,” *The Bell system technical journal*, vol. 27, no. 3, pp. 379–423, 1948.

[11] B. J. Mangan, L. Farr, A. Langford, P. J. Roberts, D. P. Williams, F. Couny, M. Lawman, M. Mason, S. Coupland, R. Flea, H. Sabert, T. A. Birks, J. C. Knight, and P. S. J. Russell, "Low loss (1.7 dB/km) hollow core photonic bandgap fiber," in *Optical Fiber Communication Conference, Technical Digest (CD) (Optical Society of America), paper PD24.*, 2004.

[12] M. N. Petrovich, F. Poletti, A. van Brakel, and D. J. Richardson, "Robustly single mode hollow core photonic bandgap fiber," *Optics Express*, vol. 16, pp. 4337–4346, 2008.

[13] M. E. Lines, " Scattering losses in optic fiber materials. I. A new parametrization," *Journal of Applied Physics*, vol. 55, pp. 4052–4057, 1984.

[14] H. Zhang, N. Kavanagh, Z. Li, J. Zhao, N. Ye, Y. Chen, N. Wheeler, J. Wooler, J. Hayes, S. Sandoghchi, F. Poletti, M. Petrovich, S. Alam, R. Phelan, J. O'Carroll, B. Kelly, L. Grüner-Nielsen, D. Richardson, B. Corbett, and F. Garcia Gunning, "100 Gbit/s WDM transmission at 2 μm: Transmission studies in both low-loss hollow core photonic bandgap fiber and solid core fiber," *Optics Express*, vol. 23, no. 4, 2015.

[15] M. U. Sadiq, H. Zhang, J. O'Callaghan, B. Roycroft, N. Kavanagh, K. Thomas, A. Gocalinska, Y. Chen, T. Bradley, J. R. Hayes, Z. Li, S. U. Alam, F. Poletti, M. N. Petrovich, D. J. Richardson, E. Pelucchi, P. O'Brien, F. H. Peters, F. Gunning, and B. Corbett, "40 Gb/s WDM Transmission over 1.15-km HC-PBGF Using an InP-Based Mach-Zehnder Modulator at 2 μm," *Journal of Lightwave Technology*, vol. 34, pp. 1706–1711, 4 2016.

[16] B. Jalali and S. Fathpour, "Silicon Photonics," *Journal of Lightwave Technology*, vol. 24, no. 12, pp. 4600–4615, 2006.

[17] R. Soref, "The Past, Present, and Future of Silicon Photonics," *IEEE Journal of Selected Topics in Quantum Electronics*, vol. 12, no. 6, pp. 1678–1687, 2006.

[18] R. Baets, A. Z. Subramanian, S. Clemmen, B. Kuyken, P. Bienstman, N. Le Thomas, G. Roelkens, D. Van Thourhout, P. Helin, and S. Severi, "Silicon photonics: Silicon nitride versus silicon-on-insulator," in *Optical Fiber Communications Conference and Exhibition*, pp. 1–2, 2016.

[19] B. Jalali, S. Yegnanarayanan, T. Yoon, T. Yoshimoto, I. Rendina, and F. Coppinger, "Advances in silicon-on-insulator optoelectronics," *IEEE Journal of Selected Topics in Quantum Electronics*, vol. 4, no. 6, pp. 938–947, 1998.

[20] M. Borghi, C. Castellan, S. Signorini, A. Trenti, and L. Pavesi, "Nonlinear silicon photonics," *Journal of Optics*, vol. 19, 2017.

[21] R. A. Soref, "Silicon-based optoelectronics," *Proceedings of the IEEE*, vol. 81, no. 12, pp. 1687–1706, 1993.

[22] J. Leuthold, C. Koos, and W. Freude, "Nonlinear silicon photonics," 2010.

[23] A. D. Bristow, N. Rotenberg, and H. M. Van Driel, "Two-photon absorption and Kerr coefficients of silicon for 850-2200 nm," *Applied Physics Letters*, 2007.

[24] R. T. H. Collis, "Lidar," *Applied Optics*, vol. 9, pp. 1782–1788, 1970.

[25] R. T. Menzies and R. M. Hardesty, " Coherent Doppler lidar for measurements of wind fieldspp," *Proceedings of the IEEE*, vol. 77, no. 3, pp. 449–462, 1989.

[26] M. L. Chanin, A. Garnier, A. Hauchecorne, and J. Porteneuve, "A Doppler lidar for measuring winds in the middle atmosphere," *Geophysical Research Letters*, vol. 16, no. 11, pp. 1273–1276, 1989.

[27] C. J. Grund, R. M. Banta, J. L. George, J. N. Howell, M. J. Post, R. A. Richter, and A. M. Weickmann, "High-Resolution Doppler Lidar for Boundary Layer and Cloud Research," *Journal of Atmospheric and Oceanic Technology*, vol. 18, no. 3, pp. 376–393, 2001.

[28] A. Belmonte and B. J. Rye, "Heterodyne lidar returns in the turbulent atmosphere: performance evaluation of simulated systems," *Applied Optics*, vol. 39, pp. 2401–2411, 2000.

[29] A. Ghosh, A. S. Roy, S. D. Chowdhury, R. Sen, and A. Pal, "All-fiber tunable ring laser source near 2 μm designed for CO2 sensing," *Sensors and Actuators, B: Chemical*, vol. 235, pp. 547–553, 2016.

[30] J. A. Nwaboh, O. Werhahn, P. Ortwein, D. Schiel, and V. Ebert, "Laser-spectrometric gas analysis: CO2-TDLAS at 2μm," *Measurement Science and Technology*, vol. 24, no. 1, 2013.

[31] J. Huber, C. Weber, A. Eberhardt, and J. Wöllenstein, "Photoacoustic CO2-Sensor for Automotive Applications," *Procedia Engineering*, vol. 168, pp. 3–6, 2016.

[32] J. J. West, A. M. Fiore, L. W. Horowitz, and D. L. Mauzerall, "Global health benefits of mitigating ozone pollution with methane emission controls," *Proceedings of the National Academy of Sciences*, vol. 103, no. 11, pp. 3988–3993, 2006.

[33] A. M. Fiore, D. J. Jacob, B. D. Field, D. G. Streets, S. D. Fernandes, and C. Jang, "Linking ozone pollution and climate change: The case for controlling methane," *Geophysical Research Letters*, vol. 29, no. 19, p. 1919, 2002.

[34] K. Owen and A. Farooq, "A calibration-free ammonia breath sensor using a quantum cascade laser with WMS 2f/1f," *Applied Physics B: Lasers and Optics*, vol. 116, no. 2, pp. 371–383, 2014.

[35] C. Wang and P. Sahay, "Breath analysis using laser spectroscopic techniques: Breath biomarkers, spectral fingerprints, and detection limits," *Sensors*, vol. 9, pp. 8230–8262, 10 2009.

[36] S. Bevc, E. Mohorko, M. Kolar, P. Brglez, A. Holobar, D. Kniepeiss, M. Podbregar, N. Piko, N. Hojs, M. Knehtl, R. Ekart, and R. Hojs, "Measurement of breath ammonia for detection of patients with chronic kidney disease," *Clinical Nephrology*, vol. 88, pp. S14–S17, 2017.

[37] H. Li, A. Farooq, J. Jeffries, and R. K. Hanson, "Near-infrared diode laser absorption sensor for rapid measurements of temperature and water vapor in a shock tube," *Applied Physics B*, vol. 89, pp. 407–416, 2007.

[38] X. Zhou, X. Liu, J. B. Jeffries, and R. K. Hanson, "Development of a sensor for temperature and water concentration in combustion gases using a single tunable diode laser," *Measurement Science and Technology*, vol. 14, p. 1459, 2003.

[39] Walsh. J. T., T. J. Flotte, R. R. Anderson, and T. F. Deutsch, "Pulsed CO2 laser tissue ablation: Effect of tissue type and pulse duration on thermal damage," *Lasers in Surgery and Medicine*, vol. 8, pp. 108–118, 1988.

[40] T. Fortier and E. Baumann, "20 years of developments in optical frequency comb technology and applications," *Communications Physics*, vol. 2, 12 2019.

[41] R. Phelan, D. Byrne, J. O'carroll, M. Gleeson, M. Nawrocka, R. Lennox, K. Carney, C. Herbert, J. Somers, and B. Kelly, "Mid-Infrared InP-Based Discrete Mode Laser Diodes," in *Optical Fiber Applications* (G. Huerta-Cuellar and R. Imani, eds.), IntechOpen, 2019.

[42] P. M. Anandarajah, R. Maher, Y. Q. Xu, S. Latkowski, J. O'Carroll, S. G. Murdoch, R. Phelan, J. O'Gorman, and L. P. Barry, "Generation of coherent multicarrier signals by gain switching of discrete mode lasers," *IEEE Photonics Journal*, vol. 3, no. 1, pp. 112–122, 2011.

[43] I. Coddington, N. Newbury, and W. Swann, "Dual-comb spectroscopy," *Optica*, vol. 3, p. 414, 4 2016.

[44] E. Schrodinger, "An undulatory theory of the mechanics of atoms and molecules," *Physical Review*, vol. 28, no. 6, pp. 1049–1070, 1926.

[45] F. Schwabl, *Advanced Quantum Mechanics*. Springer, 4th ed., 2008.

[46] D. Kleppner, "Inhibited Spontaneous Emission," *Physical Review Letters*, vol. 47, no. 4, 1981.

[47] A. Einstein, "The Quantum Theory of Radiation," *Physikalische Zeitschrift*, vol. 18, p. 121, 1917.

[48] R. G. Gould, "The LASER, Light Amplification by Stimulated Emission of Radiation," in *The Ann Arbor Conference on Optical Pumping*, (the University of Michigan), 6 1959.

[49] L. F. Johnson, "Optical Maser Characteristics of Rare-Earth Ions in Crystals," *Journal of Applied Physics*, vol. 34, pp. 897–909, 1963.

[50] E. F. Schubert, *Light-Emitting Diodes*. Cambridge University Press, 2nd ed., 2006.

[51] C. P. Kuo, S. K. Vong, R. M. Cohen, and G. B. Stringfellow, "Effect of mismatch strain on band gap in III-V semiconductors," *Journal of Applied Physics*, vol. 57, pp. 5428–5432, 1985.

[52] P. M. J. Marée, J. C. Barbour, J. F. van der Veen, Kavanagh. K. L., C. W. T. Bulle-Lieuwma, and M. P. A. Viegers, "Generation of misfit dislocations in semiconductors," *Journal of Applied Physics*, vol. 62, pp. 4413–4420, 1987.

[53] D. L. Dexter and F. Seitz, "Effects of Dislocations on Mobilities in Semiconductors," *American Physical Society*, vol. 86, p. 964, 1952.

[54] C. Caneau, A. Srivastava, A. Dentai, J. Zyskind, and M. Pollack, "Room-temperature GaInAsSb/AlGaAsSb DH injection lasers at 2.2 μm," *Electronics Letters*, vol. 21, pp. 815–817, 1985.

[55] N. Holonyak, R. Kolbas, R. Dupuis, and P. Dapkus, "Quantum-well heterostructure lasers," *IEEE Journal of Quantum Electronics*, vol. 16, no. 2, pp. 170–186, 1980.

[56] R. Phelan, M. Gleeson, D. Byrne, J. O'Carroll, M. Nawrocka, K. Carney, R. Lennox, L. Maigyte, P. Long, C. Herbert, J. Somers, and B. Kelly, "High power narrow linewidth discrete mode laser diode integrated with a curved semiconductor optical amplifier emitting at 2051 nm," *Applied Optics*, vol. 57, p. E1, 8 2018.

[57] R. Phelan, J. O'Carroll, D. Byrne, C. Herbert, J. Somers, and B. Kelly, "In 0.75Ga 0.25As/InP multiple quantum-well discrete-mode laser diode emitting at 2 μm," *IEEE Photonics Technology Letters*, vol. 24, no. 8, pp. 652–654, 2012.

[58] A. Parriaux, K. Hammani, and G. Millot, "Electro-optic frequency combs," *Advances in Optics and Photonics*, vol. 12, p. 223, 3 2020.

[59] H. R. Telle, G. Steinmeyer, A. E. Dunlop, J. Stenger, D. H. Sutter, and U. Keller, "Applied Physics B Lasers and Optics Carrier-envelope offset phase control: A novel concept for absolute optical frequency measurement and ultrashort pulse generation," *Appl. Phys. B*, vol. 69, pp. 327–332, 1999.

[60] J. Pfeifle, V. Brasch, M. Lauermann, Y. Yu, D. Wegner, T. Herr, K. Hartinger, P. Schindler, J. Li, D. Hillerkuss, R. Schmogrow, C. Weimann, R. Holzwarth, W. Freude, J. Leuthold, T. J. Kippenberg, and C. Koos, "Coherent terabit communications with microresonator Kerr frequency combs," *Nature Photonics*, vol. 8, no. 5, pp. 375–380, 2014.

[61] S. B. Papp, K. Beha, P. Del'Haye, F. Quinlan, H. Lee, K. J. Vahala, and S. A. Diddams, "Microresonator frequency comb optical clock," *Optica*, vol. 1, p. 10, 7 2014.

[62] J. Ye, H. Schnatz, and L. W. Hollberg, “Optical Frequency Combs: From Frequency Metrology to Optical Phase Control,” *IEEE Journal on Selected Topics in Quantum Electronics*, vol. 9, pp. 1041–1058, 7 2003.

[63] P. Trocha, M. Karpov, D. Ganin, M. H. P. Pfeiffer, A. Kordts, S. Wolf, J. Krockenberger, P. Marin-Palomo, C. Weimann, S. Randel, W. Freude, T. J. Kippenberg, and C. Koos, “Ultrafast optical ranging using microresonator soliton frequency combs,” *Science*, vol. 359, no. 6378, pp. 887–891, 2018.

[64] B. Jerez, P. Martín-Mateos, E. Prior, C. de Dios, and P. Acedo, “Dual optical frequency comb architecture with capabilities from visible to mid-infrared,” *Optics Express*, vol. 24, p. 14986, 6 2016.

[65] N. Picqué and T. W. Hänsch, “Frequency comb spectroscopy,” *Nature Photonics*, vol. 13, pp. 146–157, 3 2019.

[66] L. E. Hargrove, R. L. Fork, and M. A. Pollack, “Locking of hene laser modes induced by synchronous intracavity modulation,” *Applied Physics Letters*, vol. 5, no. 1, pp. 4–5, 1964.

[67] P. Del’Haye, A. Schliesser, O. Arcizet, T. Wilken, R. Holzwarth, and T. J. Kippenberg, “Optical frequency comb generation from a monolithic microresonator,” *Nature*, vol. 450, pp. 1214–1217, 12 2007.

[68] A. Gambetta, N. Coluccelli, M. Cassinerio, D. Gatti, P. Laporta, G. Galzerano, and M. Marangoni, “Milliwatt-level frequency combs in the 8-14 μm range via difference frequency generation from an Er:fiber oscillator A huge number of applications in medical diagnostics,” *Optics Letters*, vol. 38, pp. 1155–1157, 2013.

[69] A. Hugi, G. Villares, S. Blaser, H. C. Liu, and J. Faist, “Mid-infrared frequency comb based on a quantum cascade laser,” *Nature*, vol. 492, pp. 229–233, 12 2012.

[70] D. C. Hanna, R. M. Percival, R. G. Smart, and A. C. Tropper, “Efficient and tunable operation of a Tm-doped fibre laser,” *Optics Communications*, vol. 75, no. 3-4, pp. 283–286, 1990.

[71] C. Gaida, T. Heuermann, M. Gebhardt, E. Shestaev, T. P. Butler, D. Gerz, N. Lilienfein, P. Sulzer, M. Fischer, R. Holzwarth, A. Leitenstorfer, I. Pupeza, and J. Limpert, “High-power frequency comb at 2 μm

wavelength emitted by a Tm-doped fiber laser system," *Optics Letters*, vol. 43, p. 5178, 11 2018.

[72] F. Adler and S. A. Diddams, "High-power, hybrid Er:fiber/Tm:fiber frequency comb source in the 2 μm wavelength region," *Opt. Lett.*, vol. 37, pp. 1400–1402, 2012.

[73] C. Huang, C. Wang, W. Shang, N. Yang, Y. Tang, and J. Xu, "Developing high energy dissipative soliton fiber lasers at 2 micron," *Sci Rep*, vol. 13680, 2015.

[74] P. S. Dutta and H. L. Bhat, "The physics and technology of gallium antimonide: An emerging optoelectronic material," *Journal of Applied Physics*, vol. 81, pp. 5821–5870, 1997.

[75] H. K. Choi and S. J. Eglash, "Room-temperature CW operation at 2.2 μm of GaInAsSb/AlGaAsSb diode lasers grown by molecular beam epitaxy," *Applied Physics Letters*, vol. 59, pp. 1165–1166, 1991.

[76] L. A. Sterczewski, C. Frez, S. Forouhar, D. Burghoff, and M. Bagheri, "Frequency-modulated diode laser frequency combs at 2 μm wavelength," *APL Photonics*, vol. 5, p. 076111, 7 2020.

[77] D. Burghoff, "Unraveling the origin of frequency modulated combs using active cavity mean-field theory," *Optica*, vol. 7, pp. 1781–1787, 2020.

[78] K. Kashani-Shirazi, K. Vizbaras, A. Bachmann, S. Arafin, and M. Amann, "Low-Threshold Strained Quantum-Well GaSb-Based Lasers Emitting in the 2.5- to 2.7-μm Wavelength Range," *IEEE Photonics Technology Letters*, vol. 21, no. 16, pp. 1106–1108, 2009.

[79] L. Shterengas, G. Kipshidze, T. Hosoda, R. Liang, T. Feng, M. Wang, A. Stein, and B. Belenky, "Cascade Pumping of 1.9–3.3 μm Type-I Quantum Well GaSb-Based Diode Lasers," *IEEE Journal of Selected Topics in Quantum Electronics*, vol. 23, no. 6, pp. 1–8, 2017.

[80] P. T. Ho, L. A. Glasser, E. P. Ippen, and H. A. Haus, "Picosecond pulse generation with a cw GaAlAs laser diode," *Applied Physics Letters*, vol. 33, no. 3, pp. 241–242, 1978.

[81] K. Y. Lau, "Gain switching of semiconductor injection lasers," *Applied Physics Letters*, vol. 52, no. 4, pp. 257–259, 1988.

[82] P. Paulus, R. Langenhorst, and D. Jager, "Generation and Optimum Control of Picosecond Optical Pulses from Gain-Switched Semiconductor Lasers," *IEEE Journal of Quantum Electronics*, vol. 24, no. 8, pp. 1519 – 1523, 1988.

[83] J. Auyeung, "Picosecond optical pulse generation at gigahertz rates by direct modulation of a semiconductor laser," *Applied Physics Letters*, vol. 38, no. 5, pp. 308–310, 1981.

[84] W. Weng, A. Kaszubowska-Anandarajah, J. He, P. D. Lakshmijayasimha, E. Lucas, J. Liu, P. M. Anandarajah, and T. J. Kippenberg, "Gain-switched semiconductor laser driven soliton microcombs," *Nature Communications*, vol. 12, 12 2021.

[85] N. Jukam, S. S. Dhillon, D. Oustinov, J. Madeo, C. Manquest, S. Barbieri, C. Sirtori, S. P. Khanna, E. H. Linfield, A. G. Davies, and J. Tignon, "Terahertz amplifier based on gain switching in a quantum cascade laser," *Nature Photonics*, vol. 3, pp. 715–719, 12 2009.

[86] J. M. Huikari, E. A. Avrutin, B. S. Ryvkin, J. J. Nissinen, and J. T. Kostamovaara, "High-energy picosecond pulse generation by gain switching in asymmetric waveguide structure multiple quantum well lasers," *IEEE Journal of Selected Topics in Quantum Electronics*, vol. 21, pp. 189–194, 11 2015.

[87] A. Rosado, A. Pérez-Serrano, J. M. G. Tijero, A. Valle, L. Pesquera, and I. Esquivias, "Experimental study of optical frequency comb generation in gain-switched semiconductor lasers," *Optics and Laser Technology*, vol. 108, pp. 542–550, 2018.

[88] R. Zhou, S. Latkowski, J. O'Carroll, R. Phelan, L. P. Barry, and P. Anandarajah, "40nm wavelength tunable gain-switched optical comb source," *Optics Express*, vol. 19, pp. B415–B420, 2011.

[89] A. Rosado, A. Perez-Serrano, J. M. G. Tijero, A. V. Gutierrez, L. Pesquera, and I. Esquivias, "Numerical and Experimental Analysis of Optical Frequency Comb Generation in Gain-Switched Semiconductor Lasers," *IEEE Journal of Quantum Electronics*, vol. 55, 12 2019.

[90] P. M. Anandarajah, S. P. Ó Dúill, R. Zhou, and L. P. Barry, "Enhanced Optical Comb Generation by Gain-Switching a Single-Mode Semiconductor Laser Close to Its Relaxation Oscillation Frequency,"

IEEE Journal of Selected Topics in Quantum Electronics, vol. 21, pp. 592–600, 11 2015.

[91] I. Fatadin, D. Ives, and M. Wicks, "Numerical simulation of intensity and phase noise from extracted parameters for CW DFB lasers," *IEEE Journal of Quantum Electronics*, vol. 42, no. 9, pp. 934–941, 2006.

[92] N. Schunk and P. Petermann, "Noise analysis of injection-locked semiconductor injection lasers ," *IEEE Journal of Quantum Electronics*, vol. 22, no. 5, pp. 642–650, 1986.

[93] E. Kapon, *Semiconductor lasers. Volume 1, Fundamentals*. Academic Press, 1999.

[94] L. A. Coldren, S. W. Corzine, and M. L. Mashanovitch, *Diode Lasers and Photonic Integrated Circuits*. John Wiley & Sons, Inc., 2012.

[95] A. K. Dutta and G. P. Agrawal, *Semiconductor Lasers*. Springer US, 1993.

[96] M. Ahmed, M. Yamada, and M. Saito, "Numerical modeling of intensity and phase noise in semiconductor lasers," *IEEE Journal of Quantum Electronics*, vol. 37, no. 12, pp. 1600–1610, 2001.

[97] K. Itô, "Stochastic integral," in *Proceedings of the Imperial Academy*, pp. 519–524, 1944.

[98] G. Maruyama, "Continuous Markov processes and stochastic equations," *Rendiconti del Circolo Matematico di Palermo*, vol. 4, no. 1, pp. 48–90, 1955.

[99] A. Horchler, " SDETools (https://github.com/horchler/SDETools)," 2021.

[100] G. P. Agrawal, "Effect of gain nonlinearities on period doubling and chaos in directly modulated semiconductor lasers," *Appl. Phys. Lett.*, vol. 49, p. 1013, 1986.

[101] H. R. Carleton and W. T. Maloney, "A Balanced Optical Heterodyne Detector," *Applied Optics*, vol. 7, pp. 1241–1243, 1968.

[102] E. Russell, N. Kavanagh, K. Shortiss, and F. Garcia Gunning, "Development of thulium-doped fibre amplifiers for the 2μm waveband," in *Proceedings of SPIE - The International Society for Optical Engineering*, vol. 10683, 2016.

[103] M. Jinno, "Correlated and Uncorrelated Timing Jitter in Gain-Switched Laser Diodes," *IEEE Photonics Technology Letters*, vol. 5, no. 10, pp. 1140–1143, 1993.

[104] U. L. Rohde, A. K. Poddar, and A. M. Apte, "Getting its measure," *IEEE Microwave Magazine*, vol. 14, no. 6, pp. 73–86, 2013.

[105] J. A. R. Griffith and G. Duxbury, "Laser Heterodyne Spectroscopy," *Philosophical Transactions of the Royal Society of London. Series A, Mathematical and Physical Sciences*, vol. 307, no. 1500, pp. 563–571, 1982.

[106] M. Bennett, M. F. Schatz, H. Rockwood, and K. Wiesenfeld, "Huygens's clocks," *Proceedings: Mathematical, Physical and Engineering Sciences*, vol. 458, no. 2019, pp. 563–579, 2002.

[107] J. H. Vincent, "On some Experiments in which Two Neighbouring maintained Oscillatory Circuits affect a Resonating Circuit," *Proceedings of the Physical Society of London*, vol. 32, pp. 84–91, 12 1919.

[108] H. L. Stover and W. H. Steier, "Locking of laser oscillators by light injection," *Applied Physics Letters*, vol. 8, no. 4, pp. 91–93, 1966.

[109] R. Zhou, P. M. Anandarajah, M. D. G. Pascual, J. O'Carroll, R. Phelan, B. Kelly, and L. P. Barry, "Monolithically Integrated 2-Section Lasers for Injection Locked Gain Switched Comb Generation," in *Optical Fiber Communication Conference*, p. Th3A.3, Optical Society of America, 2014.

[110] S. P. O. Duill, P. M. Anandarajah, R. Zhou, and L. P. Barry, "Numerical investigation into the injectionlocking phenomena of gain switched lasers for optical frequency comb generation," *Appl. Phys. Lett*, vol. 106, p. 211105, 2019.

[111] N. Kavanagh, D. Goulding, and F. C. Garcia Gunning, " Stable injection locking with slotted Fabry–Perot lasers at 2 μ m ," *Journal of Physics: Photonics*, vol. 1, p. 015005, 12 2018.

[112] C. N. Banwell, *Fundamentals of molecular spectroscopy*. New York: McGraw-Hill, 1972.

[113] D. Papousek and M. Aliev, "Molecular vibrational-rotational spectra," *Netherlands: Elsevier Scientific*, 1982.

[114] U. Platt and J. Stutz, *Differential Optical Absorption Spectroscopy*. Berlin, Heidelberg: Springer, 2008.

[115] S. Diddams, L. Hollberg, and V. Mbele, “Molecular fingerprinting with the resolved modes of a femtosecond laser frequency comb,” *Nature*, vol. 445, pp. 630–630, 2007.

[116] M. Lackner, “TUNABLE DIODE LASER ABSORPTION SPECTROSCOPY (TDLAS) IN THE PROCESS INDUSTRIES – A REVIEW,” *Reviews in Chemical Engineering*, 2007.

[117] L. Dong, F. K. Tittel, C. Li, N. P. Sanchez, H. Wu, C. Zheng, Y. Yu, A. Sampaolo, and R. J. Griffin, “Compact TDLAS based optical sensor for ppb-level ethane detection by use of a 3.34 μm room-temperature CW interband cascade laser,” *Optics Express*, vol. 24, pp. A528–A535, 2016.

[118] G. Gao, T. Zhang, G. Zhang, X. Lui, and T. Cai, “Simultaneous and interference-free measurements of temperature and C2H4 concentration using a single tunable diode laser at 1.62 μm ,” *Optics Express*, vol. 27, no. 13, pp. 17887 –17904, 2019.

[119] P. R. Griffiths and J. A. de Haseth, *Fourier Transform Infrared Spectrometry, Second Edition*. John Wiley & Sons, Inc, 2006.

[120] R. Mukhopadhyay, “Portable FTIR spectrometers get moving,” *ACS Publications*, 2004.

[121] J. Mandon, G. Guelachvili, and N. Picqué, “Fourier transform spectroscopy with a laser frequency comb,” *Nature Photonics*, vol. 3, pp. 99–102, 2009.

[122] F. Keilmann, C. Gohle, and R. Holzwarth, “Time-domain mid-infrared frequency-comb spectrometer,” *Optics Letters*, vol. 29, pp. 1542–1544, 2004.

[123] I. Coddington, W. C. Swann, and R. N. Newbury, “Coherent dual-comb spectroscopy at high signal-to-noise ratio,” *Physical Review A*, vol. 82, no. 4, 2010.

[124] T. Ideguchi, A. Poisson, and G. Guelachvili, “Adaptive real-time dual-comb spectroscopy,” *Nature communications*, vol. 5, p. 3375, 2014.

[125] Z. Chen, M. Yan, T. Hänsch, and P. Nathalie, "A phase-stable dual-comb interferometer," *Nature Communications*, vol. 9, p. 3035, 2018.

[126] C. Quevedo-Galán, V. Durán, A. Rosado, A. Pérez-Serrano, J. M. G. Tijero, and I. Esquivias, "Gain-switched semiconductor lasers with pulsed excitation and optical injection for dual-comb spectroscopy," *Optics Express*, vol. 28, p. 33307, 10 2020.

[127] B. Jerez, P. Martín-Mateos, E. Prior, C. de Dios, and A. Acedo, "Gain-switching injection-locked dual optical frequency combs: characterization and optimization," *Opt. Lett.*, vol. 41, pp. 4293–4296, 2016.

[128] E. P. Martin, S. Chandran, A. Rosado, E. P. Soderholm, J. K. Alexander, F. H. Peters, A. A. Ruth, and P. M. Anandarajah, "Mutually Injection Locked Gain Switched Optical Frequency Combs for Dual Comb Spectroscopy of H 2 S," in *Conference on Lasers and Electro-Optics, OSA Technical Digest*, Optical Society of America, 2020.

[129] N. R. Newbury, I. Coddington, and W. Swann, "Sensitivity of coherent dual-comb spectroscopy," *Optics Express*, vol. 18, pp. 7929–7945, 2010.

[130] P. A. M. Dirac, "The Quantum Theory o f the Emission and Absorption of Radiation," *Proc. Roy. Soc.*, vol. A114, no. 767, pp. 243–265, 1927.

[131] D. W. Ball, "Field Guide to Spectroscopy," *SPIE Press*, 2006.

[132] B. R. O'Dwyer M.F., Kent J.E., "Gross Atomic Structure. In: Valency. Heidelberg Science Library," in *Gross Atomic Structure, In: Valency*, Heidelberg Science Library. Springer, 1978.

[133] R. Eisberg, *Quantum Physics of Atoms, Molecules, Solids, Nuclei and Particles*. New York: John Wiley & Sons Inc., 1974.

[134] E. W. Michelson, A. A. Morley, "On a method of making the wave-length of sodium light the actual practical standard of length," *American Journal of Science*, vol. 34, no. 427, 1887.

[135] G. K. Woodgate, *Elementary Atomic Structure*. Oxford University Press, 1999.

[136] P. Zeeman, "The Effect of Magnetisation on the Nature of Light Emitted by a Substance," *Nature*, vol. 55, no. 347, 1897.

[137] J. Stark, "Observation of the Separation of Spectral Lines by an Electric Field," *Nature*, vol. 92, no. 401, 1913.

[138] H. V. McIntosh, "Symmetry and Degeneracy," in *Group Theory and its Applications*, pp. 75–144, Academic Press, 1971.

[139] H. Steinkemper, S. Fischer, M. Hermle, and J. C. Goldschmidt, "Stark level analysis of the spectral line shape of electronic transitions in rare earth ions embedded in host crystals," *New Journal of Physics*, vol. 15, 5 2013.

[140] Burshtein Zeev, " Radiative, nonradiative, and mixed-decay transitions of rare-earth ions in dielectric media ," *Optical Engineering*, vol. 49, no. 9, 2010.

[141] R. J. Mears et al., "Low-noise erbium-doped fibre amplifier operating at 1.54μm," *Electronics Letters*, vol. 23, no. 19, pp. 1026–1028, 1987.

[142] M. J. F. Digonnet, ed., *Rare Earth Doped Fiber Lasers and Amplifiers*. New York: CRC Press, 2nd ed., 2001.

[143] J. H. Van Vleck, "Theory of the Variations in Paramagnetic Anisotropy Among Different Salts of the Iron Group," *Physical Review, American Physical Society*, pp. 208–215, 1932.

[144] R. Paschotta, J. Nilsson, A. C. Tropper, and D. C. Hanna, "Ytterbium-doped fiber amplifiers," *IEEE Journal of Quantum Electronics*, vol. 33, no. 7, pp. 1049–1056, 1997.

[145] W. J. Miniscalco, "Erbium-doped glasses for fiber amplifiers at 1500 nm," *Journal of Lightwave Technology*, vol. 9, no. 2, pp. 234–250, 1991.

[146] C. B. Layne, W. H. Lowdermilk, and M. J. Weber, "Multiphonon relaxation of rare-earth ions in oxide glasses," *Physical Review B*, vol. 16, no. 10, 1997.

[147] A. de Pablos-Martín, A. Durán, and M. J. Pascual, "Nanocrystallisation in Oxyfluoride Systems: Mechanisms of Crystallisation and Photonic Properties," *International Materials Reviews*, vol. 57, no. 3, pp. 165–186, 2012.

[148] T. Komukai, T. Yamamoto, T. Sugawa, and Y. Miyajima, "Upconversion pumped thulium-doped fluoride fiber amplifier and laser operating at

1.47 μm," *IEEE Journal of Quantum Electronics*, vol. 31, no. 11, pp. 1880–1889, 1995.

[149] N. Bloembergen, S. Shapiro, P. S. Pershan, and J. O. Artman, "Cross-Relaxation in Spin Systems," *Physical Review*, vol. 144, no. 445, 1959.

[150] T. O. Sales, R. J. Amjad, C. Jacinto, and M. R. Dousti, "Concentration dependent luminescence and cross-relaxation energy transfers in Tb3+ doped fluoroborate glasses," *Journal of Luminescence*, vol. 205, pp. 282–286, 2019.

[151] S. D. Jackson, "Cross relaxation and energy transfer upconversion processes relevant to the functioning of 2 μm Tm3+-doped silica fibre lasers," *Optics Communications*, vol. 230, no. 1-3, pp. 197–203, 2004.

[152] R. Scheps, "Upconversion laser processes," *Progress in Quantum Electronics*, vol. 20, no. 4, pp. 271–358, 1996.

[153] L. F. Johnson and H. G. Guggenheim, "Infrared-Pumped Visible Laser," *Applied Physics Letters*, vol. 19, pp. 44–47, 1971.

[154] Y. Kawamura, J. Brooks, J. J. Brown, H. Sasabe, and C. Adachi, "Intermolecular Interaction and a Concentration-Quenching Mechanism of Phosphorescent Ir(III) Complexes in a Solid Film," *Physical Review Letters*, vol. 96, no. 1, p. 017404, 2006.

[155] Z. Li, A. M. Heidt, J. M. O. Daniel, Y. Jun, S. U. Alam, and D. J. Richardson, "Thulium-doped fiber amplifier for optical communications at 2 μm," *Opt. Express*, vol. 21, pp. 9297–9297, 2013.

[156] B. R. Judd, "Optical Absorption Intensities of Rare Earth Ions," *Physical Review*, vol. 127, no. 750, 1962.

[157] M. A. Saifi, "Optical Amplifiers," in *Encyclopedia of Materials: Science and Technology*, pp. 6416–6423, Elsevier, 2001.

[158] R. M. Sternheimer, "Shielding and Antishielding Effects for Various Ions and Atomic Systems," *Physical Review*, vol. 146, no. 140, pp. –, 1966.

[159] S. D. Agger and J. H. Povlsen, "Emission and absorption cross section of thulium doped silica fibers," *Opt. Express*, vol. 14, pp. 50–57, 2006.

[160] P. Peterka, I. Kasik, A. Dhar, B. Dussardier, and W. Blanc, “Theoretical modeling of fiber laser at 810 nm based on thulium-doped silica fibers with enhanced 3H4 level lifetime,” *Opt. Express*, vol. 19, pp. 2773–2781, 2011.

[161] D. Bayart, “Erbium-doped and Raman fiber amplifiers Amplificateurs à fibres dopée erbium et à effet Raman,” *Ann. Télécommun.*, vol. 58, pp. 1603–1639, 2003.

[162] H. A. Haus, “The noise figure of optical amplifiers,” *IEEE Photonics Technology Letters*, vol. 10, no. 11, pp. 1602–1604, 1998.

[163] A. A. M. Saleh, R. M. Jopson, J. Evankow, and J. Aspell, “Modeling of gain in erbium-doped fiber amplifiers,” *IEEE Photonics Technology Letters*, vol. 2, no. 10, pp. 714–717, 1990.

[164] B. Bernhardt, A. Ozawa, and P. e. a. Jacquet, “Cavity-enhanced dual-comb spectroscopy,” *Nature Photonics*, vol. 4, pp. 55–57, 2010.

[165] M. Thorpe and J. Ye, “Cavity-enhanced direct frequency comb spectroscopy,” *Applied Physics B*, vol. 91, pp. 397–414, 2008.

[166] D. S. Baer, J. B. Paul, M. Gupta, and A. O’Keefe, “Sensitive absorption measurements in the near-infrared region using off-axis integrated-cavity-output spectroscopy,” *Applied Physics B*, vol. 75, pp. 261–265, 2002.

[167] M. D. G. Pascual, V. Vujicic, J. Braddell, F. Smyth, P. Anandarajah, and L. Barry, “Photonic Integrated Gain Switched Optical Frequency Comb for Spectrally Efficient Optical Transmission Systems,” *IEEE Photonics Journal*, vol. 9, 6 2017.

[168] J. K. Alexander, L. Caro, M. Dernaika, S. P. Duggan, H. Yang, S. Chandran, E. P. Martin, A. A. Ruth, P. M. Anandarajah, and F. H. Peters, “Integrated dual optical frequency comb source,” *Optics Express*, pp. 16900–16906, 2020.

[169] N. Volet, A. Spott, E. J. Stanton, M. L. Davenport, L. Chang, J. D. Peters, T. C. Briles, I. Vurgaftman, J. R. Meyer, and J. E. Bowers, “Semiconductor optical amplifiers at 2.0-μm wavelength on silicon,” *Laser and Photonics Reviews*, vol. 11, 3 2017.

[170] N. Volet, A. Spott, E. J. Stanton, M. L. Davenport, J. Peters, J. Meyer, and J. E. Bowers, "Semiconductor optical amplifiers at 2.0-μm wavelength heterogeneously integrated on silicon," in *Conference on Lasers and Electro-Optics, OSA Technical Digest*, 2016.

[171] Z. Zhou, B. Yin, and J. Michel, "On-chip light sources for silicon photonics," *Light Science Applications*, 2015.

[172] Z. Yan, Y. Han, L. Lin, Y. Xue, C. Ma, W. Kit Ng, K. Sing Wong, and May Lau. K., "A monolithic InP/SOI platform for integrated photonics," *Light Science Applications*, vol. 10, no. 200, 2021.

[173] M. Smita, K. Williams, and J. van der Tol, "Past, present, and future of InP-based photonic integration," *APL Photonics*, vol. 4, 2019.

[174] V. Albino, U. Berardi, and R. M. Dangelico, "Smart Cities: Definitions, Dimensions, Performance, and Initiatives," *Journal of Urban Technology*, vol. 22, no. 1, pp. 3–21, 2015.

[175] T. Nam and T. A. Pardo, "Conceptualizing smart city with dimensions of technology, people, and institutions," in *Proceedings of the 12th Annual International Digital Government Research Conference: Digital Government Innovation in Challenging Times*, pp. 282–291, Association for Computing Machinery, 2011.

[176] A. Delmade, M. Krstić, C. Browning, J. Crnjanski, D. Gvozdić, and L. Barry, "Power efficient optical frequency comb generation using laser gain switching and dual-drive Mach-Zehnder modulator," *Optics Express*, vol. 27, p. 24135, 8 2019.

[177] X. Wang, W. Shen, W. Li, Y. Liu, Y. Yao, J. Du, Q. Song, and K. Xu, "High-speed silicon photonic Mach–Zehnder modulator at 2 μm," *Photonics Research*, vol. 9, p. 535, 4 2021.

[178] P. D. Lakshmijayasimha, A. Kaszubowska-Anandarajah, E. P. Martin, P. Landais, and P. M. Anandarajah, "Expansion and phase correlation of a wavelength tunable gain-switched optical frequency comb," *Optics Express*, vol. 27, pp. 16560–16570, 2019.

[179] T. J. Kippenberg, A. L. Gaeta, M. Lipson, and M. L. Gorodetsky, "Dissipative Kerr solitons in optical microresonators," 8 2018.

[180] P. Del'Haye, T. Herr, E. Gavartin, M. L. Gorodetsky, R. Holzwarth, and T. J. Kippenberg, "Octave spanning tunable frequency comb from a microresonator," *Physical Review Letters*, vol. 107, 8 2011.

[181] W. Weng, K. Kaszubowska-Anandarajah, J. Liu, P. M. Anandarajah, and T. J. Kippenberg, "Frequency division using a soliton-injected semiconductor gain-switched frequency comb," *Science Advances*, vol. 6, no. 39, 2020.